DISSERTATION

ON THE PARADOX OF CONVECTIVELY-COUPLED WAVES

Submitted by

Lyle Alistair Pakula

Department of Atmospheric Science

In partial fulfillment of the requirements

For the Degree of Doctor of Philosophy

Colorado State University

Fort Collins, Colorado

Summer 2006

COLORADO STATE UNIVERSITY

April 13, 2006

WE HEREBY RECOMMEND THAT THE DISSERTATION PREPARED UNDER OUR SUPERVISION BY LYLE ALISTAIR PAKULA ENTITLED ON THE PARADOX OF CONVECTIVELY COUPLED WAVES BE ACCEPTED AS FULFILLING IN PART REQUIREMENTS FOR THE DEGREE OF DOCTOR OF PHILOSOPHY.

Committee on Graduate Work

Richard H. Johnson

R. Johnson

J. Ramirez

Wayne Schubert

W. Schubert

Adviser, G. L. Stephens

Department Head, S. Rutledge

ABSTRACT OF DISSERTATION

ON THE PARADOX OF CONVECTIVELY-COUPLED WAVES

This thesis investigates the forced response of waves on a linearized, shallow water beta-plane in an attempt to develop some gross understanding of the properties of convectively coupled waves. Two concepts are central to this new theory: (i) a convectively coupled wave is a *forced* wave; (ii) a convectively coupled wave is a coupled feedback system, wherein the forcing and wave mutually reinforce one another. Furthermore, a convectively coupled wave exhibits phase-locked structures as it approaches steady state.

The basic theory of forced waves is explored and it is shown that such forced waves are governed by two equations, one for the amplitude and one for the frequency of the wave. The difference between the speed of the forcing and the theoretical speed of the wave, δc, is an essential parameter of these solutions. It is shown that many of the observed features of convectively-coupled waves, for example the energy spectra and apparent paradox of slow propagation, can be explained by consideration of the parameter δc.

Focus is then directed to the problem of the forced Kelvin wave, whose solutions show that a single wave produces two wave fronts that propagate at different phase speeds, one with a speed equal to the forced response and the other with a speed equal to the free response. Consideration of the feedback of the wave response to the forcing leads to the condition that $\delta c < 0$ is required to produce a positive feedback. Furthermore, using the derived definition of power and an alternate physical scaling argument leads to

the same optimal condition, $\delta c \propto -\sigma_x \varepsilon$, where σ_x is the x Gaussian scale of the forcing and ε is the dampening rate. This relationship serves as a predictive and diagnostic equation that correctly predicts the phase speed of convectively-coupled Kelvin waves and possibly the MJO as well adhering to the multi-scale view of these systems.

The theory introduced demonstrates that the structure of the forcing is central to its application. Furthermore, the large scale forcing represents the aggregate effect of many processes operating on smaller scales. The role of shallow cumulus clouds in this process is also explored and it is demonstrated that shallow convection is fundamental to moistening as well as the low-level static stability, both of which have a significant effect on convection and indirectly, the forcing of convectively coupled waves.

Lyle Alistair Pakula
Atmospheric Science Department
Colorado State University
Fort Collins, CO 80523
Summer 2006

Contents

List of Tables

List of Figures

Chapter 1

Introduction

The theory of equatorially trapped waves is frequently used as a basis for explaining many of the fundamental modes of variation of the large scale flows of the tropical atmosphere, including the Walker circulation (e.g. Gill 1980), the Madden Julian Oscillation (MJO Lau and Peng 1987, and others) and the El Nino-Southern Oscillation (ENSO Lau 1981). A key aspect of these phenomena is the way they apparently organize convection to such an extent that indices of deep convection, derived from observed Outgoing Longwave Radiation (OLR), are used to reveal the waves themselves (e.g. Lau and Peng 1987; Wheeler and Kiladis 1999). Because of the perceived importance of the interactions between the waves and convection, the observed wave-like phenomena in OLR are most often referred to as convectively coupled waves (e.g. Yang et al. 2003).

The theory of equatorial waves, most frequently developed for a linearized beta-plane (Matsuno 1966; Lindzen 1967), explains many of the salient wave-like structures observed in tropical circulations (e.g. Gill 1980; Silva Dias et al. 1983; Lau and Peng 1987; Wheeler et al. 2000; Yang et al. 2003; Biello and Majda 2005, and others). However, the interactions between the convection and the large-scale flow and the feedbacks defined by these interactions are not well understood and a paradox exists between the theory and observed structures as highlighted in time-longitude (Hovmoller) representations of OLR shown in Fig. 2.7a. The wave propagation speed implied by tracking areas of low OLR, and thus presumably deep convection, is significantly slower than that derived from linear wave theory that invokes expected vertical distributions of heating and related equivalent depths of the fluid. There are three prevailing ideas about the resolution of this paradox: (i) The interaction of convection with dynamics in some way modifies the background static stability or "equivalent depth" and thus the intrinsic phase speed (Gill 1982b; Emanuel et al. 1994; Neelin and Yu 1994, and others). (ii) The importance of different vertical wavelengths, and thus phase speeds, affect the propagation speeds of these systems (Lindzen 1973, 2003). (iii) That the inability to explain the propagation characteristics of the observed phenomena suggests that the system is not wave-like at all (Zhang 2005).

This investigation outlines a new dynamical theory to explain this paradox. Three concepts are important to the theory and its interpretation:

- a convectively coupled wave is a *forced* wave whereby the forcing is defined by convection. In forming the solution of the forced wave problem, the difference between the speed of the forcing and the theoretical speed of the wave, hereafter defined as δc, is an essential parameter of the particular solution. It is conjectured that the forcing and the wave propagate at different speeds and must do so to explain observed properties (i.e. $\delta c \neq 0$). This notion is at least supported in Fig. 2.7b taken from Wheeler et al. (2000). The figure is a time-longitude diagram of anomalies of OLR, sea-level pressure (SLP) and 1000 hPa (after Wheeler et al. 2000) of a composite convectively coupled Kelvin wave. As in Fig. 2.7a, the figures shows a convective envelope that propagates eastward at about 15 ms^{-1} whereas the SLP anomaly propagates eastward diverging away from the convective envelope at speeds more like that predicted by simple wave theory as indicated by the 44 ms^{-1} phase lines shown.

- a convectively coupled wave is a coupled feedback system, wherein the forcing and wave mutually reinforce one another. Although the theory explicitly investigates the problem of 'given a forcing, what then of the wave', the idea of feedback is a central concept of the theory introduced and in this context. It is suggested that reinforcing feedbacks only exist when the forcing propagates at speeds less than the wave itself (i.e. $\delta c < 0$). In this way we suggest that the apparent paradox is not a paradox at all but rather reflects the optimal configuration for self-sustaining convectively coupled waves.

- a convectively coupled wave exhibits features of phase-locking as it approaches steady state. We use the radio frequency engineering definition of phase locking which describes how one wave acquires another. It seems counter-intuitive that two waves propagating at different speeds can become phase-locked, where the forcing, considered as a wave, captures the wave response. The phase lock concept identifies a number of useful conditions about convectively coupled waves, such as the ratio of the forcing to wave amplitudes serving as a measure of the coupling and the tendency of phase-locking to filter out smaller scale structures.

Chapter 2 derives and analyzes the forced β-plane system, revealing that forced waves are governed by two equations; one relating to wave amplitude and the other to the phase speed. Furthermore, these equations are shown to relate to the energetics of the system such that the equation for wave amplitude is transformed into an equation for the time rate of change of energy (power) that describes the rate at which energy is drawn from the forcing and is thus termed the 'real' power of the forcing. The equation for phase is also converted to an equation of power and is conjectured to describe the rate at which energy is propagated away from the forcing region. The power quantity so derived is thus referred to as the 'radiant' power of the forcing.

These results are expanded upon in the context of the forced Kelvin wave in chapter 3. We present the solution of a Kelvin wave forced by a Gaussian forcing and choose this example, not only because of its observed importance to the large-scale flow patterns of the tropics, but also because its solution can be expressed analytically. Assuming that the condition for positive reinforcement of the forcing by the wave occurs in regions of large-scale (low level) convergence, then we show how the solutions reveal that a convectively-coupled Kelvin wave only positively feedbacks to the forcing, thus reinforcing the coupled system, when $\delta c < 0$. That is the forcing must propagate slower than the wave itself if the forcing that drives the wave is to be sustained by that wave.

Chapter 3 highlights the importance of the transient response for the Gaussian forced, undamped Kelvin wave and shows that comparison of the apparent β-plane frequencies with the physical space is ambiguous while also illustrating basic concepts introduced in chapter 2. We explore the feedbacks between the wave and the forcing in identifying the solutions that are most likely those that produce the observed Kelvin wave feature of the real atmosphere by consideration of the Gaussian forced, damped Kelvin wave. We then provide physical arguments for estimating characteristic values of δc for the convectively coupled Kelvin wave based on heuristic considerations involving both Bjerknes (1938) 'uniform' adjustment condition and Mapes (1993) stratiform mode lifting mechanism. These concepts lead to a linear scaling of δc as a function of forcing size and damping. These physical arguments are connected back to the definitions of real and radiant power where it is conjectured that the optimal configuration of convectively coupled waves is one in which energy is radiated away from the forcing at the same rate at which it is created by the forcing. This then permits the calculation of the optimal propagation speed for all wave types on the β-plane and it is shown that for the forced Kelvin wave, this concept leads to the same scaling relationship between δc as a function of forcing size and damping as deduced from the more physical arguments. We then show how this simple relationship appears to predict the correct phase speed of convectively-coupled Kelvin waves and, possibly, the MJO.

The investigation in chapters 2 and 3 highlight the importance of the physical structure of the forcing, both in space and time. While the large scale structure of the forcing can be deduced from observation (Yanai et al. 1973; Houze 1989; Johnson et al. 1999, and many others), it is becoming increasingly clear that the large-scale is representative of many cooperative processes operating on a variety of spatial and time scales that act to establish preferential forcing scales of the real atmosphere (for example Nakazawa 1988; Stephens et al. 2004a; Biello and Majda 2005; Zhang 2005). According to the optimal relationship derived in chapter 3, the propagation speeds of convectively coupled systems should be continuous based on a continues distribution of forcing sizes. While this is somewhat observed (Masunaga et al. 2006), spectral analysis of OLR reveals distinct spectral peaks in k (Wheeler and Kiladis 1999), which are analogous to peaks in forcing size. Thus, the observed propagation speeds of convectively-coupled systems are not continuous but discrete and the physical processes that control the propagation of the forcing are not understood.

Chapter 4 begins an investigation into what factors may contribute to the selective scale of the space-time structure of the forcing and, in particular, the role of shallow cumulus clouds on the tropical atmosphere. The importance of cumulus clouds has previously been highlighted (Yanai et al. 1973; Betts 1973; Johnson et al. 1999; Inness et al. 2001, and others) as one of the many mechanisms that influence the organization of convection and thus the forcing of convectively coupled waves. In this investigation a radiative convective equilibrium (RCE) cloud resolving model (CRM) is used to investigate elementary aspects the large-scale organization of convection with relation to the hydrologic cycle. It is found that cumulus clouds create a 'moist dome' feedback system that strongly influences deep convection and the resulting large-scale forcing fields. It is found that shallow clouds are integral in increasing moisture while decreasing low-level lapse rates, both of which produce a favorable environment for deep convection. This feedback, as shown, is sensitive to radiation and sea surface temperature and has significant implications for many tropical phenomena, including forced, convectively-coupled waves.

Chapter 5 summarizes the research described in this thesis and hints at future applications of the theory described. The main new findings are:

- Forced waves on the β-plane are governed by two equations, one for amplitude and the other for frequency (phase speed).
- These two equations relate to the 'real' and 'radiant' power of the forcing, the former indicating the work done on the atmosphere and the later the location of this work.
- The difference in phase speed of the forcing to that of the wave, denoted as δc is an essential parameter of the forced response problem.
- Consideration of a convectively-coupled wave as a forced wave response and that the forcing and response mutually feedback on each other in a positive fashion, explains several key observations in the atmosphere:
  - A direct comparison between observed energy spectra of meteorologic variables and that of the β-plane is ambiguous but with this in mind, the energy spectra can be explained
  - The observations of domain spectral energy and observations of convectively coupled waves with coherent structures outside the forcing region implies that $\delta c \neq 0$
  - Upon steady state, convectively coupled waves phase-lock and the necessary condition for this demonstrates the scale of the coherent response and the likelihood of convective-coupling
  - A positive feedback between the forcing and wave can only exist for $\delta c < 0$
  - Thus, the apparent paradox that the forcing travels slower than that theoretically implied is not a paradox at all but rather the optimal state.

- A forced wave response from a *propagating* forcing has a radius of influence defined by $R_{ix} \propto \delta c/\epsilon$ which reduces the expected form for a stationary forcing ($\delta c \rightarrow c$).

- For a forced Kelvin wave, the optimal propagation speed is given by two methods, both of which define $\delta c \propto -\sigma_x \epsilon$. This correctly predicts the observed convectively coupled Kelvin propagation speed as well as, possibly, the MJO. As a diagnostic equation, it predicts the correct damping rate in accordance with previous research. Furthermore, it adheres to the multi-scale view of convectively-coupled systems.

- Shallow cumulus clouds provide a feedback system that promotes deep convection by (i) moistening the environment, and (ii) reducing the low-level static stability as the clouds deepen.

- This feedback system, termed a 'moist dome' is sensitive to radiations interaction with water vapor and, thus, sea surface temperature.

Chapter 2

The Forced β-plane Equations and General Solutions

Sections 1 to 5 in this chapter derive the linearized shallow water β-plane equations from the compressible Navier Stokes equation on a rotating plane. We perform this to emphasize the approximations, and thus limits, of the shallow water β-plane equations since these will form the basis for most of this research. The shallow water β-plane equations are then solved for the conditions of a constant, propagating forcing with a linear Rayleigh Friction and Newtonian Cooling term, this leading to a governing spectral equation.

Section 6 performs a complex analysis on this spectral governing equations, separating it into two governing equations for wave amplitude and frequency (phase speed) and explores the physical significance of these two equations. Section 7 investigates the general wave behavior under a steadily propagating forcing, illuminating the importance of the phase speed difference δc and demonstrating that the wave response for a Gaussian thermal forcing remarkably resembles the structures of Fig 2.7b. Section 8 discusses the characteristics of the forced solutions in terms of phase locking and stability analogies drawn from radio frequency engineering and the work of Viterbi (1966). Section 9 provides a summary of the chapter and its key conclusions.

The theory begins with the compressible Navier-Stokes equations on a rotating plane:

$$\frac{D\mathbf{u}}{Dt} = -\frac{1}{\rho}\nabla p - \Omega \times \mathbf{u} - \mathbf{g} + \mathbf{F} \tag{2.1a}$$

$$\frac{D\rho}{Dt} + \rho\nabla \cdot \mathbf{u} = 0 \tag{2.1b}$$

$$C_p\frac{DT}{Dt} - \frac{1}{\rho}\frac{Dp}{Dt} = Q \tag{2.1c}$$

$$p = \rho RT \tag{2.1d}$$

Where

$$\frac{D}{Dt} = \frac{\partial}{\partial t} + u\frac{\partial}{\partial x} + v\frac{\partial}{\partial y} + w\frac{\partial}{\partial z}$$

$\mathbf{u}$ - three-component velocity vector : (u, v, w)

ρ - Density

p - pressure

T - Temperature

$\mathbf{F}$ - three-component momentum source and sinks vector : (F_u, F_v, F_w)

Q - Diabatic heat source and sinks

Ω - Earth rotation vector

$\mathbf{g}$ - Gravitational vector, with the earth's centrifugal force included

R - Dry air gas constant

C_p - specific heat of dry air at constant pressure

2.1. Quasi-Static Approximation and log-p Coordinates

The vertical component of the momentum equation (2.1a) is

$$\frac{Dw}{Dt} = -\frac{1}{\rho}\frac{\partial p}{\partial z} - g + F_z$$

and assuming a reference background state, such that $p(x, y, z, t) = p_s(z) + p'(x, y, z, t)$ and $\rho(x, y, z, t) = \rho_s(z) + \rho'(x, y, z, t)$, and further assuming this background state to be in hydrostatic balance $\left(\frac{\partial}{\partial z}p_s = -\rho_s g\right)$, then:

$$\rho_s\left(1 + \frac{\rho'}{\rho_s}\right)\frac{Dw}{Dt} \approx \rho_s\frac{Dw}{Dt} = -\frac{\partial p'}{\partial z} - \rho' g + \rho F_z \qquad \text{if } \rho' << \rho_s$$

The quasi-static approximation attempts to simplify the vertical momentum equation by use of scaling arguments. Since F_z is unknown at this time and could have any magnitude, this term must be set to zero. Hence, unresolved sources of vertical momentum can not be included in this model. A scale analysis performed on the horizontal momentum equation for typical atmospheric motions allows an estimate of the perturbation vertical pressure gradient (not shown). Under all conditions, the vertical acceleration term is negligible, such that;

$$\frac{\partial p}{\partial z} = -\rho g \qquad \text{if} \qquad \frac{\text{Depth}}{\text{Width}} << 1$$

the atmosphere remains in hydrostatic balance if the flow is dominated by horizontal motions (quasi two-dimensional). The quasi-static approximation does permit vertical motion, which can be diagnosed using the mass continuity equation, however, variations in the vertical pressure gradient will only be reflected by changes in ρ', that is buoyancy (temperature) rather than vertical acceleration.Thus, the quasi-static approximation has excluded non-hydrostatic flows from the model and any coupling with vertical momentum producing parameterizations.

In later sections, the solutions for the system will be separated by their horizontal and vertical structures. The separation is made easier by a change of vertical coordinate, from physical height to 'log p' coordinates, that is where $z = \ln(p_0/p)$. Appendix A outlines this procedure and we find the 'log p' system, with the f-plane approximation (not shown), to be:

$$\frac{Du}{Dt} = -\frac{\partial \phi}{\partial x} + fv + F_u \tag{2.2a}$$

$$\frac{Dv}{Dt} = -\frac{\partial \phi}{\partial y} - fu + F_v \tag{2.2b}$$

$$\frac{\partial \phi}{\partial z} = RT \tag{2.2c}$$

$$\frac{\partial u}{\partial x} + \frac{\partial v}{\partial y} + \frac{\partial w}{\partial z} - w = 0 \tag{2.2d}$$

$$\frac{DT}{Dt} + \kappa T w = \frac{Q}{C_p} \tag{2.2e}$$

$$p = \rho R T \tag{2.2f}$$

Where

$$\frac{D}{Dt} = \frac{\partial}{\partial t} + u\frac{\partial}{\partial x} + v\frac{\partial}{\partial y} + w\frac{\partial}{\partial z}$$

$$\phi = gz \qquad \kappa = \frac{R}{C_p}$$

where $f = 2\Omega \sin(\theta)$ and θ is the lattitude of the f-plane. Note that w is redefined as the vertical log pressure velocity and derivatives on z surfaces are now implied to be on $\ln(p_0/p)$ surfaces.

2.2. β-plane Approximation

The β-plane approximation attempts to represent the non-linear variation of the Coriolis parameter in the meridional direction by a linear function. A Taylor expansion of f

yields:

$$
\begin{aligned}
f(y_0 + y) &= f(y_o) + y\left(\frac{\partial f}{\partial y}\right)_{y=y_0} + \text{Higher Order Terms} \\
&\approx f(y_o) + y\beta
\end{aligned}
$$

Where higher order terms have been ignored and $\beta = \left(\frac{\partial f}{\partial y}\right)_{y=y_0}$ is the 'beta' term. Recalling that $f = 2\Omega\sin(\theta)$ and using the arc length formula $dy = ad\theta$;

$$
\beta = \left(\frac{\partial f}{\partial y}\right)_{y=y_0} = \left(\frac{\partial[2\Omega\sin(\theta)]}{a\partial\theta}\right)_{\theta=\theta_0} = \frac{2\Omega}{a}\cos(\theta_0)
$$

For the case of the β-plane situated on the equator ($\theta_0 = 0$), $f = 2\Omega y/a$. Note that as the actual Coriolis parameter must lie in the domain $[0, 2\Omega]$, the β-plane approximation is un-physical for $y > a$ and probably quantitatively incorrect for all y. That said, the β-plane approximation has been shown to be qualitatively accurate for the types of problems considered in this thesis and certainly suitable for such applications.

2.3. Linearization

The dependant variables for the quasi-static β-plane can be expressed as

$$
\begin{aligned}
u(x,y,z,t) &= \bar{u} + u'(x,y,z,t) \\
v(x,y,z,t) &= \bar{v} + v'(x,y,z,t) \\
w(x,y,z,t) &= \bar{w} + w'(x,y,z,t) \\
\phi(x,y,z,t) &= \bar{\phi}(z) + \phi'(x,y,z,t) \\
T(x,y,z,t) &= \bar{T}(z) + T'(x,y,z,t),
\end{aligned}
$$

where the mean states for ϕ and T are assumed to be a function of z. Setting the basic state to be at rest ($\bar{u} = \bar{v} = \bar{w} = 0$) and be in hydrostatic balance, as required by the quasi-static approximation, $\left(\frac{\partial \bar{\phi}}{\partial z} = R\bar{T}\right)$, (2.2) becomes;

$$\frac{\partial u'}{\partial t} + \frac{\partial \phi'}{\partial x} - \beta y v' = F_u - \left[u'\frac{\partial u'}{\partial x} + v'\frac{\partial u'}{\partial y} + w'\frac{\partial u'}{\partial z}\right] = F_u \tag{2.3a}$$

$$\frac{\partial v'}{\partial t} + \frac{\partial \phi'}{\partial y} + \beta y u' = F_v - \left[u'\frac{\partial v'}{\partial x} + v'\frac{\partial v'}{\partial y} + w'\frac{\partial v'}{\partial z}\right] = F_v \tag{2.3b}$$

$$\frac{\partial \phi'}{\partial z} = RT' \tag{2.3c}$$

$$\frac{\partial u'}{\partial x} + \frac{\partial v'}{\partial y} + \frac{\partial w'}{\partial z} - w' = 0 \tag{2.3d}$$

$$\frac{\partial T'}{\partial t} + w'\left(\frac{\partial \bar{T}}{\partial z} + \kappa \bar{T}\right) = \frac{Q}{C_p} - \left[u'\frac{\partial T'}{\partial x} + v'\frac{\partial T'}{\partial y} + w'\frac{\partial T'}{\partial z} + \kappa T' w'\right] = \frac{Q}{C_p} \tag{2.3e}$$

Noting that F_u, F_v and Q are redefined potentially containing the non-linear terms that would otherwise be set to zero by the 'negligible product of perturbations' approximation. From here on, primes are dropped and implied. In general, for the linearized system, one assumes that the sum of non-linear terms in square brackets is negligibly small compared to any of the individual terms on the left hand side. Thus, eddy fluxes are assumed negligible but all solutions should be checked for possible locations where this is assumption is broken.

The thermodynamic equation (2.3e) can be simplified by the introduction of a mean state static stability, defined as $\Gamma(z) = \frac{\partial \bar{T}}{\partial z} + \kappa \bar{T}(z)$. As this appears coupled to the vertical velocity, the first term represents the temperature change due to advection and the second term the temperature change associated with dry-adiabatic motions. As the mean state is in hydrostatic balance, it must also be unconditionally stable for dry convection, that is $\Gamma(z)$ must be positive.

2.4. Separation of Vertical and Horizontal Structure

Fortuitously, the β-plane system defined thus far is separable and allows the structure of the solution to be considered by two independent differential equations. We begin by collapsing the vertical differentials in (2.3c, d and e) into a single equation. Noting that $\frac{\partial w}{\partial z} - w = e^z \frac{\partial (e^{-z} w)}{\partial z}$, the continuity equation (2.3d) can be written as:

$$\frac{\partial u}{\partial x} + \frac{\partial v}{\partial y} + e^z \frac{\partial (e^{-z} w)}{\partial z} = 0, \tag{2.4}$$

and taking the time derivative of the hydrostatic equation (2.3c) and substituting in for $\frac{\partial T}{\partial t}$ in the thermodynamic equation (2.3e), we find:

$$\frac{\partial}{\partial z}\frac{\partial \phi}{\partial t} + R\Gamma w = \kappa Q \quad \text{where} \quad \kappa = R/C_p \tag{2.5}$$

It will be advantageous to redefine the thermal forcing as;

$$\frac{\partial}{\partial z}\frac{\partial \tilde{\phi}}{\partial t} = \kappa Q \tag{2.6}$$

where $\tilde{\phi}$ is the forced change in geopotential that would arise if the thermal heating were constrained to only alter the thickness of the layer and not drive any vertical motions (i.e. $w = 0$ in 2.5). Hence, (2.5) can be written as:

$$\frac{\partial}{\partial t}\frac{\partial (\phi - \tilde{\phi})}{\partial z} + R\Gamma w = 0 \tag{2.7}$$

Eliminating w by taking the $e^z \frac{\partial}{\partial z}\frac{e^{-z}}{R\Gamma}$ of (2.5) and substituting in (2.4), (2.3c, d and e) are reduced to a single equation:

$$\frac{\partial}{\partial t}\mathcal{L}_z[\phi - \tilde{\phi}] - \left(\frac{\partial u}{\partial x} + \frac{\partial v}{\partial y}\right) = 0 \tag{2.8}$$

where

$$\mathcal{L}_z[\ \ ] = e^z \frac{\partial}{\partial z} \frac{e^{-z}}{R\Gamma} \frac{\partial}{\partial z}[\ \ ]$$

is an operator only in z. The complete linearized system is thus:

$$\frac{\partial u}{\partial t} + \frac{\partial \phi}{\partial x} - \beta y v = F_u \quad (2.9a)$$

$$\frac{\partial v}{\partial t} + \frac{\partial \phi}{\partial y} + \beta y u = F_v \quad (2.9b)$$

$$\frac{\partial}{\partial t}\mathcal{L}_z[\phi - \tilde{\phi}] - \left(\frac{\partial u}{\partial x} + \frac{\partial v}{\partial y}\right) = 0 \quad (2.9c)$$

$$\frac{\partial}{\partial z}\frac{\partial \tilde{\phi}}{\partial t} = \kappa Q$$

noting w and T can be diagnosed from the original set of equations. It is self evident that (2.9c) is separable in the vertical and horizontal and since (2.9a and b) have no vertical derivatives, the system is linked through this equation. We may formally show this by assuming that $\phi(x, y, z, t) = \Psi(z)\Phi(x, y, t)$, with similar expressions for u, v, F_u, F_v and $\tilde{\phi}$. The forcing terms may contain dependencies on vertical derivatives but we propose that the forcing could be projected onto these vertical structure functions, such as that done by use of normal mode analysis (e.g. Fulton and Schubert 1985). The benefit of this derivation is that no assumption on the boundary conditions or horizontal structure is made (in contrast to the wavelike assumption in Lindzen 1967), enabling a general discussion of the solution. Substituting these into (2.9c), noting that (2.9a and b) are trivial and omitted:

$$\mathcal{L}_z[\Psi(z)]\frac{\partial}{\partial t}[\Phi(x, y, t) - \tilde{\Phi}(x, y, t)] - \Psi(z)\left(\frac{\partial U(x, y, t)}{\partial x} + \frac{\partial V(x, y, t)}{\partial y}\right) = 0 \quad (2.10)$$

which can be rearranged to:

$$\frac{\mathcal{L}_z[\Psi(z)]}{\Psi(z)} = \frac{\left(\frac{\partial U(x,y,t)}{\partial x} + \frac{\partial V(x,y,t)}{\partial y}\right)}{\frac{\partial}{\partial t}[\Phi(x,y,t) - \tilde{\Phi}(x,y,t)]} = \frac{-1}{c^2} \tag{2.11}$$

Two eigenvalue problems are defined for the vertical and horizontal structure with c^2 the eigenvalue of this separation, noting that we have chose that this must be negative for physical solutions, then:

$$\frac{\partial \Phi}{\partial t} + c^2 \left(\frac{\partial U}{\partial x} + \frac{\partial V}{\partial y}\right) = \frac{\partial \tilde{\Phi}}{\partial t} \tag{2.12a}$$

$$\mathcal{L}_z[\Psi] + \Psi/c^2 = 0 \tag{2.12b}$$

noting that the modified versions of (2.9a and b) would be required to solve (2.12a), which are now formally equivalent to the shallow water equations on a linearized β-plane . Section 2.5 is dedicated to the solution of this system and for the rest of this section, we investigate the properties of the vertical structure problem (2.12b). Setting Γ constant in (2.12b) greatly simplifies the problem to:

$$\frac{\partial^2 \Psi}{\partial z^2} - \frac{\partial \Psi}{\partial z} + \frac{R\Gamma}{c^2}\Psi = 0$$

which we note is an oscillator equation with a generating function. We can remove this generating term by use of a Euler transform through the assumption that $\Psi(z) = \Psi'(z)e^{z/2}$, then:

$$\frac{\partial^2 \Psi'}{\partial z^2} + \left(\frac{R\Gamma}{c^2} - \frac{1}{4}\right)\Psi' = 0 \tag{2.13}$$

which has the characteristic solution $\Psi(z) = (Ae^{imz} + Be^{-imz})e^{z/2}$ with $m = \pm\left(\frac{R\Gamma}{c^2} - \frac{1}{4}\right)^{\frac{1}{2}}$. If c^2 is large enough, evanescent solutions pertain while wave solutions pertain otherwise. In either the wave or evanescent contexts, m is related to the vertical depth of the vertical structure function, Ψ. If $R\Gamma/c^2 >> 1/4$, which for a typical atmosphere

($\Gamma \sim 17$ K) implies $c << 138$ m/s then

$$c \sim \sqrt{R\Gamma}/m \sim 50/j \text{ m/s}$$

where j is the vertical mode of the wavelike (baroclinic) solution. Note that j is continuous in this discussion but is discrete under the 'rigid upper-lid' boundary condition (Fulton and Schubert 1985). Thus, the first baroclinic mode has a horizontal propagation speed of ~ 50 m/s. Only one mode has a phase speed $c > 138$ m/s, the external mode or Lamb wave, and under either a rigid lid or radiation upper boundary condition, this solution is evanescent (trapped) as $c \sim 300$ m/s (DeMaria 1985; Wu et al. 2000b).

It has been shown by Fulton and Schubert (1985), and follows from the separable property of the system, that the forcing can be considered a projection onto a set of vertical basis functions and then the resultant solution will be governed by the consideration of the vertical and horizontal structure separately. In section 2.5, the forced horizontal solution is shown to be wavelike with time structure $e^{\pm i\omega t}$, where ω is an apparent frequency. Hence, if the vertical solution is wavelike, it will propagate with vertical phase speed $c_v = \omega/m$ but if it is evanescent, it is vertically trapped. Since both m and ω can be of either sign, this defines that energy may propagate in four directions, that is 'radially' away in the vertical plane. As the horizontal solutions govern ω, we can consider this a parameter defined by $\omega = c_p k$, where c_p is the horizontal phase speed and k is the horizontal wave number. Thus, $c_v = c_p k/m$, implying that for a given vertical structure of forcing (i.e. constant m), horizontally larger disturbances (small k) will propagate slower in the vertical. Furthermore, faster intrinsic modes (i.e. Kelvin versus Rossby modes) will propagate faster in the vertical but that under forced conditions, phase-locking can occur that implies the vertical propagation will be reduced. As will be shown, the concept of phase-locking introduced later implies that waves propagate at the speed of their forcing so that the apparent vertical propagation speed will be set by the speed of the forcing under phase-locked conditions. Note that this is just an apparent advection of vertical propagating energy since in the refract frame of the forcing, the vertical propagation is always zero in phase-lock.

2.5. Solutions of the Divergent Barotropic Model

In Section 2.4 it was shown that the compressible β-plane can be separated into vertical and horizontal eigenproblems with a common eigenvalue c^2. The horizontal eigenproblem was shown to be equivalent to the divergent barotropic equations on a linearized β-plane , that is:

$$\frac{\partial u}{\partial t} + \frac{\partial \phi}{\partial x} - \beta y v = F_u - \epsilon u \tag{2.14a}$$

$$\frac{\partial v}{\partial t} + \frac{\partial \phi}{\partial y} + \beta y u = F_v - \epsilon v_m \tag{2.14b}$$

$$\frac{\partial \phi}{\partial t} + c^2 \left(\frac{\partial u}{\partial x} + \frac{\partial v}{\partial y} \right) = F_\phi - \epsilon \phi \tag{2.14c}$$

Where a constant Rayleigh friction / Newtonian cooling linear damping term (ϵ) has been added and the forcing terms are now defined as projections onto the vertical structure function of this mode:

$$F_u = F'_u \bullet \Psi(z)$$

$$F_v = F'_v \bullet \Psi(z)$$

$$F_\phi = \frac{\partial \tilde{\Phi}}{\partial t} = \left[\int \kappa Q dz \right] \bullet \Psi(z)$$

noting that F_ϕ represents the vertically integrated total mass sink/source projected onto this vertical solution. Rewriting this in matrix form;

$$\left(\frac{\partial}{\partial t} + \epsilon \right) \mathbf{W} + \mathbf{L}\mathbf{W} = \mathbf{F} \tag{2.15}$$

where $\mathbf{W} = \begin{pmatrix} u(x,y,t) \\ v(x,y,t) \\ \phi(x,y,t) \end{pmatrix}$, $\mathbf{F} = \begin{pmatrix} F_u(x,y,t) \\ F_v(x,y,t) \\ F_\phi(x,y,t) \end{pmatrix}$ and $\mathbf{L} = \begin{pmatrix} 0 & -\beta y & \frac{\partial}{\partial x} \\ \beta y & 0 & \frac{\partial}{\partial y} \\ c^2 \frac{\partial}{\partial x} & c^2 \frac{\partial}{\partial y} & 0 \end{pmatrix}$ and

restating the definition variables:

u	-	x velocity perturbation
v	-	y velocity perturbation
ϕ	-	geopotential height perturbation
$\beta = \dfrac{\partial f}{\partial y}$	-	Meridional gradient of coriolis parameter
ϵ	-	coefficient of damping
F_u, F_v, F_ϕ	-	Forcing terms of u, v and ϕ, possibly containing non-linear terms
$c^2 = gh$	-	Characteristic Phase Speed
g	-	gravitational constant
h	-	equivalent depth or scale height

An analogous system exists on the sphere through modification of the operator **L** except that such a system becomes prohibitively complex to solve analytically (Longuet-Higgins 1968). The equations represented by (2.15) are usually made non-dimensional but we refrain from doing so. These equations also differ from those of Matsuno (1966) through the presence of an unspecified general forcing by diabatic heating and momentum source terms as well as through the presence of a linear damping term. Unlike Matsuno (1966) and other studies, we refrain from assuming wavelike solutions in (x, t), effectively Fourier transforming (2.15) with respect to these two dimensions. Generality of the forcing is maintained by noting that at any given time, it too may be Fourier transformed in space but not in time and thus define for a general function the Fourier transform pair $f(x, y, t)$ and $\hat{f}(k, y, t)$ as:

$$\hat{f}(k, y, t) = \frac{1}{(2\pi)^{1/2}} \int_{-\infty}^{\infty} f(x, y, t) e^{-ikx} dx \qquad (2.16a)$$

$$f(x, y, t) = \frac{1}{(2\pi)^{1/2}} \int_{-\infty}^{\infty} \hat{f}(k, y, t) e^{ikx} dk \qquad (2.16b)$$

Note that on the infinite plane k is continuous, however, with periodic or closed boundary conditions k becomes a discrete quantity which we may express as $f_k(y, t)$. Keeping the notation for the continuous values of k and applying the Fourier transform to (2.15) produces:

$$\left(\frac{\partial}{\partial t}+\epsilon\right)\hat{\mathbf{W}}+\hat{\mathbf{L}}\hat{\mathbf{W}}=\hat{\mathbf{F}} \tag{2.17}$$

where $\hat{\mathbf{W}}=\begin{pmatrix}\hat{u}\\ \hat{v}\\ \hat{\phi}\end{pmatrix}$, $\hat{\mathbf{F}}=\begin{pmatrix}\hat{F}_u\\ \hat{F}_v\\ \hat{F}_\phi\end{pmatrix}$ and $\hat{\mathbf{L}}=\begin{pmatrix}0 & -\beta y & ik\\ \beta y & 0 & \dfrac{\partial}{\partial y}\\ ikc^2 & c^2\dfrac{\partial}{\partial y} & 0\end{pmatrix}$

2.5a. Homogenous Solution

Wu and Moore (2004) showed that there exists a complete set of solutions for the homogenous version of eqn (2.17) (i.e. for $\mathbf{F}=\epsilon=0$). Since the goal of this study is to find the particular solution for a given forcing and damping of the system, the known completeness of the homogenous solution defines that the particular solution will be an appropriate combination of homogenous solutions. Hence, we now discuss the homogenous solution, which is taken to be separable and oscillatory in time and of the form $\hat{u}(k,y,t)=U(k,y)e^{i\nu t}$ with similar expressions for $\hat{v}$ and $\hat{\phi}$, so that (2.17) becomes:

$$\hat{\mathbf{L}}\mathbf{K}=-i\nu\mathbf{K} \tag{2.18}$$

where $\mathbf{K}(k,y)=\begin{pmatrix}U(k,y)\\ V(k,y)\\ \Phi(k,y)\end{pmatrix}$ and is complex and ν is the eigenvalue. One might be tempted to write $\hat{\mathbf{W}}(k,y,t)=\mathbf{K}(k,y)e^{i\nu t}$ but we emphasize this is only true for $\mathbf{F}=0$ and $\epsilon=0$, that is the unforced and undamped solution. Using suitable row operations, one can show that:

$$U=\frac{-i}{\nu^2-c^2k^2}\left[\nu\beta yV+kc^2\frac{dV}{dy}\right] \tag{2.19}$$

$$\Phi=\frac{ic^2}{\nu^2-c^2k^2}\left[k\beta yV+\nu\frac{dV}{dy}\right] \tag{2.20}$$

and that (2.18) reduces to the following ordinary differential equation:

$$\frac{d^2V}{dy^2} + \left[\frac{\nu^2}{c^2} - k^2 + \beta\frac{k}{\nu} - \frac{\beta^2}{c^2}y^2\right]V = 0 \tag{2.21}$$

Which is formally equivalent to the classic harmonic oscillator equation except for the y^2 term, hence, this will yield oscillatory or evanescent solutions depending on the value of y, that is the meridional extent of the wave. Thus, equatorial waves are trapped between some latitude and that their meridional extent will be proportional to $\sqrt{c/\beta}$. We proceed to solve this equation recognizing it as Hermites' Differential equations (Appendix B) but we additional use a power series method (Appendix D) to illustrate that the Hermite polynomials that form the solution are composed of odd and even functions and that all basis functions must be considered when speaking of the true physical solution.

i. ***Hermite's Solution*** We now cast this equation into Hermites Differential equation (See Appendix B or Gradshteyn and Ryzhik 2000) by non-dimensionalizing the y variable using $y = \sqrt{c/\beta}\hat{y}$, where the 'hat' is not to be confused with that of the Fourier transform, then

$$\frac{d^2V}{d\hat{y}^2} + \left[\frac{\nu^2}{c\beta} - \frac{c}{\beta}k^2 + c\frac{k}{\nu} - \hat{y}^2\right]V = 0 \tag{2.22}$$

We now state the 'radiation' boundary condition on the problem by assuming that $V(k, \hat{y}) \to 0$ as $\hat{y} \to \infty$. The following substitution removes the $\hat{y}^2$ part from the second term and will also guarantee the boundary condition;

$$V(k, \hat{y}) = \hat{V}(k, \hat{y})e^{-\hat{y}^2/2} \tag{2.23}$$

then (2.22) becomes:

$$\frac{d^2\hat{V}}{d\hat{y}^2} - 2\hat{y}\frac{d\hat{V}}{d\hat{y}} + \left[\frac{\nu^2}{c\beta} - \frac{c}{\beta}k^2 + c\frac{k}{\nu} - 1\right]\hat{V} = 0 \tag{2.24}$$

Which is now formally equivalent to Hermites Differential Equation provided the cubic root equation for ν satisfies

$$\frac{\nu^2}{c\beta} - \frac{c}{\beta}k^2 + c\frac{k}{\nu} - 1 = 2n \tag{2.25}$$

where $n = 0, ..., \infty$ and $\check{V}(k,\hat{y}) = H_n(\hat{y})$ where H_n is the n'th Hermite polynomial. It is important to note that the Hermite polynomials are orthogonal with respect to the inner product $\int_{-\infty}^{\infty} H_{n'}(\hat{y})H_n(\hat{y})e^{-\hat{y}^2}d\hat{y}$ and that the eigenvalue depends on both the Hermite number (n) and cubic root (r) and thus we write the eigenvalue as $i\nu_{n,r}$. Note that this differential equation contains a generating term dependant on $\hat{y}$, indicating that this is actually a source term - the β affect. In this respect $\check{V} \to \infty$ as $\hat{y} \to \infty$ however, weighting this by $e^{-\hat{y}^2/2}$ guarantees that $V \to 0$ as $\hat{y} \to \infty$, easily verified by considering L'Hosptials rule and that the Hermite solution is polynomial while the weighting function is exponential and will, thus, always obtain.

The Kelvin Wave

An additional non trivial solution for (2.18) exists for $V(k,y) = 0$, in which case the system becomes;

$$\nu U + k\Phi = 0 \tag{2.26a}$$

$$\frac{\partial \Phi}{\partial y} + \beta y U = 0 \tag{2.26b}$$

$$\nu\Phi + kc^2 U = 0 \tag{2.26c}$$

Reducing (2.26) to two equations for Φ, it is easily verified that the dispersion relation is;

$$\nu = \pm ck$$

and that the general solution is;

$$\Phi(k,y) = e^{\pm\frac{1}{2}\frac{\beta}{c}y^2}$$

Only the negative exponent satisfies the radiation boundary condition on y thus, the positive solution must be discarded and the Kelvin wave has the form;

$$\begin{pmatrix} U(k,y) \\ V(k,y) \\ \Phi(k,y) \end{pmatrix} = \begin{pmatrix} c \\ 0 \\ c^2 \end{pmatrix} e^{-\frac{1}{2}\frac{\beta}{c}y^2} \tag{2.27}$$

and $\nu_{-1,2} = -ck$, where it has been indexed as $n = -1$, which is one of the roots for (2.25) with $n = -1$. Furthermore, the Kelvin wave is non-dispersive (i.e. Inertia Gravity wave like) and may only propagate east and we notionally index it as $r = 2$.

ii. Discussion of Eigenvalues The homogenous system (2.18) eigenvalues are given by ν, which from the solution to V are given by the cubic equation:

$$\frac{\nu_{n,r}^2}{c\beta} - \frac{c}{\beta}k^2 + c\frac{k}{\nu_{n,r}} = 2n+1 \quad (n = 0, 1, ..., \infty) \quad (r = 0, 1, 2) \tag{2.28}$$

Where $\nu_{n,r}$ specifies that for every eigenvalue n there are 3 roots ($r = 0, 1, 2$) which form three separate eigenvalues for the homogenous system. Since all other coefficients are parameters of the system, this forms a dispersion relation for the eigenfunctions. We now explore the behavior of these eigenvalues as a function of k, depicted non-dimensionally by setting $\nu_d = \nu_{nd}\sqrt{c\beta}$ and $k_d = k_{nd}\sqrt{c/\beta}$ in Fig. 2.1a for all k and Fig. 2.1b for $k \geq 0$ on a log-log scale and where subscripts n and nd refer to dimensional and non-dimensional, respectively.

The dispersion equation (D.1) can be simplified by considering its behavior at large

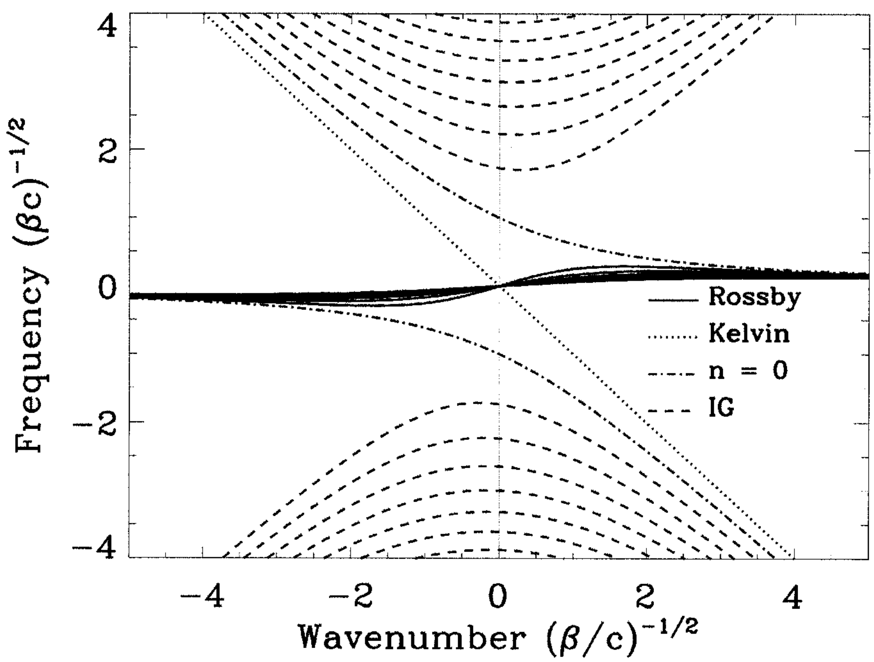

a)

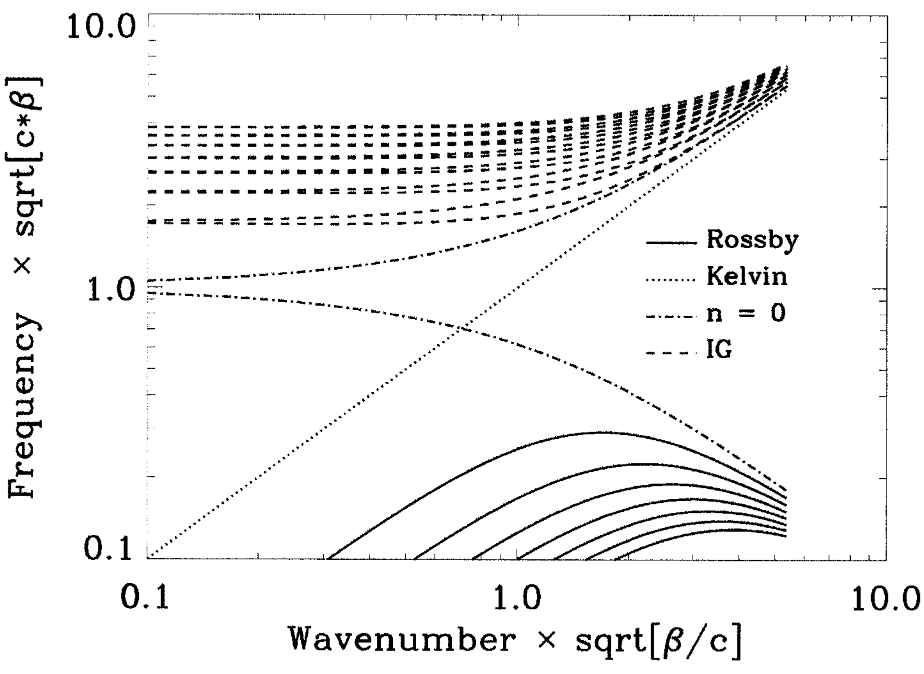

b)

Figure 2.1: Non-Dimensional dispersion diagrams for the shallow water β-plane system. (a) has linear scaling for $-\infty < k < \infty$ whilst (b) depicts the log-log scale of the absolute frequencies for $k > 0$ only.

k. The first term may be ignored provided that $\nu k^2/\beta << k$ and that $\nu < 1$, then

$$\nu_{n,0} = ck/(2n + 1 + \frac{c}{\beta}k^2)$$

If $\nu > 1$, then the first term must be included but the third term may be ignored, then:

$$\nu_{n,1} = +\sqrt{c^2k^2 + c\beta(2n+1)}$$
$$\nu_{n,2} = -\sqrt{c^2k^2 + c\beta(2n+1)}$$

In Fig. 2.1 these roots are spectrally separated. Considering the phase speed of these solutions, that is $c_p = \nu/k$, the '$r = 0$' root describes a wave whose phase speed is always less than the maximum (c) and always propagates west. The '$r = 1$' and '$r = 2$' roots frequency are symmetrical in k such that their phase speed changes direction with the change of sign of k but, importantly, are always faster than the maximum (c). The eigenfunctions, to be discussed, show that the slow moving wave is quasi-geostrophic and, as in Matsuno (1966), is referred to as a Rossby wave. The fast moving waves are referred to as Inertia-Gravity (IG) waves but since they have no directional sense when all k are considered, we refer to both roots as IG waves, in contradiction to typical nomenclature that only considers $k \geq 0$.

n=0 Modes

Special care is needed when $n = 0$, as the dispersion equation factors to;

$$(\nu_{0,r} - ck)\left(\frac{1}{c\beta}\nu_{0,r}^2 + \frac{1}{\beta}k\nu_{0,r} - 1\right) = 0$$

in which case;

$$\nu_{0,0} = ck$$
$$\nu_{0,1} = -\frac{c}{2}k + \frac{1}{2}\sqrt{c^2k^2 + 4c\beta}$$
$$\nu_{0,2} = -\frac{c}{2}k - \frac{1}{2}\sqrt{c^2k^2 + 4c\beta}$$

The '$r = 0$' root must be rejected as nonphysical because it corresponds to a zero in the denominator for the solution to $U(k, y)$ and $\Phi(k, y)$ (i.e. 2.19 and 2.20). Root '$r = 1$' and '$r = 2$' both exhibit phase speeds that are typical of Rossby and Inertia-Gravity waves, when considered for all k. Typical nomenclature for $k \geq 0$ identifies the first root as a mixed-Rossby gravity wave and the second as an eastward IG wave but we note the 2nd root also exhibits Rossby phase speeds for $k < 0$ and we refer to these solutions simply as the "$n = 0$" solutions.

Inertia-Gravity Waves

Fig 2.1 shows that IG waves are strongly dispersive, while in a non-rotating system they are non-dispersive (Gill 1982a). The group velocity ($\frac{\partial \nu}{\partial k}$) in Fig 2.1a shows that IG waves slow for larger k. Furthermore, there is an asymmetry towards slower westward waves versus eastward waves since both roots depict a turning point for the group velocity in westward propagating quadrants of the dispersion diagram, this depicted more clearly in the log-log plot (Fig 2.1b). Using the large k approximation, the group velocity is:

$$\frac{d\nu}{dk} = \frac{\pm c}{\left(1 + \frac{\beta}{ck^2}(2n+1)\right)^{1/2}}$$

Which only captures the symmetrical decrease in group velocity for $k \rightarrow 0$, noting that the reduction in phase speed for a given k increases as a function of β and n. The mechanism for wave propagation is the phase difference between the divergence and pressure fields. For larger waves (smaller k), these fields vary much more slowly in time and, by their increased scale, approach the Rossby radius of deformation, even near the equator. Thus, we conjecture that larger IG waves geostrophically adjust, reducing the isallobaric flow and hence divergence, decreasing the speed of the wave.

Consider the spectral momentum equations (2.3a and b) rearranged to identify the terms that balance the pressure gradient force;

$$ik\Phi = \beta y V - i\nu U \tag{2.29a}$$

$$\frac{\partial \Phi}{\partial y} = -\beta y U - i\nu V \tag{2.29b}$$

then we note that the beta (Coriolis) term does not depend on the size of the wave (k) or the frequency (ν) while the other term do in a way that for an increasing wave size ($k \rightarrow 0$), these terms become smaller implying an increasing importance of the beta term and thus the system tends towards geostrophy. Interestingly, as $k \rightarrow 0$, the U wind is driven purely by the beta term, implying an inertial oscillation. In this manner, if $\beta = 0$, that is some scale where rotation may be neglected, the dispersion equation reduces to that of the non-rotating, non-dispersive IG wave system. We note that the group velocity depends on n because this relates to the turning latitude of the wave and, for increasing n, implies increasing y and thus, f.

Geostrophy also implies the existence of Potential Vorticity (PV), symbolized as q, which can be shown for the spectral β-plane system discussed here to be:

$$q = \frac{-\beta V}{i\nu} \tag{2.30}$$

where

$$q = \frac{\partial V}{\partial x} - \frac{\partial U}{\partial y} - \beta y \Phi / c^2$$

such that the PV is proportional to the meridional flow advecting the planetary vorticity. Hence, a Kelvin wave possess no PV as $V = 0$, IG waves possess some PV as $V \neq 0$ and $\nu \neq 0$ and Rossby waves are strongly PV driven as $\nu \rightarrow 0$. From the previous discussion, for small IG waves ($k \rightarrow \infty$), $\nu \approx \pm ck$ such that (2.29a) implies that $\beta V \propto k^{-1}$. Thus, small IG waves carry little PV while large ones possess increasingly more PV, again implying a greater tendency for geostrophy. We conjecture that the asymmetry between east and westward IG waves is a result of large scale westward moving IG waves having more PV, with similar group velocity to Rossby waves and, thus, conjectured to be behaving as a Rossby wave. One may physically understand this by considering the divergence field for a monochromatic IG wave moving east and conversely, one moving west. Consider then how the PV anomalies induced by the meridional winds might cause a local rotation that feedbacks on the wave in a Rossby like fashion. In general, the PV anomalies act to damp the divergence field since they are associated with geostrophy but for the eastward IG wave, the PV anomalies moves out of phase with the westward Rossby propagation tendency, while the westward IG remains in phase and then amplifies the PV anomaly. Hence, the westward IG waves have more PV and propagate slower than their eastward counterpart at scales where geostrophy becomes important.

These concepts are best illustrated by visualization of the eigenfunctions as a function of k in Fig. 2.4 and Fig. 2.5. These figures illustrate the magnitude of the divergence and U and V wind vectors in the (k, y) plane. The scale of the contours and wind vectors varies from figure to figure. For example, note that the Kelvin wave contains no V wind component, indicating no PV. Rossby waves are dominated by V wind and have little divergence compared to the other waves. The IG waves also consist of large zonal wind and divergence fields for $|k| \rightarrow \infty$ but become more PV dominated as $k \rightarrow 0$. The '$n = 0$' waves exhibit both characteristics in a much stronger manner as expected by their typified mixed characteristics.

In summary, the naming conventions and permissible roots of the dispersion equation (D.1) are introduced here to be :

$$\text{for } n > 0 \qquad \frac{\nu_{n,r}^2}{c\beta} - \frac{c}{\beta}k^2 + c\frac{k}{\nu_{n,r}} = 2n+1 \qquad r = \begin{cases} 0 & \text{Rossby} \\ 1 & \text{inertia gravity} \\ 2 & \text{inertia gravity} \end{cases}$$

$$\text{for } n = 0 \qquad \nu_{0,r} = \begin{cases} -\frac{c}{2}k + \frac{1}{2}\sqrt{c^2k^2 + 4c\beta} & r = 1 \\ -\frac{c}{2}k - \frac{1}{2}\sqrt{c^2k^2 + 4c\beta} & r = 2 \end{cases} \qquad \text{“n = 0”}$$

$$\text{for } n = -1 \quad \nu_{-1,2} = -ck \qquad r = 2 \qquad \text{Kelvin}$$

iii. The Eigenfunctions From (2.23), the solution to V is used to solve for U and Φ in (2.19) and (2.20). As the solution to V is only known to an arbitrary constant, we thus define a constant that makes the substitution a little easier and yields natural units:

$$V(k,y) = i\beta^{-1}(\nu_{n,r}^2 - c^2k^2)H_n\left(\sqrt{\tfrac{\beta}{c}}y\right)e^{-\frac{1}{2}\frac{\beta}{c}y^2}$$

Substituting this into the definition of U and Φ;

$$U(k,y) = \sqrt{c/\beta}\left[\frac{1}{2}(\nu_{n,r} - ck)H_{n+1}\left(\sqrt{\tfrac{\beta}{c}}y\right) + n(\nu_{n,r} + ck)H_{n-1}\left(\sqrt{\tfrac{\beta}{c}}y\right)\right]e^{-\frac{1}{2}\frac{\beta}{c}y^2}$$

$$\Phi(k,y) = c\sqrt{c/\beta}\left[\frac{1}{2}(\nu_{n,r} - ck)H_{n+1}\left(\sqrt{\tfrac{\beta}{c}}y\right) - n(\nu_{n,r} + ck)H_{n-1}\left(\sqrt{\tfrac{\beta}{c}}y\right)\right]e^{-\frac{1}{2}\frac{\beta}{c}y^2}$$

Redefining $\mathbf{K}_{n,r}(k,y)$ as a three component, complex matrix depending on the indices n and r and incorporating the Kelvin Wave;

$$\mathbf{K}_{n,r}(k,y) = \begin{pmatrix} U(k,y) \\ V(k,y) \\ \Phi(k,y) \end{pmatrix} =$$

$$\begin{cases} \begin{pmatrix} \sqrt{c/\beta}\left[\frac{1}{2}(\nu_{n,r}-ck)H_{n+1}\left(\sqrt{\frac{\beta}{c}}y\right)+n(\nu_{n,r}+ck)H_{n-1}\left(\sqrt{\frac{\beta}{c}}y\right)\right] \\ i\beta^{-1}(\nu_{n,r}^2-c^2k^2)H_n\left(\sqrt{\frac{\beta}{c}}y\right) \\ c\sqrt{c/\beta}\left[\frac{1}{2}(\nu_{n,r}-ck)H_{n+1}\left(\sqrt{\frac{\beta}{c}}y\right)-n(\nu_{n,r}+ck)H_{n-1}\left(\sqrt{\frac{\beta}{c}}y\right)\right] \end{pmatrix} e^{-\frac{1}{2}\frac{\beta}{c}y^2} & n \geq 0 \\ \begin{pmatrix} c \\ 0 \\ c^2 \end{pmatrix} e^{-\frac{1}{2}\frac{\beta}{c}y^2} & n = -1 \end{cases}$$

which is the complete solution to (2.18) according to Wu and Moore (2004). Figures 2.2 and 2.3 present the magnitude of the eigenfunctions in the (k,y) plane noting that the contours are of geopotential and the scale of these contours and wind vectors differ from figure to figure.

2.5b. Particular Solution

Given the completeness of the homogenous solution as mentioned, the solution to (2.17) is an appropriate combination of the homogenous solutions, given by the eigenfunctions **K**. We now define a normal mode transform in the meridional direction using **K** as a set

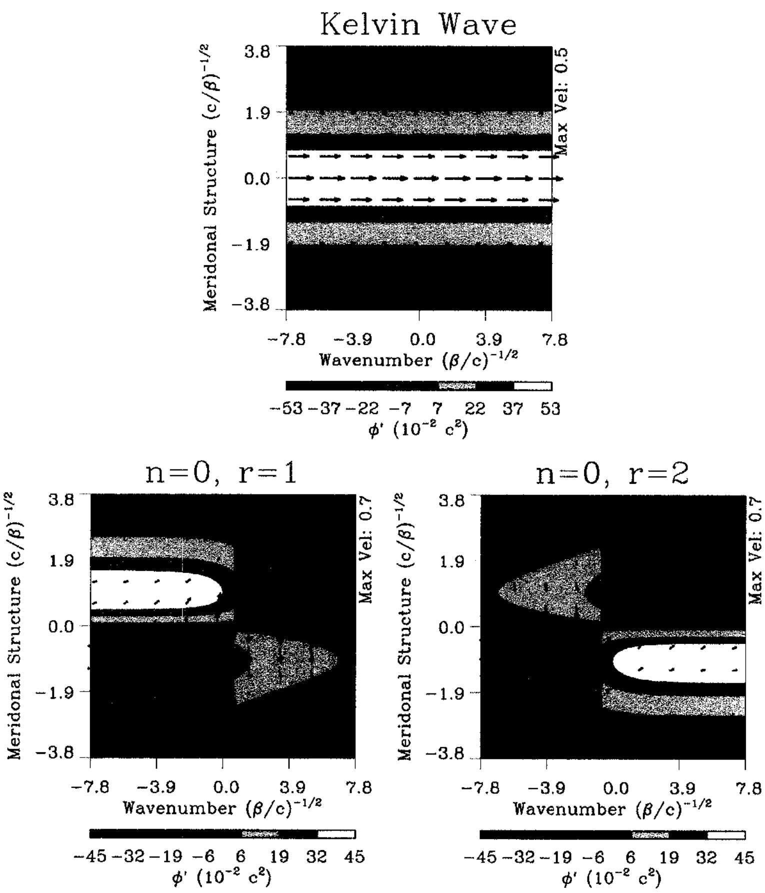

Figure 2.2: Partial visualization of **K** transformation kernel for $n = -1$ to $n = 0$. Note that all figures are non-dimensionalized and wind vectors are scaled for each figure independently.

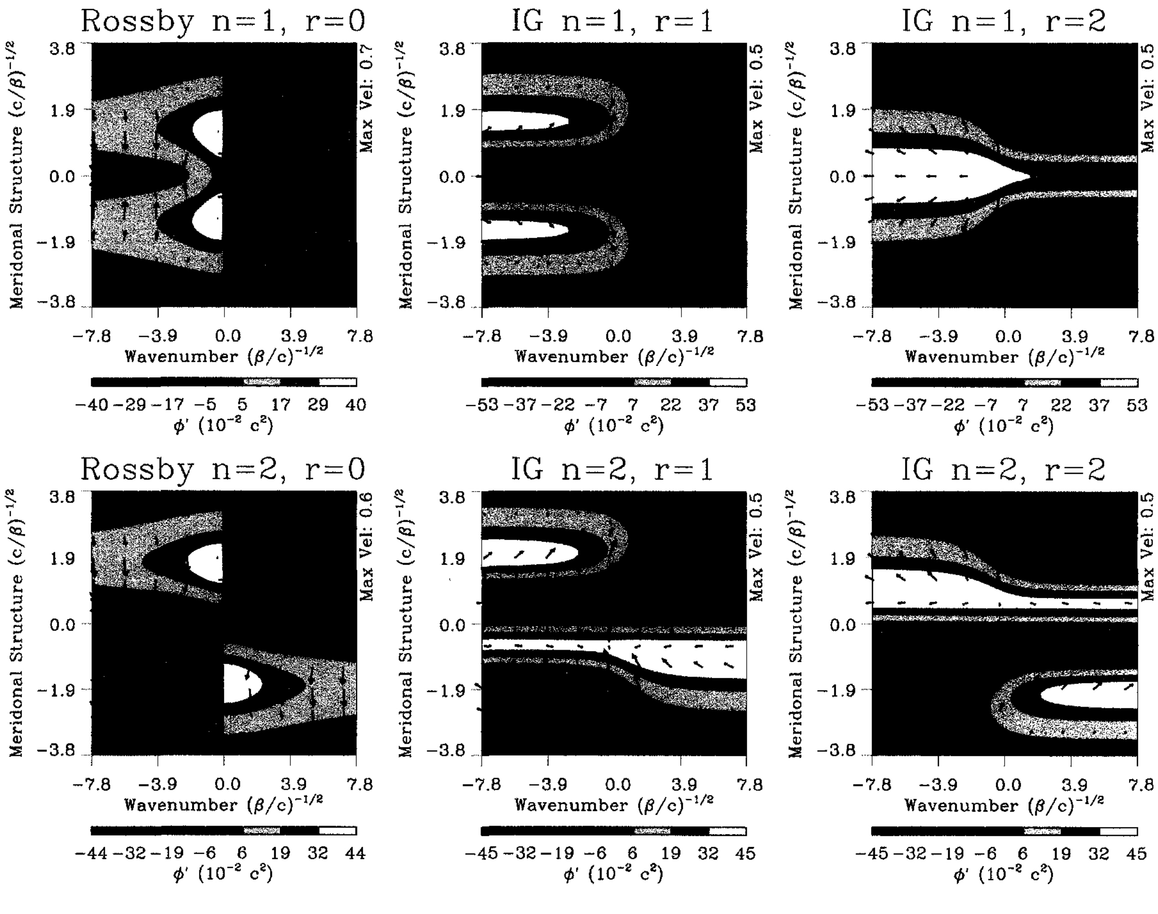

Figure 2.3: Partial visualization of **K** transformation kernel for $n = 1$ to $n = 2$. Note that all figures are non-dimensionalized and wind vectors are scaled for each figure independently.

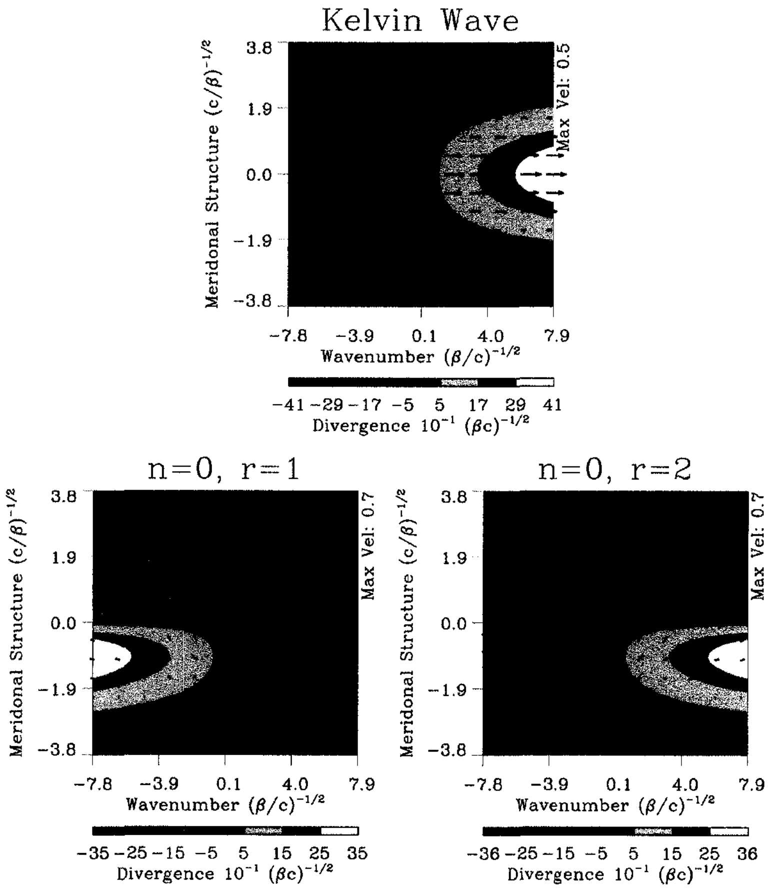

Figure 2.4: Partial visualization of the divergence of the**K** transformation kernel for $n = -1$ to $n = 0$. Note that all figures are non-dimensionalized and wind vectors are scaled for each figure independently.

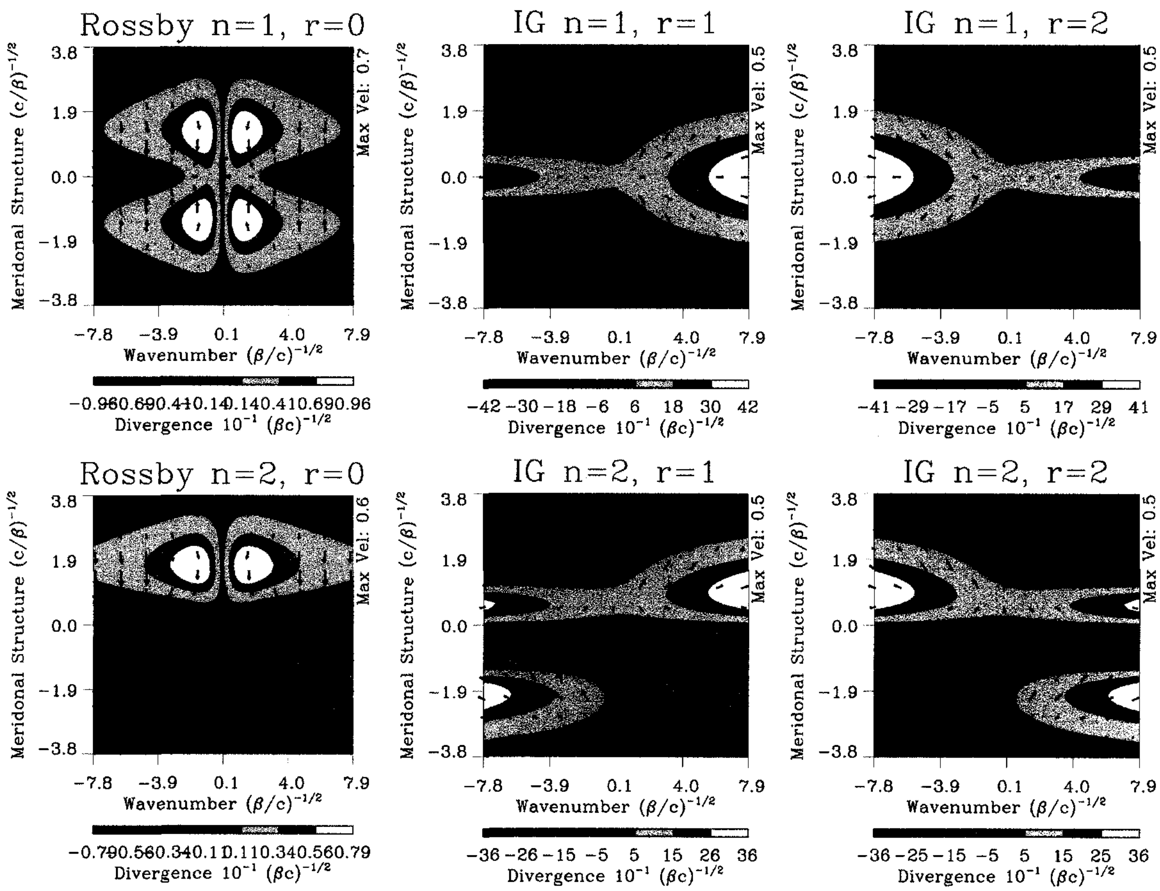

Figure 2.5: Partial visualization of the divergence of the **K** transformation kernel for $n = 1$ to $n = 2$. Note that all figures are non-dimensionalized but wind vectors are scaled for each figure independently.

of basis functions, noting that the transform must ensure orthonormality:

$$W_{n,r}(k,t) = \left(\hat{\mathbf{W}}(k,y,t), \mathbf{K}_{n,r}(k,y)\right) \tag{2.31a}$$

$$\hat{\mathbf{W}}(k,y,t) = \sum_{n,r} W_{n,r}(k,t)\mathbf{K}_{n,r}(k,y) \tag{2.31b}$$

where

$$(\mathbf{f}, \mathbf{g}) = c^{-2} \int_{-\infty}^{\infty} (f_1 g_1^* + f_2 g_2^* + \frac{1}{c^2} f_3 g_3^*) d\hat{y}$$

is the inner product of any two complex, three-component vectors and g^* denotes the complex conjugate. The definition of this inner product is motivated by the total energy of the system, (i.e. $\frac{\partial}{\partial t}(u^2 + v^2 + \phi^2/c^2)$ and the orthogonality of $\mathbf{K}$ with respect to this inner product such that our desired property is summarized as:

$$(\mathbf{K}_{n,r}(k,y), \mathbf{K}_{n',r'}(k,y)) = \begin{cases} 1 & (n,r) = (n',r') \\ 0 & (n,r) \neq (n',r') \end{cases} \tag{2.32}$$

To assure orthonormality, we take the inner product $(\mathbf{K}N, \mathbf{K}N)$, with N being a normalization constant and note that $\int_{-\infty}^{\infty} H_m(\hat{y}) H_n(\hat{y}) e^{-\hat{y}^2} d\hat{y} = \delta_{mn} 2^n n! \sqrt{\pi}$. We then find;

$$\frac{1}{N_{n,r}^2} = \begin{cases} 2^n n! \frac{\sqrt{\pi}}{c\beta} \left[(c\beta)^{-1} (\nu_{n,r}^2 - c^2 k^2)^2 + (n+1)(\nu_{n,r} - ck)^2 + n(\nu_{n,r} + ck)^2 \right] & n \geq 0 \\ 2\sqrt{\pi} & n = -1 \end{cases} \tag{2.33}$$

Taking the inner product of (2.18) with $\mathbf{K}_{n'r'}$, noting that $\hat{\mathbf{L}}$ is skew-Hermitian with respect to the inner-product, such that:

$$\left(\hat{\mathbf{L}} f, g\right) = -\left(f, \hat{\mathbf{L}} g\right)$$

and it follows;

$$\left(\hat{\mathbf{L}}\mathbf{K}_{n,r}, \mathbf{K}_{n'r'}\right) = \left(-i\nu_{n,r}\mathbf{K}_{n,r}, \mathbf{K}_{n'r'}\right)$$

$$\left(\mathbf{K}_{n,r}, \hat{\mathbf{L}}\mathbf{K}_{n'r'}\right) + i\nu_{n,r}\left(\mathbf{K}_{n,r}, \mathbf{K}_{n'r'}\right) = 0$$

$$\left(\mathbf{K}_{n,r}, -i\nu_{n',r'}\mathbf{K}_{n'r'}\right) + i\nu_{n,r}\left(\mathbf{K}_{n,r}, \mathbf{K}_{n'r'}\right) = 0$$

$$\left(\mathbf{K}_{n,r}, \mathbf{K}_{n'r'}\right)\left(\nu_{n,r} - \nu_{n',r'}\right) = 0$$

so that $\mathbf{K}$ is orthogonal so long as degeneracy does not occur in the eigenvalues. For the Rossby modes ($r = 0$), degeneracy does occur when $k = 0$ and we follow the procedure of Schubert and Masarik (2005) outlined in Appendix C to find the orthogonal eigenfunctions for this case.

Since the meridional normal mode transform (2.31) has been shown to be complete, orthogonal and orthonormal, it can be used to form the particular solution for the inhomogeneous system (2.17). Taking the meridional transform of (2.17):

$$\left(\frac{\partial\hat{\mathbf{W}}}{\partial t}, \mathbf{K}_{n,r}\right) + \left(\epsilon\hat{\mathbf{W}}, \mathbf{K}_{n,r}\right) + \left(\hat{\mathbf{L}}\hat{\mathbf{W}}, \mathbf{K}_{n,r}\right) = \left(\hat{\mathbf{F}}, \mathbf{K}_{n,r}\right),$$

which becomes

$$\left(\frac{\partial}{\partial t} + \epsilon\right) W_{n,r} + \left(\hat{\mathbf{L}}\hat{\mathbf{W}}, \mathbf{K}_{n,r}\right) = F_{n,r} \tag{2.34}$$

where $F_{n,r}(t) = \left(\hat{\mathbf{F}}(t), \mathbf{K}_{n,r}\right)$ is the forcing term at time t. Since $\hat{\mathbf{L}}$ is skew-Hermitian, $\left(\hat{\mathbf{L}}\hat{\mathbf{W}}, \mathbf{K}_{n,r}\right) = -\left(\hat{\mathbf{W}}, \hat{\mathbf{L}}\mathbf{K}_{n,r}\right) = -\left(\hat{\mathbf{W}}, -i\nu_{n,r}\mathbf{K}_{n,r}\right) = -i\nu_{n,r}W_{n,r}$ and (2.34) becomes:

$$\left(\frac{\partial}{\partial t} + \epsilon - i\nu_{n,r}\right) W_{n,r} = F_{n,r} \tag{2.35}$$

which is the governing spectral equation for the particular solution.

In the process of linearizing the system, the non-linear terms can be grouped into the forcing terms. If these are projected back onto the linear modes, the non-linear problem is not solved analytically. Rather, the non-linear forcing is projected onto the linear space but the true non-linear solution could only ever be calculated with the use of a fully non-linear model. The utility of incorporating the non-linear terms in the forcing might be to identify the scale that they operate on and, possibly, also capture some of their affects. One may not assume that all non-linear forcing produces a non-linear result, as is the basis of the model used by Biello and Majda (2005).

i. ***Computational Simplification*** We use a modified function following Schubert and Masarik (2006):

$$\mathcal{H}_n(\hat{y}) = H_n(\hat{y})e^{-\frac{1}{2}\hat{y}^2}(2^n n!)^{-\frac{1}{2}} \tag{2.36}$$

to simplify the computation of $\mathbf{K}$ and $N_{n,r}$. This allows us to take the original form of the Hermite recurrence relation (Appendix B) and, multiplying them by $e^{-\frac{1}{2}\hat{y}^2}(2^n n!)^{-\frac{1}{2}}$, form a modified recurrence relation:

$$\hat{y}\mathcal{H}_n(\hat{y}) = \left(\frac{n+1}{2}\right)^{\frac{1}{2}} \mathcal{H}_{n+1}(\hat{y}) + \left(\frac{n}{2}\right)^{\frac{1}{2}} \mathcal{H}_{n-1}(\hat{y}) \tag{2.37a}$$

$$\frac{\partial \mathcal{H}_n(\hat{y})}{\partial y} = -\left(\frac{n+1}{2}\right)^{\frac{1}{2}} \mathcal{H}_{n+1}(\hat{y}) + \left(\frac{n}{2}\right)^{\frac{1}{2}} \mathcal{H}_{n-1}(\hat{y}) \tag{2.37b}$$

The recurrence relation is initialized using the definition of the Hermite polynomials $H_0 = 1$ and $H_1 = 2\hat{y}$ in (2.36) to obtain $\mathcal{H}_0(\hat{y}) = e^{-\frac{1}{2}\hat{y}^2}$ and $\mathcal{H}_1(\hat{y}) = \sqrt{2}\,\hat{y}\,e^{-\frac{1}{2}\hat{y}^2}$. This modified recurrence relation offers a numerical advantage, avoiding calculation of the factorial values and large values associated with the Hermite polynomials. Figure (2.6) depicts the structure of $\mathcal{H}$ for the first (a) five functions while (b) and (c) depict the even and odd functions for the first 63 components. Note that for increasing n, the turning latitude increases for a given meridional wave structure.

The solution is now summarized as:

$$\mathbf{K}_{n,r}(k,\hat{y}) =$$
$$\begin{cases} \begin{pmatrix} (c/2\beta)^{\frac{1}{2}}\left[(n+1)^{\frac{1}{2}}(\nu_{n,r}-ck)\mathcal{H}_{n+1}(\hat{y})+n^{\frac{1}{2}}(\nu_{n,r}+ck)\mathcal{H}_{n-1}(\hat{y})\right] \\ i\beta^{-1}(\nu_{n,r}^2-c^2k^2)\mathcal{H}_n(\hat{y}) \\ c(c/2\beta)^{\frac{1}{2}}\left[(n+1)^{\frac{1}{2}}(\nu_{n,r}-ck)\mathcal{H}_{n+1}(\hat{y})-n^{\frac{1}{2}}(\nu_{n,r}+ck)\mathcal{H}_{n-1}(\hat{y})\right] \end{pmatrix} N_{n,r} & n \geq 0 \\ \begin{pmatrix} c \\ 0 \\ c^2 \end{pmatrix} (2\sqrt{\pi})^{-\frac{1}{2}}\,\mathcal{H}_0(\hat{y}) & n=-1 \end{cases} \tag{2.38}$$

having applied an appropriate constant to ensure $\mathbf{K}$ has natural units and where the normalization constant is:

$$\frac{1}{N_{n,r}^2} = \frac{\sqrt{\pi}}{c\beta}\left[(c\beta)^{-1}(\nu_{n,r}^2-c^2k^2)^2+(n+1)(\nu_{n,r}-ck)^2+n(\nu_{n,r}+ck)^2\right], \quad n \geq 0$$

The dispersion relation is summarized as:

$$\text{for } n>0 \qquad \frac{\nu_{n,r}^2}{c\beta}-\frac{c}{\beta}k^2+c\frac{k}{\nu_{n,r}}=2n+1 \qquad r=\begin{cases} 0 & \text{Rossby} \\ 1 & \text{inertia gravity} \\ 2 & \text{inertia gravity} \end{cases}$$

$$\text{for } n=0 \qquad \nu_{0,r}=\begin{cases} -\frac{c}{2}k+\frac{1}{2}\sqrt{c^2k^2+4c\beta} & r=1 \\ -\frac{c}{2}k-\frac{1}{2}\sqrt{c^2k^2+4c\beta} & r=2 \end{cases} \qquad \text{“n = 0”}$$

$$\text{for } n=-1 \qquad \nu_{-1,2}=-ck \qquad r=2 \qquad \text{Kelvin Wave}$$

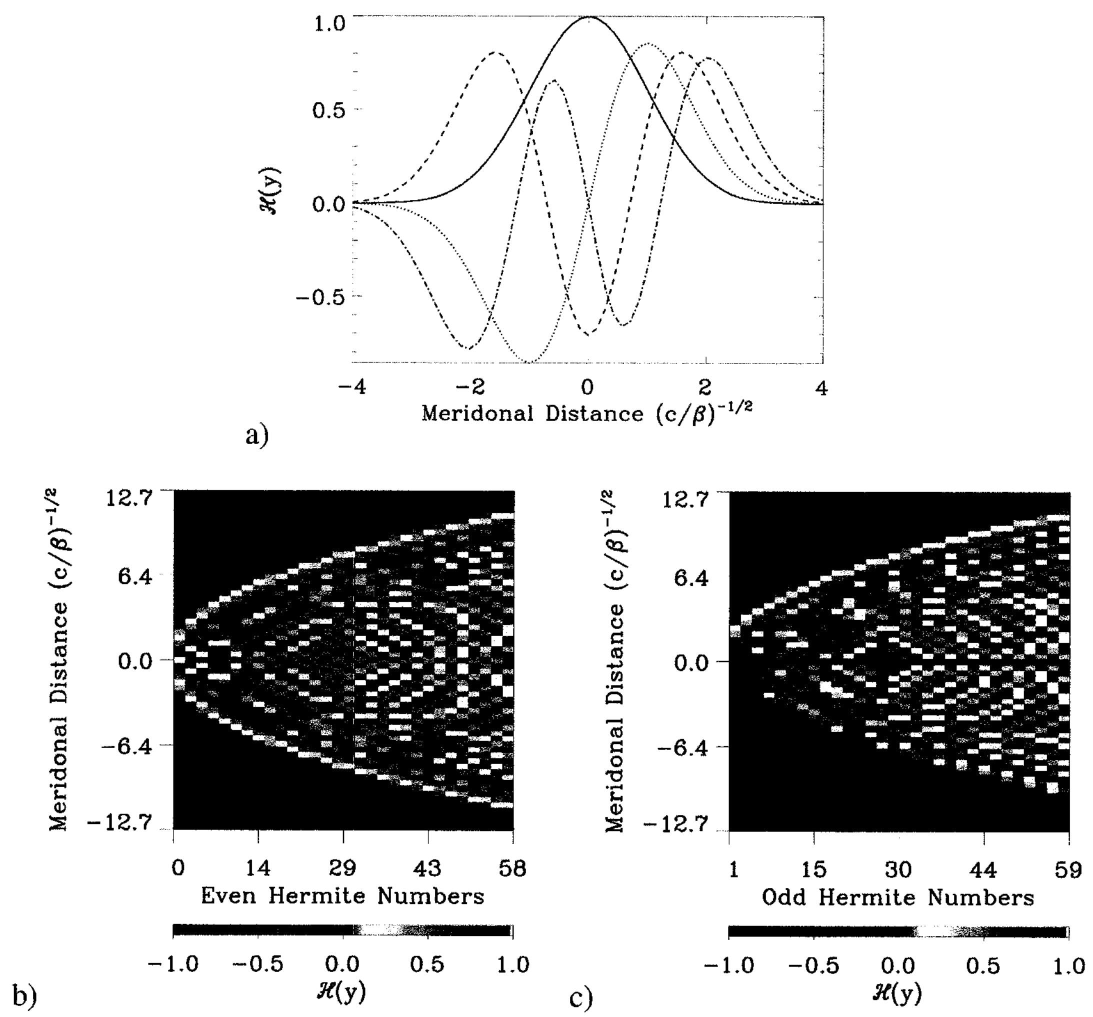

Figure 2.6: Non-dimensional plots for the form of the first (a) four, (b) even and (c) odd fifty nine $\mathcal{H}_n$ functions

2.6. Interactions Between Forcing and the System

For a single spectral wave (n, r, k), the spectral form of the β-plane system (2.35) can be written as;

$$\frac{\partial \ln W(t)}{\partial t} = -\epsilon + i\nu + \frac{F(t)}{W(t)} \tag{2.39}$$

The system state $W(t)$ and forcing $F(t)$ can be expressed in Euler's form as:

$$W(t) = A(t)e^{i\theta(t)} \tag{2.40a}$$

$$F(t) = B(t)e^{i\phi(t)} \tag{2.40b}$$

where A and θ represent the amplitude and phase of the wave in the system, respectively, and B and ϕ are the amplitude and phase of the forcing function. Given (2.40a) and (2.40b), then:

$$\frac{F(t)}{W(t)} = \frac{B(t)}{A(t)}e^{i\delta\theta(t)} = \frac{B(t)}{A(t)}\left(\cos(\delta\theta(t)) + i\sin(\delta\theta(t))\right) \tag{2.41}$$

where $\delta\theta(t) = \phi(t) - \theta(t)$ is the phase difference between the forcing and wave. On substituting (2.40) and (2.41) into (2.39) and omitting the notation of time dependance for convenience, then:

$$\frac{\partial \ln A}{\partial t} + i\frac{\partial \theta}{\partial t} = -\epsilon + i\nu + \frac{B}{A}(\cos(\delta\theta) + i\sin(\delta\theta)) \tag{2.42}$$

The real and imaginary parts of this expression thus yield a pair of predictive equations for the amplitude and apparent frequency (ω) of the forced system:

$$\frac{\partial A}{\partial t} = -\epsilon A + B\cos(\delta\theta) \tag{2.43}$$

$$\omega \equiv \frac{\partial \theta}{\partial t} = \nu + \frac{B}{A}\sin(\delta\theta) \tag{2.44}$$

and hereafter ν is referred to as the intrinsic frequency of the system. Under conditions of zero forcing ($B = 0$), the apparent frequency (ω) and intrinsic frequency (ν) are the same.

2.6a. *Interpretation of the Amplitude Equation*

The amplitude equation (2.43) is related to the total available energy, henceforth referred to as the 'energy'. The energy equation derives by taking the dot product of $\mathbf{W}$ with (2.15) producing the following equation for energy at a point (x, y):

$$\frac{1}{2}\frac{\partial}{\partial t}\overbrace{(u^2 + v^2 + \phi^2/c^2)}^{\text{Total Available Energy}} = \underbrace{uF_u + vF_v + \phi/c^2 F_\phi}_{\text{Source Term}} - \underbrace{\epsilon(u^2 + v^2 + \phi^2/c^2)}_{\text{Damping}} - \underbrace{\left(\frac{\partial(u\phi)}{\partial x} + \frac{\partial(v\phi)}{\partial y}\right)}_{\text{Flux Terms}} \tag{2.45}$$

where we note that all quantities on the right hand side have units of power. The damping term is simply proportional to the energy and the flux term depends on the state of the flow at a point. The source term is of the form $\mathbf{W} \cdot \mathbf{F}$, which implies that the effect of a forcing will depend on the state of the system and will be non-linear.

We can now relate this discussion back to forced wave interactions by invoking Parsevals relation which states:

$$\int_{-\infty}^{\infty} f(x)g^*(x)dx = \int_{-\infty}^{\infty} \hat{f}(k)\hat{g}^*(k)dk$$

Where $\hat{()}$ denotes the Fourier transform, and $()^*$ the complex conjugate, as before. Writing (2.45) in matrix form and noting that the dot product is of the form $(\mathbf{W}\cdot\mathbf{W}) = (u^2+v^2+\phi^2/c^2)$, then :

$$\left(\frac{1}{2}\frac{\partial}{\partial t}+\epsilon\right)(\mathbf{W}\cdot\mathbf{W}) = (\mathbf{W}\cdot\mathbf{F}) - \left(\frac{\partial(u\phi)}{\partial x}+\frac{\partial(v\phi)}{\partial y}\right)$$

Integrating over the entire horizontal domain, noting that the flux terms will be zero on a periodic domain or as the perturbations $\rightarrow$ zero at $\pm\infty$, then yields :

$$\left(\frac{1}{2}\frac{\partial}{\partial t}+\epsilon\right)\int_{-\infty}^{\infty}\int_{-\infty}^{\infty}(\mathbf{W}\cdot\mathbf{W})\,dxdy = \int_{-\infty}^{\infty}\int_{-\infty}^{\infty}(\mathbf{W}\cdot\mathbf{F})\,dxdy$$

Using Parsevals relation, this becomes

$$\left(\frac{1}{2}\frac{\partial}{\partial t}+\epsilon\right)\int_{-\infty}^{\infty}\int_{-\infty}^{\infty}\left(\hat{\mathbf{W}}\cdot\hat{\mathbf{W}}^*\right)dkdy = \int_{-\infty}^{\infty}\int_{-\infty}^{\infty}\left(\hat{\mathbf{W}}\cdot\hat{\mathbf{F}}^*\right)dkdy \tag{2.46}$$

where we recognize that this is the form of the inner product if the integration over y is non-dimensional. Using the definition of the inner product (2.31) we can write the left hand side as:

$$\begin{aligned}\int_{-\infty}^{\infty}\left(\hat{\mathbf{W}}\cdot\hat{\mathbf{W}}^*\right)dy =& \sqrt{c^5/\beta}\left(\hat{\mathbf{W}},\hat{\mathbf{W}}\right)\\ =& \sqrt{c^5/\beta}\left(\hat{\mathbf{W}},\sum_{n,r}W_{n,r}(k,t)\mathbf{K}_{n,r}(k,y)\right)\\ =& \sqrt{c^5/\beta}\sum_{n,r}W_{n,r}W_{n,r}^*\\ =& \sqrt{c^5/\beta}\sum_{n,r}|W_{n,r}|^2\end{aligned}$$

Then (2.46) becomes

$$\left(\frac{1}{2}\frac{\partial}{\partial t}+\epsilon\right)\int_{-\infty}^{\infty}\sum_{n,r}|W_{n,r}|^2dk=\int_{-\infty}^{\infty}\sum_{n,r}|W_{n,r}||F^*_{n,r}|dk$$

which states that the energy in the system ($W_{n,r}$) is modified by the energy in the forcing ($F_{n,r}$) convolved with the system and damps proportional to the energy in the system, as expected from (2.45). Expressing the total domain energy in physical space:

$$\begin{aligned}\int_{-\infty}^{\infty}\int_{-\infty}^{\infty}\frac{1}{2}(u^2+v^2+\phi^2/c^2)dxdy &= \sqrt{c^5/\beta}\sum_{n,r}\int_{-\infty}^{\infty}\frac{1}{2}|W_{n,r}|^2(k,t)dk\\ &= \sqrt{c^5/\beta}\sum_{n,r}\int_{-\infty}^{\infty}\frac{1}{2}A^2_{n,r}(k,t)dk \qquad (2.47)\end{aligned}$$

So that in multiplying (2.43) by A, we obtain a predictive equation for how the energy of a single wave in the system is affected by the forcing, i.e.:

$$\frac{\partial\frac{1}{2}A^2}{\partial t}=-\epsilon A^2+AB\cos(\delta\theta) \qquad (2.48)$$

This equation implies the occurrence of three regimes of interaction between the wave and its forcing, expressed through the $\cos(\delta\theta)$ term which can also be thought of as arising from the dot product between the wave and its forcing. In the first regime, the forcing and wave are positively correlated or 'in-phase' occurring when $cos(\delta\theta) > 0$. The second regime is characterized by a negative correlation or 'out of phase' interaction in which $cos(\delta\theta) < 0$. The third regime is one that results in no energy change. The non-linear aspect in (2.48) is captured through the product term AB and, as expected, the damping is proportional to the current energy of the wave. From (2.47), A^2 relates to the energy in the system and we refer to the forcing term in (2.48) as the *real* power.

2.6b. Interpretation of the Phase Equation

Equation (2.44) can be written in terms of phase speed:

$$c_a = c_p + \frac{B}{kA}\sin(\delta\theta) \tag{2.49}$$

where $c_a = \omega/k$ and $c_p = \nu/k$ are the apparent and intrinsic phase speeds, respectively. According to (2.49) the change in phase speed depends on the ratio of the amplitudes of the wave (A) and forcing (B), the wavenumber (k) and the phase difference between the wave and forcing as expressed by the $\sin(\delta\theta)$ term. By multiplying (2.44) by A^2 we obtain:

$$\omega A^2 = \nu A^2 + AB\sin(\delta\theta) \tag{2.50}$$

which is also an equation of power and since it derives from the imaginary part of the system the quantities of (2.50) do not directly contribute to the the total energy of the system (i.e. 2.45). Given that the phase equation relates to the apparent phase speed we suggest, by analogy, that (2.50) then relates to the apparent speed of energy propagation. For example, energy propagates at the intrinsic phase speed for the unforced case ($B = 0$). Furthermore, the net effect of the energy-phase equation (2.50) is always zero when summed over all (k, n, r) as every eigenvalue ($\nu_{n,r}$) for $k > 0$ has an odd counterpart for $k < 0$. Although (2.50) does not directly describe the state of the energy of the system, we conjecture that the equation describes the amount of energy being moved within the system and as such, we refer to the forcing term as the *radiant* power.

It is tempting to interpret both (2.49) and (2.50) as a change in physical wave speed, however, we maintain that it is impossible to alter the speed of a wave other than by altering the properties of the medium in which it is propagating. Hence, while the ***apparent*** solution permits the change of phase and energy speed, the actual wave and energy always propagate at their intrinsic speeds, easily verified when the forcing is turned off.

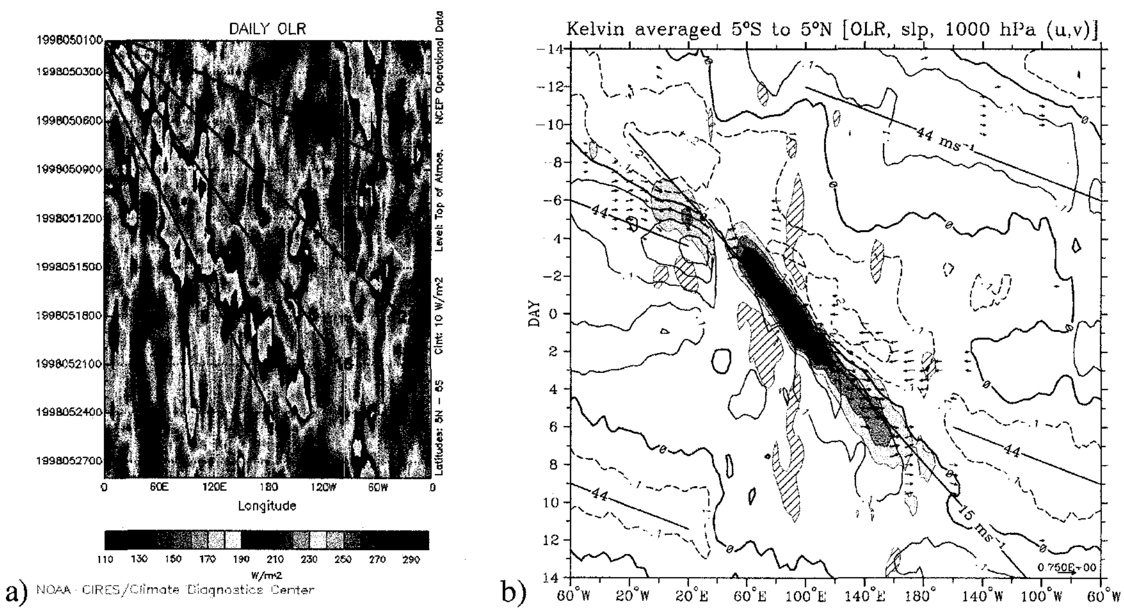

Figure 2.7: (a) depicts a Hovmoller of the Outgoing Longwave Radiation (OLR) observational data averaged from 5N to 5S for the period May 1 to May 28, 1998 superimposed with 10, 15, 22 and 44 ms^{-1} phase lines for reference. (b) is a reproduction from Wheeler et al. (2000) spectrally regressed composite analysis of the Kelvin wave, depicting the anomalous OLR, surface level pressure and wind field associated with the wave.

2.7. General Wave Behavior Under Steady Propagating Forcing

Consider a general forcing of the form

$$\mathbf{F}(x,y,t) = \begin{pmatrix} F_u \\ F_v \\ F_\phi \end{pmatrix} G(x - c_f t)M(y)T(t) \tag{2.51}$$

where c_f denotes the propagation speed of the forcing. If we assume steady forcing, then $T(t)$ = constant. The Fourier transform of (2.51) can be generalized for any specified propagation speed c_f by applying a Doppler shift to (2.44) as in Lindzen (1967) and Schubert and Masarik (2006). Applying the Fourier transform (2.16) to $\mathbf{F}(x,y,t)$ with

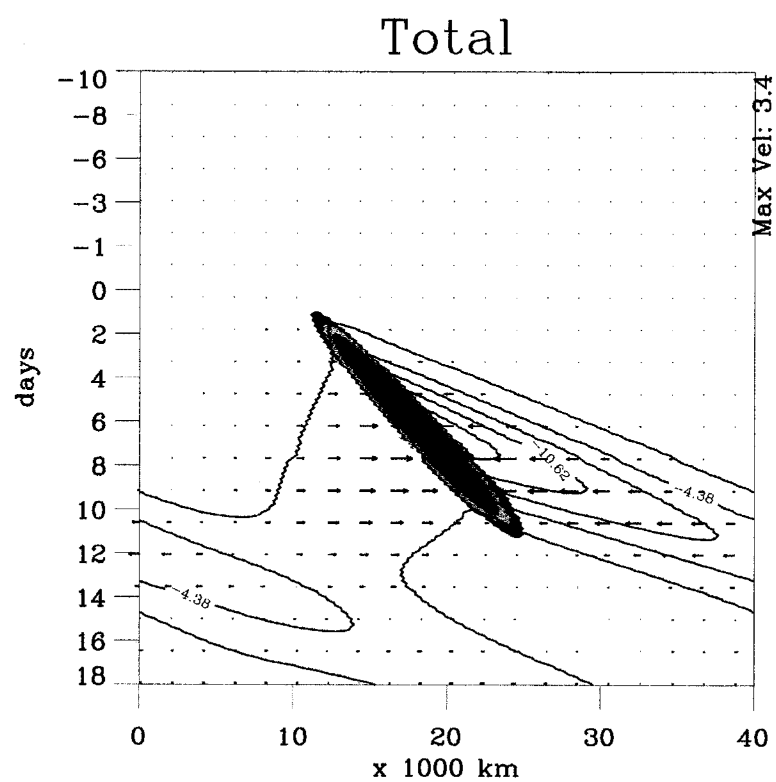

Figure 2.8: Time-space Hovmoller representation of the forced response from a Gaussian forcing propagating to the east at 15 ms^{-1}.

$c_f = 0$, followed by the meridional transform (2.31), then a transformed forcing of the form $F_{n,r}(k) = \hat{G}(k)M_{n,r}(k)T(t)$ results, where $M_{n,r}(k) = (M(y), \mathbf{K}(k,y))$.

Note that the meridional transform $M_{n,r}(k)$ is a function of k as an indirect result of the natural scaling of specific waves in the β-plane system towards particular k, as depicted in Figs. 2.2 and 2.3. The amplitude of the geopotential and velocity vectors relate to the response from thermal and momentum forcings, respectively. For example, a Kelvin wave responds equally to any forcing of any size while a Rossby wave responds naturally to horizontally larger disturbances. The Kelvin wave also responds preferentially to equatorially centered disturbances whereas the Rossby wave prefers off equatorial disturbances. Furthermore, the Rossby wave preferentially produces off equatorial meridional flow while the Kelvin wave is strictly zonal. These figures serve as a first order tool for identifying what waves govern the observed flow and geopotential fields.

With the forcing now spectrally defined, we solve for $W_{n,r}(k,t)$ and introduce the Doppler shift to account for the movement of the forcing by replacing $\nu_{n,r}$ in (2.35) with $(\nu_{n,r} + c_f k)$:

$$\int_0^t \left(\frac{d}{dt'} + \epsilon - i(\nu_{n,r} + c_f k) \right) W_{n,r} dt' = \int_0^t F_{n,r} dt' \tag{2.52}$$

and

$$W_{n,r}(k,t) = F_{n,r}(k) \frac{1 - e^{[i(\nu_{n,r} + c_f k) - \epsilon]t}}{\epsilon - i(\nu_{n,r} + c_f k)} \tag{2.53}$$

for an initially undisturbed state.

2.7a. General Spectral Response

On decomposing (2.53) into Euler's form, the amplitude spectrum becomes:

$$A_{n,r}(k,t) = \hat{G}(k)M_{n,r}(k)e^{-\epsilon t}\left((-1+e^{\epsilon t}\cos[kt\delta c])^2 + e^{2\epsilon t}\sin^2[kt\delta c]\right)^{1/2}\left(\epsilon^2 + (k\delta c)^2\right)^{-1/2} \tag{2.54a}$$

$$\delta c(k) = \nu_{n,r}(k)/k + c_f \tag{2.54b}$$

where δc represents the difference between the intrinsic wave speed and forcing speed, recalling the convention that ν would be of opposite sign to c_f if the intrinsic wave traveled in the same direction as the forcing. The expression for the apparent frequency (ω), or phase speed, is cumbersome but simplifies under two conditions, noting that we have applied a Doppler shift back into the stationary reference frame and that an eastward propagating forcing corresponds to $c_f > 0$:

$$\omega = \begin{cases} -c_f k & \epsilon > 0 \quad t \to \infty \\ k\delta c/2 - c_f k & \epsilon = 0 \quad t \geq 0 \end{cases} \tag{2.55}$$

and note that for the damped case, the apparent frequency is also given by the second condition at $t = 0$ and adjusts towards the first in a non-linear manner (not shown). Thus, the second condition serves as an upper-limit to the apparent frequency. We also note that;

(i) A moving forcing acts as a filter, preferentially energizing waves of similar phase speed through the $k\delta c$ factors in (2.54a).

(ii) The first condition of (2.55) implies that once the system reaches steady state (i.e. $t \to \infty$), the apparent phase speeds for all waves, of any equivalent depth, exactly match the speed of the forcing. This situation is referred to as phase-locking for reasons explored in the next section.

(iii) $\omega = 0$ (stationary phase speed) results for two situations, the first being the system in steady state around a stationary forcing, just mentioned, and the second when the forcing moves at exactly the opposite speed to the intrinsic wave

(iv) If the forcing were turned off, all waves would once again propagate at their intrinsic speed, namely $\nu_{n,r}(k)/k$.

(v) According to (2.44), $\omega = \nu_{n,r}$ if $\sin(\delta\theta) = 0$ which occurs only if $c_f = c$, even when $\epsilon > 0$. By (2.50), this implies that the radiant power is zero and no energy propagates out of the forced region. This follows physically since the speed of the forcing, resultant wave and energy propagation are all the same. Furthermore, when $\sin(\delta\theta) = 0$, then $\cos(\delta\theta) = 1$, implying a resonance of the real power (2.48) which always occurs when the forcing and wave speeds are the same, ie $\delta c = 0$, also evident in (2.54a).

2.7b. The Steady State Response

The time varying components of the damped solution simply characterize the transient behavior as the system evolves to steady state. In this way, the steady state solution represents the eventual state to which any steady input evolves. The steady state solution follows by taking the limit $t \to \infty$ in (2.54a) producing:

$$A_{n,r}(k) = \hat{G}(k) M_{n,r}(k) \left(\epsilon^2 + [k\delta c]^2\right)^{-1/2} \tag{2.56}$$

Although δc is strictly a function of k, we can usefully consider all waves in terms of a mean propagation speed of some equivalent monochromatic wave. For example, Rossby waves exhibit only a slight variation in c_p for low wave numbers while mixed-Rossby gravity waves and inertia-gravity waves exhibit a stronger dispersion. Considering the Fourier transform of a Gaussian function, we can say that narrow spectral power corresponds to large physical solutions and visa-versa. Then, if $\delta c = 0$, we find that the spectral amplitude is only modified by a linear constant (ϵ^{-1}), meaning that the physical solution will have exactly the same physical size as the input forcing. If $\delta c \neq 0$, then we see that the final spectral amplitude varies as $[k\delta c]^{-1}$, thereby narrowing the spectral width. This implies that the domain of the physical space solution grows beyond that of the input forcing by a factor proportional to $1/\delta c$. This is a general property of dispersive waves since $\delta c \neq 0$ for all k. Hence, we now enunciate: *for any forcing on the linear beta-plane, only those forcings moving at a different speed to the intrinsic phase speed of the wave will cause the wave to scale to larger sizes, otherwise the response, and thus energy, is largely trapped in the forced region.* Therefore any coherent structure observed outside the region of forcing occurs because the forcing and waves propagate at different speeds.

2.7c. The Transient Response

Early in the evolution of the wave when t is small and when damping might be ignored, (2.54a) becomes:

$$A_{n,r}(k,t) = \hat{G}(k)M_{n,r}\begin{cases} |2\sin(kt\delta c/2)/k\delta c| & \delta c \neq 0 \\ t & \delta c = 0 \end{cases} \tag{2.57}$$

and recall from (2.54b) that δc is defined individually for every (k, n, r) combination. For the case of $\delta c = 0$, the forcing does not influence the scale of the wave but the amplitude grows continuously being a linear function of time. For the case of $\delta c \neq 0$, the forcing broadens the spectrum of the wave at a rate dependant on $k\delta c$ and the total time of interaction, which scales as ϵ^{-1} for the steady state. Interestingly, a constant forcing can only increase the amplitude if it interacts over a time range $t < 2\pi/k\delta c$, or multiples thereof, implying that larger waves (smaller k) will be more amenable to amplification. One notes that the point of maximum response is just half this time so that while larger waves will be more prevalent to positive influence, they take a long time to reach peak amplitude. Furthermore, short duration forcing will then preferentially energize larger $k\delta c$, that is smaller waves ($k \to \infty$) and wave types of much different phase speed ($\delta c \to \infty$). The reader is referred to Silva Dias et al. (1983) for a thorough analysis of the transient excitation of different waves.

Using the e-folding time scale of $t \propto \epsilon^{-1}$ for the steady state, we may define a natural wavenumber cut-off for which waves are energized, given by $k < 2\pi\epsilon/\delta c$. Finally, Wheeler and Kiladis (1999) note that the tropical OLR energy spectra, presumably associated with linear waves, appears red and we note that this is only occurs if $\delta c \neq 0$ or if the forcing function possesses the same red power spectrum. For the observed high energy synoptic and planetary scale waves, presumably generated by much smaller sub synoptic scale forcing, the former is true.

2.7d. *Example Solution for a 15 ms^{-1} Forcing*

We now demonstrate that much of the observed structure for a convectively coupled Kelvin wave (Fig 2.7b) can be obtained by considering the forced response for a vertical structure with phase speed $c = 44$ ms^{-1}. Chapter 3 provides more detailed discussion of the Kelvin wave solution. For the example presented, we define the forcing as Gaussian in form with $\sigma_x = 1000$ km, $\sigma_y = 300$ km centered on the equator and propagating east at 15 ms^{-1} with a Gaussian time scale of 8 days and a damping $\epsilon = (4 \text{ day})^{-1}$. Fig 2.8 presents a time-longitude style Hovmoller representation of the response in surface geopotential perturbation (i.e. SLP perturbation analogous to that of Fig 2.7b), surface wind and surface convergence, the latter considered a proxy for anomalously low OLR, averaged from -500 km to 500 km in the meridional direction, similar to the scale used by Wheeler et al. (2000). Two pressure signals are evident, a Rossby wave that propagates slowly to the west and a Kelvin wave signal propagating to the east. The point of minimum pressure and maximum zonal winds lie just east of the forcing, slowly extending out from this forcing in time. The non-disperive low pressure signal generated by the forcing propagates at the free wave speed (44 ms^{-1}) around the domain.

2.8. Phase Locking and its Stability

The concept of phase locked systems, which owes its origins to radio frequency engineering, involves the use of a feedback to synchronize a local event with some observable external event. This concept is also fundamental to many problems outside of purely electronic systems. The quantity controlled in such systems is the phase difference $\delta\theta(t)$ and its time derivative $\partial\delta\theta(t)/\partial t$. The phase difference is the difference of the phase of the signal of interest (i.e. the wave) and of the reference signal (i.e. the forcing), which we recall is denoted as $\theta(t)$ and $\phi(t)$, respectively. In simple terms, the system-generated signal θ is said to be phase coherent with the reference ϕ when their difference remains approximately constant over some specified time interval, i.e. if the derivative $\partial\delta\theta(t)/\partial t \rightarrow 0$. We note that phase locking requires non-linearity and the phase difference, $\delta\theta$, referred to as the phase error in engineering, need not be small.

From (2.55), we infer that convectively forced waves at steady state, or that are slowly varying, can also be thought of as a phase locked system. From this analogy we can derive a number of important properties of the solution. Under these slowly varying conditions, the ratio of the forcing to response $\left(\gamma = \dfrac{B}{A}\right)$ can be considered to be constant. By subtracting $\partial\phi/\partial t$, which we define as the forcing frequency (ν_f), from both sides of (2.44) we develop a predictive equation for $\delta\theta$:

$$\frac{1}{\gamma}\frac{\partial\delta\theta}{\partial t} = \frac{\nu - \nu_f}{\gamma} - \sin(\delta\theta), \qquad (2.58)$$

Since $\nu = c_p k$ and $\nu_f = c_f k$, then

$$\frac{1}{\gamma}\frac{\partial \delta\theta}{\partial t} = \frac{-k\delta c}{\gamma} - \sin(\delta\theta), \tag{2.59}$$

Figure 2.9 offers a conceptual presentation of (2.59) adapted from Viterbi (1966). The figure identifies null points at those values of $\delta\theta$ where $\partial\delta\theta(t)/\partial t = 0$. A null point is defined as stable if under some perturbation the system returns to the same null point, this being determined by the sign of the derivative in the direction of the perturbation, while an unstable null point will cause the system to evolve, possibly to another null point. The resultant trajectory of the system at the null points are represented by heavy arrows in the figure and clearly demonstrate the stable and unstable null points. The conditions of stable and unstable phase locking can be written as follows:

$$\begin{aligned} \delta\theta_{\text{stable}} &= 2m\pi - \sin^{-1}\frac{k\delta c}{\gamma} \\ \delta\theta_{\text{unstable}} &= (2m-1)\pi + \sin^{-1}\frac{k\delta c}{\gamma} \qquad m = 0, \pm 1, \pm 2, ... \end{aligned} \tag{2.60}$$

which describe a repeating loop of period 2π. If $k\delta c \neq 0$, then phase lock can only occur if the forcing and wave are out of phase since no null point exists at $\delta\theta = 0$. Note that the sign of δc depends on two factors: the direction of the wave and whether the forcing is moving faster than the wave. For example, an eastward moving wave and forcing is defined by $\delta c = -c_p + c_f$ so that if the wave moves faster than the forcing ($c_p > c_f$), $\delta c < 0$, implying that the first stable null point for all waves exists at $0 > \delta\theta > \pi/2$, which physically means the response leads the forcing in the east direction. If the forcing propagates faster than the wave, the response then lags the forcing noting that these arguments are clearly symmetrical for westward moving waves.

The phase lock equation (2.59) sets limits on conditions under which phase lock occurs. Since phase locking occurs when $\sin(\delta\theta) = \dfrac{-k\delta c}{\gamma}$ and since $|\sin(\delta\theta)| \leq 1$

then:

$$\left|\frac{k\delta c}{\gamma}\right| \leq 1 \tag{2.61}$$

is the condition for phase locking the wave to the forcing. The implications of this condition for convectively-coupled waves are as follows:

(i) convective forcing and waves of similar speeds (i.e. $\delta c \to 0$) will phase lock more readily but for such circumstances the response of such a system is trapped in or near the region of forcing. Furthermore, if $\delta c = 0$, the waves will always be in phase but are not in phase-lock since phase-lock requires the response wave to change speed to acquire the other. We illustrate in chapter 3 that $\delta c \to 0$ cannot support the maintenance of the coupled system.

(ii) larger scale waves (i.e. $k \to 0$) will phase lock more readily than smaller scale waves, suggesting that the observed coherent structures of a convectively coupled feature will preferentially be large;

(iii) the ability for the wave to phase-lock to convection will be highly dependent on the current energy of the wave and that of the forcing. For example, weakly forced systems with $B \to 0$ and thus $\gamma \to 0$ or highly energetic waves ($A \to \infty$ and thus $\gamma \to 0$) will tend not to phase lock. Thus the parameter γ provides some measure of the ability of the wave to couple to and feedback back on its forcing.

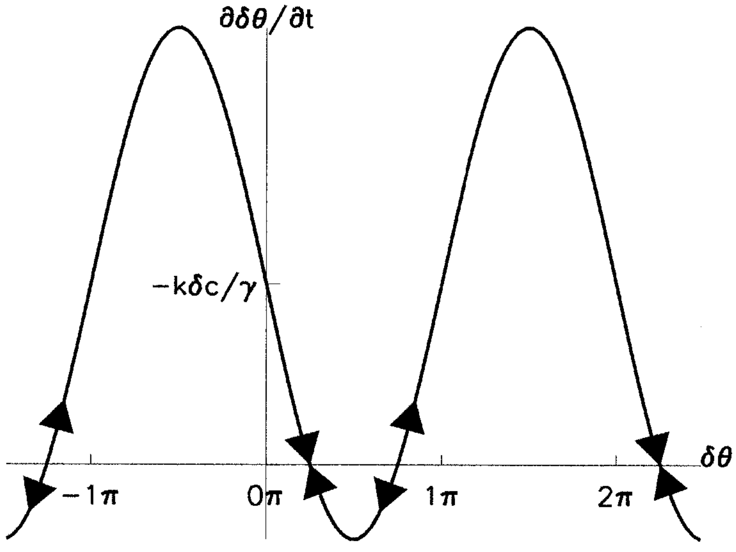

Figure 2.9: Phase-Plane plot of system trajectory. System trend in phase lock is marked by arrows from the null position. Adapted from Fig 3.2 of Viterbi (1966).

2.9. Summary

In developing the solution for forced waves, we conjecture that the forcing and the wave naturally propagate at different speeds where the difference between the speed of the forcing and the theoretical speed of the wave, δc, is an essential parameter of the particular solution. The particular solution of forced waves was shown to be governed by two characteristic equations, the first for the amplitude of the wave response and the second for the frequency (phase speed) of the wave response. Using Parseval's relation, the amplitude equation was shown to be directly related to the energy of the system and thus the forcing term in this equation is referred to as the 'real' power. The phase equation does not contribute to the energy of the system directly but it is conjectured that this equation governs the apparent propagation of energy from the region of forcing and the forcing term in this equation was termed the 'radiant' power. It also should be remarked that the forced wave solutions introduced require consideration of the entire spectrum of waves and notably waves of wavenumber ($k < 0$), which are traditionally ignored in most representations of the dispersion diagram.

The apparent frequency of the wave response for the case of a damped, forced wave was shown to vary in a stationary reference frame between $k\delta c/2 - c_f k$ and $-c_f k$, the latter implying phase locking of all waves of all equivalent depths to the forcing speed. However, the movement of the forcing acts as a filter, preferentially energizing waves of similar intrinsic phase speed and while resonance occurs for waves with $\delta c = 0$, the response is shown to be trapped (i.e. radiant power is zero). It thus followed that if the observed flow structure around a convectively-coupled feature is attributable to forced linear waves, it must be for waves in which $\delta c \neq 0$. Furthermore, if the observed domain energy spectrum is also attributable to forced linear waves, it too only follows if $\delta c \neq 0$, nullifying the apparent paradox that attempts to match the speed of the wave to that of the forcing.

The notion of phase locking of the steady convectively coupled wave, which in this study refers to a wave response that couples to the forcing, was used to develop a number of properties of the coupled system. The properties that govern phase-locking of the wave to the forcing were introduced drawing from the concepts developed from radio engineering. It was shown that the condition for phase locking is:

$$|k\delta c|/\gamma < 1$$

and, depending on the sign of δc, a stably phase-locked response either leads or lags the forcing in its respective propagation direction. The implications of this to the convectively coupled wave are;

(i) convective forcing and waves of similar speeds (i.e. $\delta c \rightarrow 0$) will phase lock more readily but for such circumstances the response of such a system is trapped in or near the region of forcing. Furthermore, if $\delta c = 0$, the waves will always be in phase but not phase-locked since phase-locking requires the response wave to change speed to acquire the other. We illustrate in the next chapter that $\delta c \rightarrow 0$ cannot maintain the coupled system.

(ii) larger scale waves (i.e. $k \rightarrow 0$) phase-lock more readily than smaller scale waves, suggesting that the observed coherent structures of convectively coupled waves are preferentially large;

(iii) the ability of the wave to phase-lock to convection will be highly dependent on the energy of the wave and that of the forcing. For example, weakly forced systems with $B \rightarrow 0$ and thus $\gamma \rightarrow 0$ or highly energetic waves ($A \rightarrow \infty$ and thus $\gamma \rightarrow 0$) will tend not to phase lock. Thus the parameter γ provides some measure of the ability of the wave to couple to and feedback back on its forcing.

Chapter 3

The Forced Kelvin Wave

Chapter 2 outlined a new theory of the dynamics of convectively coupled waves based on the general solution of a forced wave on a β-plane. One of the critical assumptions is that the forcing and the wave are assumed to propagate at different speeds with this difference, δc, being an essential parameter of the particular solution. A second key assumption is that a convectively-coupled wave is one that positively feedbacks on its forcing, an idea further explored here in the context of the forced Kelvin wave. We present the solution of a Kelvin wave forced by a Gaussian forcing and choose this example, not only because of its observed importance to the large-scale flow patterns of the tropics, but also because its solution can be expressed analytically. Assuming that the condition for positive reinforcement of the forcing by the wave occurs in regions of large-scale (low level) convergence, then we show how the solutions reveal that a convectively-coupled Kelvin wave can only sustain itself, when $\delta c < 0$. That is the forcing must propagate more slowly than the wave itself if the forcing that drives the wave is to be sustained by that wave.

Section 2 highlights the importance of the transient response for the Gaussian forced, undamped Kelvin wave and illustrates a number of the basic concepts introduced in chapter 2. In this example, we also underscore the ambiguity that arises in interpreting the wave solutions in spectral space in terms of the physical system. Section 3 explores the solutions of the Gaussian forced, damped Kelvin wave. In this section, the feedbacks between the wave and the forcing are used to identify the solutions that sustain the coupled system thereby representing the circumstances that are most likely those of the observed Kelvin wave features of the real atmosphere. Section 4 and 5 provide physical arguments for estimating characteristic values of δc for the convectively coupled Kelvin wave based on heuristic considerations involving both Bjerknes (1938) 'uniform' adjustment condition and Mapes (1993) stratiform mode lifting mechanism. These concepts lead to a linear scaling of δc as a function of forcing size and damping. These physical arguments are then connected back to the definitions of real and radiant power in section 5 where it is conjectured that the optimal configuration of convectively coupled waves is one in which energy is radiated away from the forcing at approximately the same rate at which it is created by the forcing. This then permits the calculation of the optimal propagation speed for all wave types on the β-plane and it is shown that for the forced Kelvin wave, this concept leads to the same scaling relationship between δc as a function of forcing size and damping as deduced from the more physical arguments of section 4. We then show how this simple relationship appears to predict the correct phase speed of convectively-coupled Kelvin waves and, possibly, the MJO.

3.1. The Undamped Kelvin Wave

3.1a. General Solution

The equations pertinent to solving the general forced Kelvin wave ($n = -1$ and $r = 2$) on a β-plane were developed in chapter 2 and are re-written here for reference, beginning with the governing spectral equation:

$$\left(\frac{\partial}{\partial t} + \epsilon - i\nu_{n,r}\right) W_{n,r} = F_{n,r} \tag{3.1}$$

where $W_{n,r}$ is the wave solution to which a normal mode meridional transform in y and Fourier transform in x is applied. This transform is defined by:

$$W_{n,r}(k,t) = \left(\hat{\mathbf{W}}(k,y,t), \mathbf{K}_{n,r}(k,y)\right) \tag{3.2a}$$

$$\hat{\mathbf{W}}(k,y,t) = \sum_{n,r} W_{n,r}(k,t)\mathbf{K}_{n,r}(k,y) \tag{3.2b}$$

where

$$(\mathbf{f},\mathbf{g}) = c^{-2}\int_{-\infty}^{\infty}(f_1 g_1^* + f_2 g_2^* + \frac{1}{c^2} f_3 g_3^*)d\hat{y}$$

is the inner product of any two complex, three-component vectors, g^* denotes the complex conjugate. Similarly, $F_{n,r} = (\hat{\mathbf{F}}, \mathbf{K}_{n,r})$ is the meridional transform of the Fourier transformed forcing ($\hat{\mathbf{F}}$). For the Kelvin wave, the meridional transform Kernel ($\mathbf{K}$) is given by:

$$\mathbf{K}_{-1,2}(k,\hat{y}) = \begin{pmatrix} U(k,\hat{y}) \\ V(k,\hat{y}) \\ \Phi(k,\hat{y}) \end{pmatrix} = \begin{pmatrix} c \\ 0 \\ c^2 \end{pmatrix} (2\sqrt{\pi})^{-\frac{1}{2}}\, \mathcal{H}_0(\hat{y}) \tag{3.3}$$

recalling that $\mathcal{H}_0(\hat{y}) = e^{-\hat{y}^2/2}$. Consider in (3.1) a thermal forcing (i.e. a mass source/sink) in physical space of the form $F_\phi(x,y,t) = A'M(y)e^{-(x/\sigma_x)^2}$, where A' is a forcing constant in units of c^2/s, σ_x is the x e-fold scale of the convective disturbance that creates this forcing and $M(y)$ is a dimensionless meridional structure. Setting $\nu_{-1,2} = -ck$ and $\epsilon = 0$, we find that the solution of the undamped wave in physical space with respect to the reference frame of the moving forcing is;

$$\begin{pmatrix} u(x,y,t) \\ v(x,y,t) \\ \phi(x,y,t) \end{pmatrix} = \begin{pmatrix} c \\ 0 \\ c^2 \end{pmatrix} A'\sqrt{\pi}\sigma_x M_{-1,2}\mathcal{H}_0(\hat{y})\Psi(x,t) \tag{3.4}$$

where

$$\Psi(x,t) = \begin{cases} -\left(\mathrm{Erf}\left[\frac{x}{\sigma_x}\right] - \mathrm{Erf}\left[\frac{x+\delta ct}{\sigma_x}\right]\right)(2\delta c)^{-1} & \delta c \neq 0 \\ te^{-(x/\sigma_x)^2}(\sqrt{\pi}\sigma_x)^{-1} & \delta c = 0 \end{cases} \tag{3.5}$$

and $M_{-1,2} = (M(y), \mathbf{K}_{-1,2})$ has units of c^{-2}, $\delta c = -c + c_f$ has the same meaning as in chapter 2, being the difference between the forcing (c_f) and wave speed (c), and the quantity $\Psi(x,t)$ is hereafter referred to as the amplitude response. The spectral amplitudes of the solution are defined by (2.54a) and the predicted frequency with respect to a moving reference frame for the undamped Kelvin wave is given by $\omega = k\delta c/2$ (2.55). Physically, the solution (3.4-3.5) describes two wave fronts, one stationary with respect to the forcing and the other propagating away at a shifted wave speed with respect to the forcing. In a stationary reference frame this would appear as a response moving with the forcing and a wavefront moving ahead (or behind) at its intrinsic speed. These two wave fronts are commonly referred to as the 'forced' and 'free' oscillations, respectively, but we note they are produced by the interaction of the same wave with the forcing.

When $\delta c = 0$, the wave fronts become trapped within the region of the forcing according to (3.5), and also Fig. (3.1a) to be discussed below, yielding a physical solution proportional to the input forcing function multiplied by t (section 4 in chapter 2). It was argued in chapter 2 that observations of convectively coupled waves and energy spectra could only be explained for the case of $\delta c \neq 0$. In this case, the spectral amplitudes, which relate to the physical size of the wave in the x direction were shown to broaden in a manner proportional to δc whereas the physical space solution (3.5) broadens at a rate of exactly δc.

As mentioned, the physical solution for a single wave yields two wave fronts that propagate at different phase speeds, one with a speed equal to the forced response and the other with a speed equal to the free response. Performing a Two-Dimensional Fourier Transform (2DFT) in (x, t) on this physical solution defined for a stationary reference frame, identifies these same two propagating features, one with a characteristic frequency kc of the 'free' wave and the second with the frequency of the forcing, kc_f. Such features are also observed. Wheeler and Kiladis (1999), for example, find both 'dry' modes of equivalent depth $h = 200$m and 'forced' modes of much smaller equivalent depth ($h = 12 - 50$m). As commonly done, it is tempting to project the theoretical β-plane frequency (ω) to that derived from the 2DFT analysis of real data. However this frequency ($\omega = k\delta c/2$) does not represent any real wave front as it lies between the frequencies of the two real wave fronts. Thus the spectral wave properties of the forced problem cannot be simply projected onto 2DFT transformations of the real physical system. However, the β-plane frequency (ω) of a damped system, eventually evolves to the single frequency of the forcing according to (2.55) and to be shown later. In this case, the 2DFT view of the physical system and the β-plane frequency (ω) are the same since the wave is phase locked to the forcing and, as shown in the next section, both wave fronts appear to propagate at the speed of the forcing.

3.1b. Example Results

Figure 3.1a-c depicts the amplitude response (3.5) for a forcing of size σ_x = 1000 km respectively for δc = 0 m/s, -15 m/s and 15 m/s, noting that the scale in Fig. 3.1a is an order of magnitude larger than that used in Fig. 3.1b and c. The heavy solid line represents the forcing function and the various other lines are the wave solutions at t =

[12, 24, 72, 120] hrs. The amplitude response solution given by (3.5) for $\delta c = 0$ has exactly the same structure as the forcing function (Fig 3.1a) and grows linearly with t. We refer to this response as being trapped, as previously discussed. If we consider that the amplitude responses project onto the first baroclinic mode, then the amplitude responses shown represent the surface level responses. As the amplitude is proportional to the surface zonal wind (3.4), the convergence of this wind implies ascending motion and thus an environment conducive for a positive feedback on the forcing (convection). It is easy to verify from the derivative of (3.5) or its representation in Fig 3.1a that in the case of $\delta c = 0$, both convergence (highlighted by the vertical lines) and divergence (highlighted by the hatching) are trapped within the region of forcing while the amplitude continually amplifies in time. Since the divergence region also remains contained within the region of forcing, we propose that this half of the forcing region shuts down due to unfavorable effects of wave induced subsidence on convection. The result is a forcing now contained in the convergent region of the wave response being now half its original size. This then produces the same convergence-divergence pattern with half of that forcing now being shut down, and so on until the forcing is completely annihilated by the negative feedback of the Kelvin waves.

Although the above results are shown specifically for the Kelvin wave solution, the convergence/divergence feedback concept illustrated in this example extends to all waves and all vertical modes. Since the divergence of the general solution is $iku + \dfrac{\partial v}{\partial y}$, the divergence of the **K** kernel (2.38) is easily verified to be imaginary with respect to the thermal field thus producing a divergence field in quadrature with thermal forcing. In the case of dispersive waves, however, the response spreads since $\delta c(k) \neq 0$ for all k indicating that the divergence-convergence pattern is no longer confined solely to the forcing region. It can also be shown trivially that divergence will always be in quadrature with u momentum forcing but not the v momentum forcing.

The expressions given in (3.4-3.5) and illustrated in Fig. 3.1b and c demonstrate how

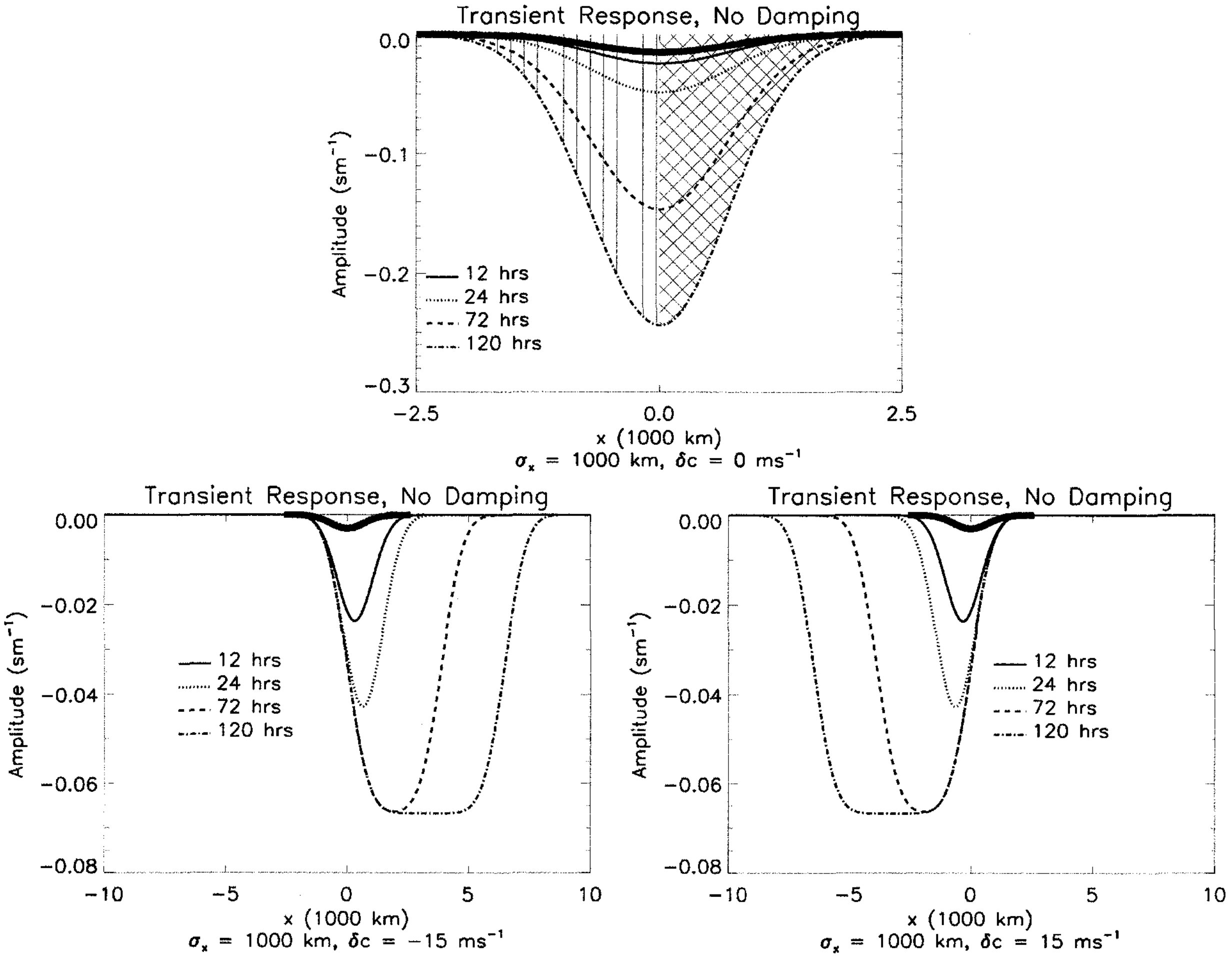

Figure 3.1: Amplitude portion of the undamped transient Kelvin Wave response described by (3.5) at time 12, 24, 72 and 120 hrs for (a) $\delta c = 0$ ms^{-1}, (b) $\delta c = -15$ ms^{-1} and (c) $\delta c = 15$ ms^{-1}. Note the heavy solid line in all figures represents the mass sink with a scale σ_x = 1000 km and that the amplitude in (a) is an order of magnitude larger than (b) and (c).

the size of the wave response in the x direction increases at a rate of δc. The results also show how the region of divergence propagates away from the forcing region for $\delta c < 0$ and, conversely, how the region of convergence propagates away from the forcing region when $\delta c > 0$. Initially (e.g. $t \sim 12$ hrs), the transient response is confined to the region of forcing such that half of this region experiences convergence and the other half divergence. As in the case of $\delta c = 0$, assuming that the mass sink is caused by some forcing related to convection and convergence, this is not an ideal configuration for sustaining the system. By time $t \to \sigma_x/\delta c$ (e.g. $t \sim 18$ hrs), the wave front has moved an e-fold out of the forcing region and the feedback of the Kelvin wave on the forcing would then be expected to enhance the forcing through the convergence that now exists over most of the forcing region. This favorable condition occurs only for $\delta c < 0$ (Fig. 3.1b). Conversely, the forcing region remains under divergence for all time for $\delta c > 0$, such that the wave is expected to suppress convection and negatively feedback on the forcing, in turn suppressing the wave. Again, we note that these arguments apply to all vertical structure functions.

3.2. The Damped Kelvin Wave

We know of no simple analytical solution in physical space for the damped Kelvin wave. The solution in spectral space, however, follows analytically from (3.1) and the physical space solution is obtained from a numerical application of the inverse Fourier transform. This numerical procedure is applied to a 40,000 km periodic domain (Fig 3.2) to produce the steady state amplitude response for a forcing with σ_x = 1000 km, ϵ = (4 day)$^{-1}$ and intrinsic wave speed $c = 45$ ms^{-1}. Figure 3.2a presents solutions for forcing propagation speeds less than the intrinsic phase speed (referred to as "sub-mach"), that is for $\delta c < 0$, whereas Fig. 3.2b presents solutions for $\delta c > 0$ ("super-mach"). In both figures, the propagation speeds are $|\delta c| = [5, 10, 15, 30]$ ms^{-1} and the heavy solid line, shown for reference, represents the forcing function multiplied by 10^4 so as to be visible on the scale of the diagram. We first note that all constituent waves are phase-locked to the forcing but that this does not imply that the wave energy travels at the forcing speed, rather that it is the *apparent* wave energy that travels with the forcing. Any perturbation applied to the forcing would move through the steady state solution until it too reached steady state and then appear to phase-lock. Taken together, the amplitude responses of both the super- and sub-mach solutions are symmetrical about the forcing for a given $|\delta c|$ except that the responses either lead or lag the forcing, respectively.

Of particular interest are the implied convergence/divergence regions relative to the domain of the forcing since these imply feedbacks to the forcing as discussed previously. For $|\delta c|$ sufficiently large, a stark contrast appears between the super-mach and sub-mach solutions. As in the undamped case, convergence is implied over the entire forcing region for the sub-mach solutions whereas divergence predominates the forcing region for the super-mach solutions, as found also in the undamped transient case. Whereas the undamped solution's divergence field was confined only to the wavefronts, the damped solutions divergence field now extends over the entire region of influence of the disturbance in the x direction, the scale of which is $R_{ix} \propto \delta c/\epsilon$. Finally, the special case of $\delta c = 0$ stands out with its large amplitude and, once again, confinement to the forcing region with the divergence field half out of phase with the forcing.

3.3. A Mechanistic View of the Forced Kelvin Wave Response

We now describe two concepts that, combined, offer a mechanistic view point of the coupling between convection and the vertical structure of the wave it excites and how these influence the propagation of the convectively coupled system. The first concept is that of Bjerknes (1938) who hypothesized that the optimum energetic configuration for

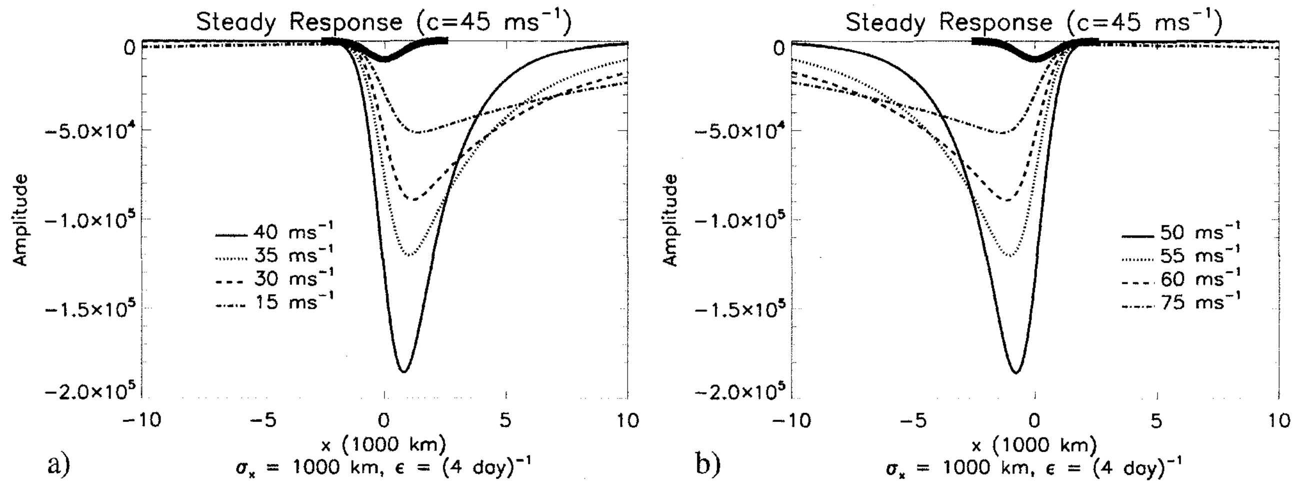

Figure 3.2: Steady, damped ($\epsilon = (4\text{ day})^{-1}$) Kelvin wave responses of a mass sink ($\sigma_x = 1000$ km) for various propagation speeds (a) slower than the intrinsic phase speed ($c = 45\text{ ms}^{-1}$) and (b) faster than the intrinsic phase speed. Note that the heavy solid line in both figures represents the location of mass sink and the resonance case ($\delta c = 0$) is included in both figures. Only half of the spatial domain is presented.

a convective cloud of finite width is one that minimizes the ratio of the updraft area to subsidence area. This implies that the "uniform adjustment" by dry adiabatic descent (subsidence) is spread over large regions resulting in a small magnitude which then has little influence on the environmental temperature that effects the buoyancy of convection. Bretherton and Smolarkiewicz (1989) view such an 'adjustment' process as a wave response. The second aspect of the wave response considers the view of Mapes (1993) who argued that the 'stratiform' response is conducive to initiating new convection. These ideas are conceptually brought together in Fig. 3.3 to offer a mechanical view of how a convectively coupled Kelvin wave propagates and influences its environment. Shown is a conceptual representation of the propagating cloud field (c_f = 15 ms^{-1}) in the convective region of a convectively coupled Kelvin wave. This representation is broadly based on observations by Straub and Kiladis (2002) and depicts deep cumulus heating followed by 'top-heavy' or stratiform heating. The top panel indicates the mass source/sink at the surface induced by idealized heating profiles in the convective region, where the heating profiles are assumed to be Gaussian. We simplify the vertical struc-

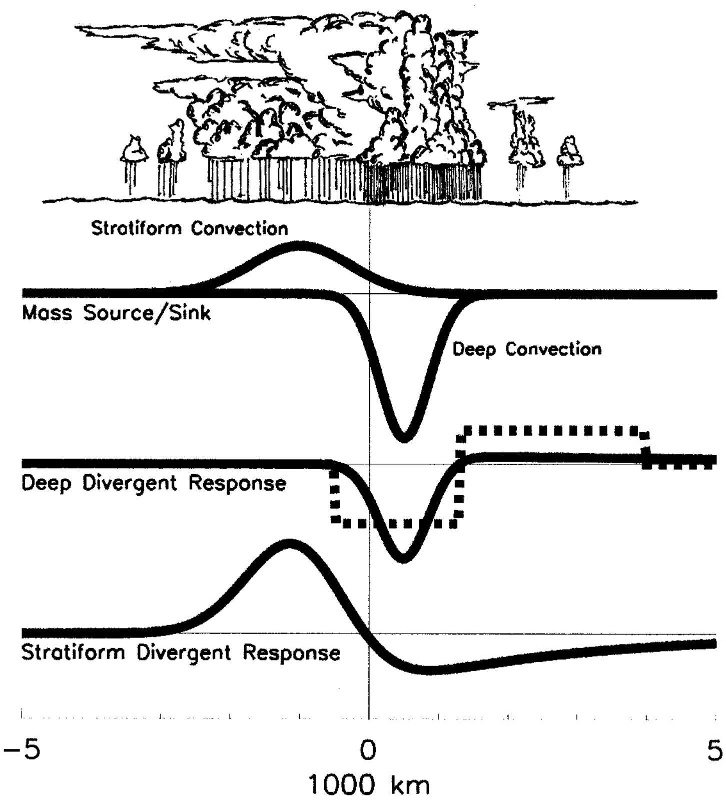

Figure 3.3: Conceptual view of a convectively coupled Kelvin wave moving at 15 ms^{-1} with deep heating leading stratiform heating. The surface level, steady, divergence response due to the deep (44 ms^{-1}) and stratiform heating (23 ms^{-1}) is presented separately. Note that the dotted line for the deep divergent response notionally represents Bjerknes (1938) uniform adjustment view of this mode. $\epsilon = (4 \text{ day})^{-1}$.

ture of these heating profiles and only consider the deep cumulus heating as projecting purely onto the first baroclinic mode (the deep mode c = 44 ms^{-1}) and the stratiform heating as projecting purely onto the second baroclinic mode (the stratiform mode c = 23 ms^{-1}). In this manner, the deep mode produces a mass sink at the surface (low pressure) and the stratiform mode produces a mass source at the surface (high pressure). For convenience, the 0 km line represents the approximate transition line between these two modes. The second and third panel respectively depict the divergent responses due to the deep and stratiform heating functions and the implications of these responses will be discussed shortly.

We first consider the deep mode within the Bjerknes (1938) deep adjustment context. In doing so, however, we note a few fundamental differences between Bjerknes' original ideas which apply to a cumulus scale constant mass flux that is balanced by subsidence fixed over some prescribed area, notionally represented by the dotted line in Fig. 3.3, panel 2. In considering the region of (deep convective) forcing as analogous to the Bjerknes cumulus scale, we propose that the adjustment by deep convection is restricted to the region described by the forced wave response, which is inhomogeneous. Viewed in this light and in contrast to Bjerknes, the mass flux related to the forcing is not constant but is a function of the response of the fluid. Nevertheless, the basic tenet of Bjerknes' is that dry adiabatic descent will tend to stabilize the thermodynamic profile and thus set a limiting lapse rate for saturated convection such that reducing the magnitude of the subsidence by spreading it over large areas is energetically desirable for supporting a convective system as it propagates into the adjusted region. Although Bjerknes' ideas suggest that the size of this area of divergence would ideally be as large as possible, we also suggest that the location of this divergence is important to the mechanics of the convective system. Using the region of divergence as a proxy for the region of adjustment, then the total adjustment relates directly to the total divergence which can be expressed as;

$$\int_a^b \frac{\partial u}{\partial x} dx = u(b) - u(a), \tag{3.6}$$

which describes the divergence over a portion of the wave extending from $a \rightarrow b$. Setting a to the point of maximum zonal velocity and $b = \infty$ yields the total adjustment, $u(a)$, since $u(\infty) \rightarrow 0$ for $t < \infty$ in both the damped and undamped cases.

The undamped solution (3.5) indicates that the maximum amplitude is proportional to $c/\delta c$. For $|\delta c| \rightarrow \infty$, this implies that $u(a) \rightarrow 0$ and thus zero thermodynamic adjustment. Furthermore, the faster the intrinsic wave speed (i.e. the larger is c in Eqn 3.5), the larger the adjustment for a given forcing (A'). While conditions of zero adjustment appear optimal according to Bjerknes, it also implies that the forcing region must be one of zero convergence by mass continuity, which clearly would not support continued convective development. As shown earlier, the response and thus convergence is maximized for the case of $\delta c = 0$ but so too is subsidence which now occurs directly within the region of forcing. We may conclude that to satisfy Bjerknes' arguments and place the location of adjustment outside the region of forcing while maintaining convergence within this region, $-\infty < \delta c < 0$ implying that some optimal value presumably exists between the unphysical bounds $\delta c = -\infty$ and $\delta c = 0$.

As discussed by Mapes (1993), the stratiform mode response induces low-level convergence away from the forced region which is then conducive to further convective development in a region local to the previous convective events. We again cast this cumulus scale argument into the large scale context of a convective coupled Kelvin wave and conjecture that this is the mechanism of propagation of the convective system. Observations of convectively coupled waves (Nakazawa 1988; Straub and Kiladis 2002, and others) depict the envelope of the large scale convective system as moving through the generation of new convection developing in previously clear air leading the system.

This implies that the forcing that triggers these new cells is not trapped further implying that $\delta c \neq 0$. It then follows from previous discussion that $\delta c < 0$ is the only condition that would support the Mapes' gregarious convection arguments on the large scale. As argued previously, $\delta c \rightarrow -\infty$ is the condition for zero response and that some optimal value presumably exist for this vertical mode too. We also note that the stratiform induced response in the region of stratiform forcing will further promote stratiform convection, as is true for all vertical modes if $\delta c < 0$.

We have argued that both $\delta c \rightarrow -\infty$ and $\delta c \rightarrow 0$ are conditions that do not support the convectively coupled wave system. However, these arguments are framed around only two vertical modes whereas convection generally excites a spectrum of vertical modes all with different equivalent depths (Lindzen 1967; Wu et al. 2000b; Lindzen 2003) and presumably different mechanistic processes. We will only attempt to address how the fundamental response of forced waves on the β-plane relate to the two modes considered as we view these as the most likely candidates that predominantly affect the large scale region, to be discussed next. At this juncture, we can confidently say that for a positive response between the Kelvin wave and its forcing, the forcing propagation speed must be less than and *not* equal to the intrinsic phase speed (equivalent depth) or, alternatively, only those equivalent depths with associated phase speeds greater than the forcing speed will positively reinforce the forcing.

3.3a. Observational Implications

Gill (1980) first recognized that the scale of the wave response was set by the intrinsic phase speed of the wave, thus explaining the asymmetry in the east-west, Kelvin-Rossby wave couplet. Mapes (1993) appears to have been the first to term the effect of different vertical modes as causing a 'vertical dispersion' in the response of a forced fluid causing faster (deeper) waves to arrive sooner at farther locations. Wu et al. (2000b) termed this an effective gravity wave speed. These previous discussions were posed with respect to a stationary forcing and showed that under damped conditions, the x radius of influence is $R_{ix} \propto c/\epsilon$. We have shown that for a moving forcing, this scale is modified such that $R_{ix} \propto \delta c/\epsilon$. Furthermore, the meridional scaling factor is $\sqrt{c/\beta}$ so that faster waves also exhibit a larger scale in the y direction.

The fact that their is a scale of influence of different vertical modes forced by convective systems propagating at different speeds has a number of implications to the interpretation of observations. Different observational data sets and theoretical studies sometimes highlight the importance of one vertical mode over another (Yanai et al. 1973; Houze 1989; Mapes 1993; Johnson and Ciesielski 2000; Biello and Majda 2005, and others). However, due to the vertical dispersion of a forced fluid and damping within that fluid, one mode or equivalent depth may appear more prevalent than another as one moves away from the forcing function primarily as a consequence of the scale being observed. For example, a convectively coupled Kelvin wave moving at 15 ms^{-1} will produce a deep response with an area nearly 4 times larger to the east than the stratiform response and observations made in this region will predominantly reflect this deep response mode. This implies that observations are a function of their viewpoint and, in this manner, it is not surprising that the equatorial mean heating profile deduced from observations reflect mostly the fastest mode (Yanai et al. 1973; Johnson and Ciesielski 2000) while smaller observational space-time periods highlight the stratiform mode (Houze 1989; Mapes 1993; Mapes and Houze 1995) and sometimes yet smaller scales within the convecting region (Johnson et al. 1999).

3.4. On Estimating the Optimal Propagation Speed of Convectively Coupled Waves

It has been emphasized that a necessary condition for the maintenance of convectively coupled systems is $\delta c < 0$ and that the limits $\delta c = 0$ and $\delta c \to -\infty$ cannot support a convectively coupled wave. This suggests there exists some optimal δc that lies between these limits. Here, we introduce two arguments for estimating this optimal state.

3.4a. A General Method using Real and Radiant Power

From (3.9) and (3.11) in PGS1, the real (P_{real}) and radiant (P_{radiant}) powers of the wave are:

$$P_{\text{real}} = \epsilon A^2 \tag{3.7a}$$

$$P_{\text{radiant}} = -k\delta c A^2 \tag{3.7b}$$

and in steady state, (Eq 3.5 and 3.6 in PGS1):

$$A(k) = B(k)cos(\delta\theta(k))/\epsilon \tag{3.8a}$$

$$\delta\theta(k) = -Tan^{-1}(k\delta c/\epsilon) \tag{3.8b}$$

with all basis waves phase-locked to the forcing such that they propagate at the same speed as the forcing although each possess different phase shifts and amplitudes, producing the non-local response when $\delta c(k) \neq 0$. According to (3.7a) the amplitude is an even function about δc whereas $\delta\theta$ is not. Thus, a moving forcing acts as a form of symmetrical filter on the amplitude (energy) but is non-symmetrical with respect to phase shift, implying a non-symmetrical response, this being the cause for dichotomy in the sub and super mach solutions for the Kelvin wave (Fig 3.1) and now shown by (3.8b) to be generally true for all waves.

Setting $\nu_{-1,2} = -ck$ for the Kelvin wave and defining the forcing as before, the spectral forcing becomes:

$$B(k) = A'M_{-1,2}(k)\sigma_x e^{-k^2\sigma_x^2/4}/\sqrt{\pi} \tag{3.9}$$

Defining the total power in the same manner as the total energy, i.e. :

$$TP = \int_{-\infty}^{\infty} \frac{1}{2} P^2 dk \tag{3.10}$$

then the total real and radiant powers follow from (3.7), (3.8), (3.9) and (3.10):

$$TP_{\text{real}} = \frac{A'^2 \sigma_x}{\epsilon} \int_0^{\infty} e^{-\mu^2/2} \frac{d\mu}{1 + (\delta c \mu / \epsilon \sigma_x)^2} \tag{3.11a}$$

$$TP_{\text{radiant}} = \frac{A'^2 |\delta c|}{\epsilon^2} \int_0^{\infty} e^{-\mu^2/2} \frac{|\mu| d\mu}{1 + (\delta c \mu / \epsilon \sigma_x)^2} \tag{3.11b}$$

where $\mu = k\sigma_x$. We can relate these quantities to our previous discussion of the mechanistic view of the wave response in recalling that the real power relates to the adjustment or work by that wave while the radiant power relates to the location of this adjustment. For example, according to (3.11a), TP_{real} is maximized and $TP_{\text{radiant}} = 0$ when $\delta c = 0$ which was shown to be the case for maximum adjustment trapped within the location of the forcing. For $|\delta c| \to \infty$ corresponding to the case of zero adjustment, both total powers approach zero and no work is performed on the atmosphere.

Figure 3.4 compares the total power terms of a Kelvin wave of scale $\sigma_x = 200$ km and $\sigma_x = 1000$ km normalized by (σ_x/ϵ). In producing Fig. 3.4b we have not applied the absolute operator to δc in (3.11b) in an attempt to convey the direction of energy propagation relative to the forcing (negative TP_{radiant} results when energy moves ahead of the system as $\delta c < 0$). The forcing scale of $\sigma_x \approx 1000$ km is of scale similar to the composite results of Wheeler et al. (2000) which depict a forcing speed $c_f \approx 15$ ms^{-1}. We first consider the deep mode response, $c \approx 45$ ms^{-1}, then a $c_f \approx 15$ ms^{-1} implies that $\delta c \approx -30$ ms^{-1}. According to Fig 3.4a, $\delta c \approx -30$ ms^{-1} lies about two e-folds along the real power curve away from the resonance case of $\delta c = 0$ ms^{-1}. This small value of TP_{real} implies that the work done by the deep adjustment of the atmosphere is effectively minimized, broadly satisfying Bjerkens' condition. We illustrate this result

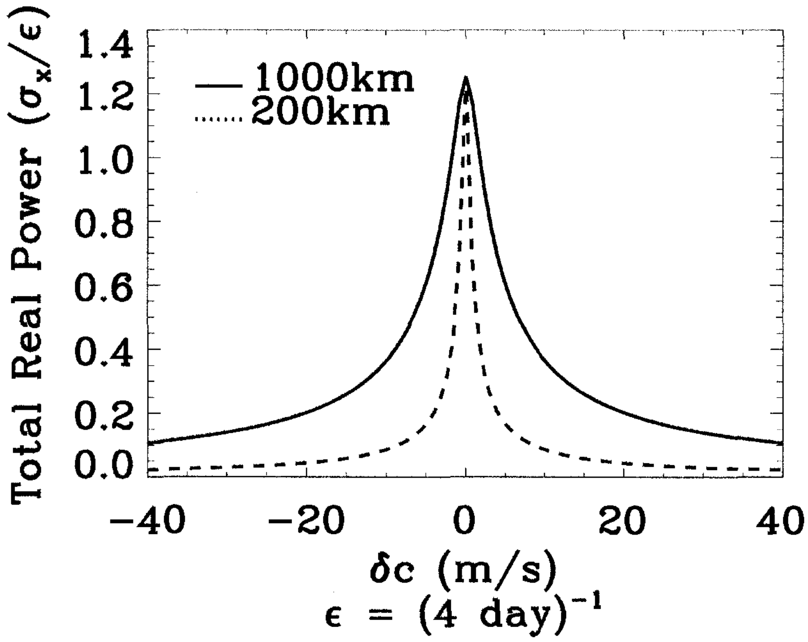

a)

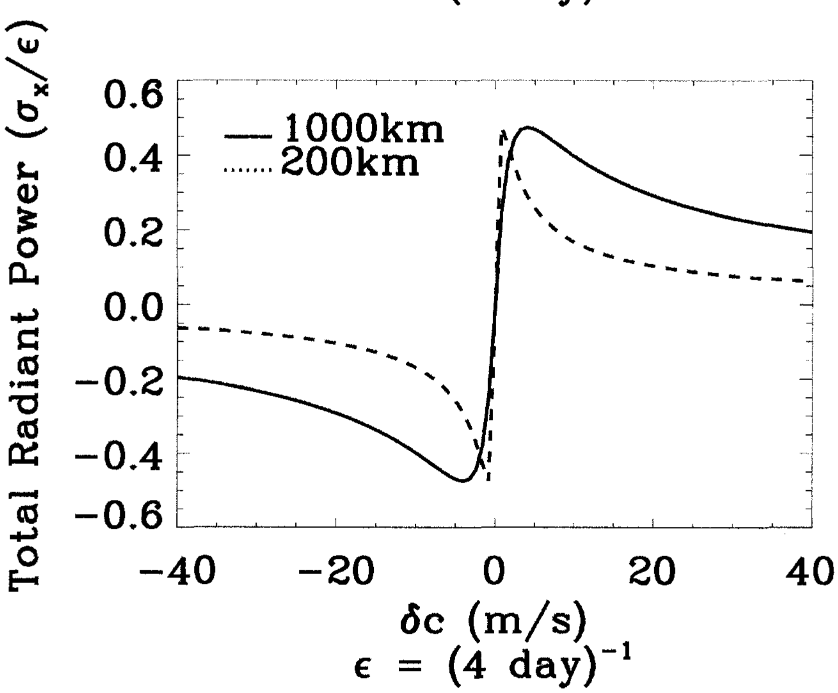

b)

Figure 3.4: Comparison of non-dimensional power response of two Kelvin Waves of horizontal scale σ_x= 200 km and σ_x = 1000 km. (a) Total real power and (b) Total radiant power.

in Fig. 3.3 showing a divergence due to the deep mode that occurs both outside the location of forcing and is everywhere small. For the stratiform mode, $c \approx 23$ ms^{-1} and $\delta c \approx -8$ ms^{-1}. In this case, this value of δc corresponds to the condition where the radiant power is approximately equal to the real power and close to its maximum.

We conjecture that this is an optimal condition for the system because it represents the circumstance for which the power generated by the forcing is removed at the same rate from the forcing region while being kept as local as possible to sustain nearby convergence but not so close to have the negative affects for the $\delta c \rightarrow 0$ case. Figure 3.5 depicts the steady amplitude response solutions for δc = -[0, 4, 8, 12, 16] ms^{-1} for the stratiform mode response (c = 23 ms^{-1}). The location of maximum amplitude for each solution corresponds to the location of $u(a)$ in (3.6) such that the adjustment occurs to the east of this position. For $\delta c \approx -8$ ms^{-1}, the region of adjustment is largely moved away from the region of forcing. For values of $|\delta c| > 8$ ms^{-1} the amplitude decreases without any significant increased forward movement away from the forcing. Thus, $\delta c \approx -8$ ms^{-1} appears optimal in maximizing the low-level lift in a region as local as possible to the stratiform convective system but not within it. This solution is consistent with the observations of new convection developing into the clear air leading the stratiform forcing while also maintaining a positive feedback to the stratiform forcing thus maintaining the source of the wave response.

By equating the two powers in (3.11), we find that :

$$|\delta c| = \sigma_x \epsilon I_{\text{real}} / I_{\text{radiant}} \tag{3.12}$$

where I_{real} and I_{radiant} are the respective definite integral terms in (3.11a and b) which we note are principal functions of σ_x, ϵ and δc. Figure 3.6 derives from the condition that the complete spectrum of powers expressed by (3.11) as a function of σ_x, ϵ and δc are equal. The most striking feature of this figure is the linearity of δc with respect to σ_x, implying

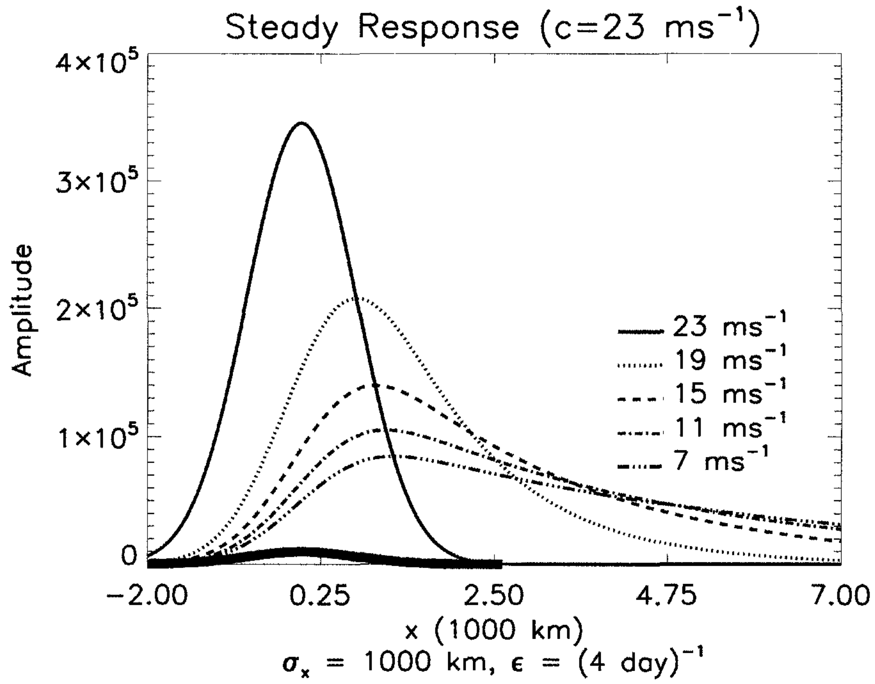

a)

Figure 3.5: Steady Kelvin wave surface level response for an intrinsic phase speed of $c = 23$ ms^{-1}, like that of the second internal trapped heating mode (stratiform response) for 5 different forcing propagation speeds ($c_f = 23, 20, 17, 14, 11$ ms^{-1}). In contrast to Fig. 3.2, only a portion of the 40,000 km domain is shown.

that the ratio of the integral terms in (3.12) is a constant and largely independent of the forcing parameters. It can also be trivially shown that δc varies linearly with ϵ.

3.4b. A Dimensional Approach to the Optimal Propagation Speed

It was noted in section (3.1b) that the time for the negative portion of the Kelvin wave transient response to move one e-fold out of the forcing region was $t_e \approx \sigma_x/\delta c$, provided $\delta c < 0$. Since the forcing is assumed Gaussian, the number of e-folds moved in the x direction also relates to the amplitude of the forcing and a three e-fold movement would effectively mean the response has moved out of the forcing region. The timescale of the wave response is also $t_s \propto \epsilon^{-1}$ before it reaches steady state and remains stationary (phase-locked) with respect to the forcing. Thus, by matching the steady state timescale

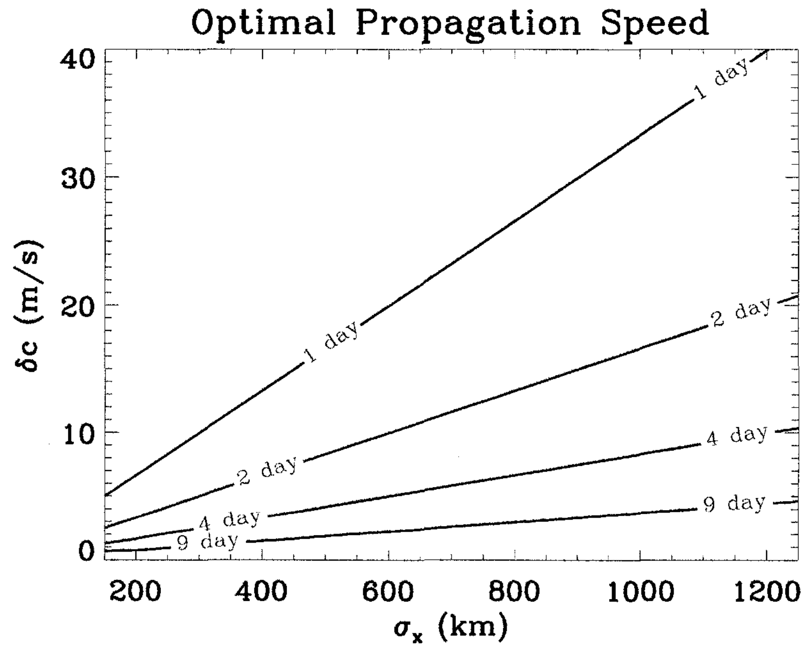

a)

Figure 3.6: Optimal Kelvin wave propagation speed for four different values of ϵ^{-1} (see text for details).

t_s to t_e yields:

$$\delta c \propto -\epsilon\sigma_x \tag{3.13}$$

where δc represents the minimum forcing-wave propagation speed difference for the negative response to propagate at least one e-fold away from the forcing region in the time t_s. This applies to any equivalent depth and the actual value one might calculate for δc depends on the desired number of e-folds used to establish both the timescale t_s and horizontal e-fold movement t_e. Equation (3.13) suggests that the speed difference between the forcing and Kelvin wave scales by the size of the forcing in the x direction and by the damping of the wave. This simple relationship suggests that if the response is strongly damped, then the forcing must travel at very different speed to that of the wave to avoid the wave response becoming highly localized with the negative consequences this implies to the forcing. On the other hand, as the forcing scale (σ_x) becomes large, the speed difference must also increase to allow the energy generated on one side of the forcing to propagate rapidly enough over the region of forcing into the unforced region before reaching steady state.

Since both the power analysis and physical scaling arguments lead to the same relationship for the optimal propagation speed, we propose that computations of the real and radiant power for all wave types as a function of forcing size, meridional position and damping forms a general method for estimating the optimal propagation speed of the convectively coupled system.

3.4c. Application to a Kelvin Wave

Without knowledge of the actual damping in the real atmosphere or what represents an adequate number of e-folds required to define sufficient separation of the response from the forcing, (3.13) implies that if the stratiform mode controls the optimal propagation speed of the forcing and for a convectively-coupled Kelvin wave, $\delta c \approx 8$ ms^{-1}, then a disturbance that grows twice as large in scale implies an optimal forcing propagation speed of $c_f \sim 7$ ms^{-1}, which is consistent with the observed propagation of the Madden Julian Oscillation (MJO Madden and Julian 1971; Wheeler et al. 2000). However, even for $c_f \sim 15$ ms^{-1}, assuming a meridional equatorially centered Gaussian disturbance of scale $\sigma_y = 500$ km, the Kelvin wave only accounts for 47% and 46% of the total energy (power) for the $c = 45$ ms^{-1} and $c = 23$ ms^{-1} modes, respectively. Hence, a complete power analysis of all waves is required using the method just proposed.

In this discussion we did not actually define values for the parameters in (3.13) but note that it may serve as a diagnostic tool. For example, (3.13) predicts a damping rate of (1.5 days)$^{-1}$ for convectively-coupled Kelvin waves of horizontal scale ($\sigma_x = 1000$ km). However, (3.13) assumes one e-fold distance is adequate to remove the response from the forcing where it may be argued that two or three e-folds would be optimal, this producing damping rates of (3 days)$^{-1}$ and (4.5 days)$^{-1}$, respectively, all of which are consistent with Wu et al. (2000a). We also note that the processes that establish σ_x and ϵ remain unresolved in this study.

For small scale disturbances (e.g. squall-lines), one would expect excitation of inertia-gravity waves to predominate (Silva Dias et al. 1983, and chapter 2) but at those scales, they are nearly non-dispersive (see discussion in section 2.5a-iii). In this limit, the non-dispersive Kelvin wave relation (3.13) applies except that the response is now radially symmetrical, demanding that the optimal forcing propagation speed be stationary. In the case of a sheared environment or when the scale of the gravity experiences rotational effects, gravity waves then predicate towards particular directions (Gill 1982a) and in this case, (3.13) holds in the direction of wave propagation. However, other processes also play an important role in squall-line propagation (e.g. vertical shear, cold pools, etc, Rotunno et al. 1988) and we would only conjecture that (3.13) serves as the upper limit before the negative response of the forced gravity waves might interfere with the squall-line. In this light, meso-scale convective systems can ideally travel faster since their scale is much smaller, noting that this is generally observed in the multi-scale view of convectively-coupled systems (Nakazawa 1988; Straub and Kiladis 2002, and others).

3.5. Summary

The main findings of this chapter are:

(i) The solutions predict that a single wave produces two wave fronts that propagate at different phase speeds, one with a speed equal to the forced response and the other with a speed equal to the free response, explaining the observed energy spectra apparent in Two-Dimensional Fourier Transform (2DFT) analysis of OLR and other meteorologic variables (Wheeler and Kiladis 1999; Wheeler et al. 2000). We also note that a simple comparison of the apparent β-plane frequency to that of a 2DFT of the physical solution is ambiguous.

(ii) Assuming a deep mode vertical structure then conditions of low level convergence is required to sustain the (convective) forcing, and conversely divergence acts to destroy this forcing, then we show that the condition that $\delta c < 0$ provides a system of positive feedback between the wave and the forcing. We also show that $\delta c = 0$ results in a wave that is trapped to the forcing whereby half the domain comes under the influence of divergence which we suggests acts to shrink the forcing eventually eliminating it and the wave completely. The behavior of the damped solutions is similar to the undamped solutions except that the the divergence field, confined to the wave fronts of the undamped solution, extend out over the entire region of influence. The physical scale of this influence in the zonal direction was shown to be

$$R_{ix} \propto \delta c/\epsilon$$

which reduces to the scale expected for a stationary forcing ($\delta c \to c$) (Gill 1980). Furthermore, these arguments are general to any vertical structure.

(iii) Consideration of the critical assumptions demonstrated that a mutually supporting convectively coupled system can only exist for the conditions;

$$-\infty < \delta c < 0$$

and that a convectively coupled system cannot exist at the bounds $\delta c \to -\infty$ and $\delta c \to 0$. It was conjectured that an optimal value of δc exists between these bounds and we deduce the relationship for this optimal value as

$$\delta c \propto -\epsilon\sigma_x$$

defined in terms of the scale of the forcing (σ_x) and rate of damping (ϵ). This relation was derived assuming that an optimal configuration of the convectively coupled wave is one in which the rate at which wave energy propagates out of the forcing region (the derived radiant power) matches that rate at which energy is created by the forcing (derived true power). A more mechanistic explanation of the propagation of a convectively coupled wave that leads to the same relationship is also presented based on the first two internal baroclinic modes in the context of Bjerknes (1938) "uniform adjustment" and Mapes (1993) gregarious convection hypotheses applied to the large scale flow. We show how this relationship correctly estimates the phase speeds of convectively-coupled Kelvin waves and, possibly, the MJO as depicted by Wheeler et al. (2000) using observed scales of convective forcing for typical values of σ_x. As a diagnostic equation, the relation also predicts damping rates consistent with the study of Wu et al. (2000a). Furthermore, the relation adheres to the multi-scale view of convectively-coupled systems with increasing propagation speeds at smaller scales (Nakazawa 1988; Straub and Kiladis 2002).

Chapter 4

'Cumulus Clouds' in a Radiative Convective Equilibrium Cloud Resolving Model

Shallow convection is a ubiquitous feature of the tropical boundary layer. Shallow cumulus clouds occur over most of the tropical oceans away from atmospheric convergence zones (Betts and Ridgway 1989) and the significance of this convection on the tropical climate is a topic of much interest. A number of earlier studies point to the importance of shallow convection in maintaining the trades and its circulation (Riehl and Malkus 1958; Nitta and Esbensen 1974; Augstein et al. 1973) and in serving as a source of moisture for the boundary layer that eventually feeds the convergence zones and deep convection (Betts 1973). Thermodynamic budget studies of Yanai et al. (1973) also point to the coexistence of copious amounts of shallow convection in regions of deep convection although the connection between these two modes of convection is not well understood.

More recent studies suggest that the heights of tropical convective clouds are distributed in a characteristically trimodal fashion (Johnson et al. 1999) - one mode of shallow convection with tops reaching to about 2 kms, a deep convective mode with tops reaching to the tropopause and a third mode of congestus with tops to about 6km or slightly above. Stephens and Wood (2005) document the influence of cumulus congestus on the observed surface radiation and precipitation at the ARM Manuus site and further show the predominance of these clouds forming as part of multiple layered systems with this congestus-type convection commonly occurring under thick layers of cirrus. The importance of congestus-type convection to the tropical atmosphere has recently been raised in a number of studies. Johnson and Lin (1997) and Johnson et al. (1999), for instance, present evidence of the importance of cumulus congestus clouds in moistening the middle troposphere prior to deep convection. Inness et al. (2001) demonstrate that a GCM with high vertical resolution produces this congestus-like mode and a more realistic MJO-like variability whereas a course resolution version of the same GCM neither contains a congestus mode nor a mode of intra-seasonal variability like that observed in the real atmosphere. In the GCM experiments that use a cloud resolving model (CRM) for the convection scheme, Ziemianski et al. (2005) report significantly more cloud water distributed in a congestus-like manner than is produced by the version of the same GCM that employs a more conventional type of convection parametrization and speculate on the importance of this convection to the improved modeled climate of the tropics.

There remains, however, much we do not understand about the roles of the two shallower modes of convection on the tropical climate and how or whether shallow convection influences the deeper tropical hot-towers. This chapter describes a series of cloud resolving model (CRM) radiative convective equilibrium (RCE) experiments that begins to examine such connections. The general concept of RCE considered here have proven to be a useful paradigm for studying broader aspects of the Earth's global climate system (Stephens 2005) and has much relevance to the study of the tropical atmosphere (e.g. Betts and Ridgway 1989). More recently, a class of RCE studies have emerged that treat convection more explicitly using CRMs (Held et al. 1993; Sui et al. 1994; Tompkins and Craig 1999; Grabowski and Moncrieff 2000; Stephens et al. 2004b, and other). The use of CRMs as a means of modeling the convection explicitly offers a more self–consistent means for connecting radiative processes to hydrological processes than was possible with the earlier, simpler RCE models and, for that matter, is currently possible with the existing parameterizations used in GCM climate models. Many of the earlier CRM-RCE studies, however, are set on model domains that are too small to consider RCE as a realistic governing state of the system. Out of necessity, larger domain RCE experiments set on domains of many 1000's of kms, and more relevant to the concepts of equilibrium of the global tropics, for example, are typically forced to use CRMs set on two dimensions with spatial resolutions $\Delta x \approx$ 2-4 km. While these experiments accommodate the larger-scale aspects of equilibrium, they suffer from uncertainties associated both with this coarse resolution that only marginally resolves convection and with issues surrounding the 2 dimensional representation of convection. To date, sufficient computer resources for equivalent large-scale, three dimensional RCE studies have not been made available except for the 3D channel experiments by Tompkins (2000).

There are many elementary aspects of RCE that remain to be understood, such as what is the role of the different modes of convection on the water and energy balance at equilibrium, how do these balances change with different external forcing and how does convection feedback on its environment to establish the equilibrium state? Given the above mentioned caveats, several CRM-RCE 2D experiments are discussed here that are used to explore the connections between shallow and deep convection, how radiative processes affect the resultant modes of convection and, in turn, the organization of the broader aspects of the hydrological cycle of the model. The results of the experiments are consistent with our understanding of shallow convection as an essential aspect of the water cycle being involved in both moistening the environment and drying the environment through their evolution to deep convection. Despite the noted limitations of the model, many aspects of the resultant equilibrium resemble the real world. For example, the CRM experiments produce thermal structures in the convective environment very similar to those observed, such as low level and mid-tropospheric stable layers. The experiments also produce realistic trimodal cloud-top distributions and exhibit a variability of water vapor as it affects convection in general agreement with the observed variations of water vapor.

The importance of feedbacks between water vapor and the organization of convection is also explored, underscoring the role of these shallow clouds in this feedback. The results reinforce the ideas that feedbacks between water vapor and convection induce a type of 'self-aggregation'; a topic discussed in many contexts, such as on the observed thermodynamics of shallow convection (Esbensen 1978; Nicholls and Lemone 1980), deeper convection associated with the easterly wave (Johnson 1978) and in the context of cloud resolving RCE experiments (e.g. Held et al. 1993; Tompkins 2001b; Bretherton et al. 2005, and others). The present study shows that a coupling between water vapor and radiation provides an important additional mechanism that promotes shallow cumulus clouds through effects of radiative cooling on low-level stability. In the RCE context, these shallow clouds respond to low-level radiative cooling structures and their existence is critical to the low to mid-level moisture build up as shallow convection deepens into congestus which in turn provides a pathway for the development of deep convection. Regions of such moisture build-up are referred to as 'moist domes' owing to their appearance in the vertical structure of water vapor. Moist domes form in a number of locations across the domain and it is there that deep convection develops and water is removed by convective precipitation.

Section 1 describes the cloud resolving model used in the experiments and the various experimental setups reported on in this paper. Section 2 reviews the equilibrium achieved in the four experiments conducted with an SST of 300K and discusses the cloud properties and atmospheric stability at equilibrium. Section 3 describes the effects of deep convection, cumulus convection and clear skies on the equilibrium hydrologic cycle demonstrating that at equilibrium, a water balance exists between the moistening effects of shallow clouds and the drying by precipitating deep convection. Section 4 outlines the mechanism responsible for the development of cumulus convection in the model and explores how this development is related to the profile of radiative cooling. Section 5 describes the factors that control the life cycle of shallow convection and illustrates the pathway connecting shallow convection to deep convection in the model. Section 6 addresses the sensitivity of these findings to grid resolution and SST reinforcing the results described in the earlier sections. Section 7 summarizes the main results of the study.

Model ID	Configuration Summary
IR / IR-300	Fully interactive run over an SST of 300K
PR-lin	Homogenously prescribed mean radiation profile, linearized to remove vertical gradients
PR-mean	Homogenously prescribed mean radiation profile (as is)
IR-nocld	Interactive run with only clear-sky forcing (no cloud forcing)
IR-295	Interactive run over an SST of 295K
IR-305	Interactive run over an SST of 305K
FINE-IR	IR-300 experiment conducted on the fine grid
FINE-PR-lin	PR-lin experiment conducted on the fine grid

Table 4.1: Summary of Model Configurations Integrated

4.1. Model Description and Experimental Setup

The RCE experiments reported in this study are conducted using the System for Atmospheric Modelling (SAM) Cloud-Resolving Model (CRM) developed at Colorado State University (CSU) by Khairoutdinov and Randall (2003). Incorporated into this model is the radiative transfer model developed at CSU and is referred to as BUGSrad (Stephens et al. 2001). The radiation module was called every five minutes producing heating rates at this frequency.

In summary, the CRM uses the anelastic set of dynamic equations with a sub grid scale (SGS) 1.5 order closure scheme based on Deardorff (1980). Microphysical processes are treated using a bulk microphysics scheme that predicts the total water (water vapor, cloud water and cloud ice) and total precipitating condensate (rain, snow and graupel). The phase distribution of hydrometeors in this scheme are diagnosed by the temperature at that grid point and the formation of clouds is parameterized by the 'all-or-nothing' approach. Cloud water is set to have a zero fall velocity but cloud ice is allowed to sediment at a rate proportional to the altitude to prevent unrealistic build up of ice clouds. The formation of precipitation is parameterized using the Kessler (1969) autoconversion method and subsequent drop size follows a Marshall-Palmer distribution. Droplet growth forms exclusively by collision and coalescence and evaporation is parameterized. Surfaces fluxes are parameterized by simple aerodynamic-bulk formulas.

Apart from the grid-resolution sensitivity experiments described later in section 6, all experiments were conducted on a 2D grid of 8192 points, at 2.4 km grid spacing covering roughly 20,000km in the horizontal. Vertical structure is resolved using a stretched grid of 65 points with a boundary layer resolution as fine as 50m near the surface, increasing to 500m by 5km and then constant to the top of the atmosphere at 27 km, which has been shown to adequately resolve vertical water vapor profiles (e.g. Tompkins and Emanuel 2000). The Coriolis parameter was set to zero with a free-slip lower oceanic boundary and time step of 10s, with the capability of this being split in two if a linear instability was detected. A gravity-wave absorber in the upper 1/3 of the domain was active with a Rayleigh damping back to the mean state applied to the x momentum to prevent the build up of vertical shear ($\tau = 7200s$). The lateral boundaries are periodic. All runs were initialized with the 00 GMT 5 December 1992 TOGA COARE [1] sounding with zero mean wind in the vertical. The standard NCAR [2] tropical ozone sounding was used for the interactive radiation experiments to create a radiative tropopause. This is required to balance the eddy heat flux divergence from overshooting deep convection and, thus, maintain a fixed tropopause height over the long integrations. An initial small-amplitude randomized disturbance was introduced into the temperature field to initiate convection and all surface fluxes are interactive, that is they are wind-speed and humidity dependent.

The experiments reported in this paper are summarized in Table 1. The first group

[1]The Coupled Ocean-Atmosphere Response Experiment of the Tropical Ocean and Global Atmosphere Programme sounding

[2]National Center for Atmospheric Research

of experiments employ four different model configurations all with a lower boundary condition defined by a uniform and fixed SST of 300K. These experiments are designed to illustrate the effects of radiation on convection. The four experimental designs are i) The Interactive Radiation experiment (IR-300) which serves as the control run, ii) The Prescribed Radiation - linear experiment (PR-lin) applies a hypothetical radiative heating profile that is a constant -1.12 K/day between 1000 mb to 130 mb and a constant 0.1 K/day from there to the top of the atmosphere, thus removing first-order vertical gradients of radiative heating, except at about 130 mb. For this profile the mass integrated tropospheric cooling is the same as the final 10 day mean IR-300 profile and that heating is applied homogeneously across the model domain, iii) a second prescribed radiation experiment (PR-mean) that applies the mean profile from the last 10 days of the IR-300 experiment, also uniformly across the model domain. iv) An interactive radiation experiment (IR-nocld) that couples only the clear-sky component of radiative heating, thus removing explicit effects of cloud radiative heating.

The next group of three experiments are referred to as the SST sensitivity experiments, including the IR-300 experiment for reference. The three experiments of this group all apply radiation interactively as in the IR-300 experiment. One experiment assumes a fixed SST of 295K (hereafter IR-295) and the second assumes a fixed SST of 305K (IR-305) providing a direct contrast to the results of the IR-300 experiment. The final group of experiments explores the effects of grid resolution on equilibrium. Both the IR-300 and PR-lin experiments were repeated using a 500m horizontal resolution but over a more limited horizontal domain.

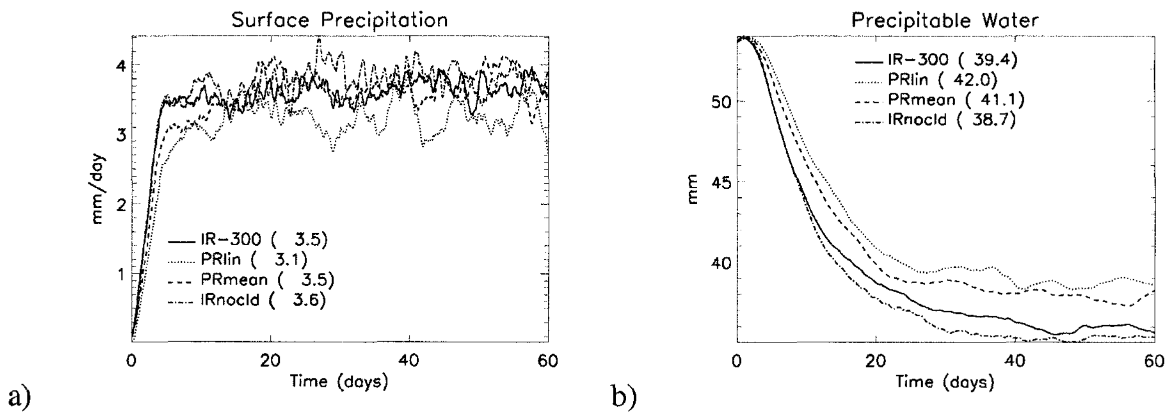

Figure 4.1: Time evolution of domain (a) surface precipitation and (b) precipitable water. Note a 4 day running average is applied and legends contain the total time mean average value.

4.2. Equilibrium Results at 300K

4.2a. Evolution to Equilibrium

Figures 4.1a-b show the evolution of the domain means surface precipitation and precipitable water (PW). These indicate that the model reaches equilibrium after about 50 days with PW and surface precipitation reaching steady values on a shorter convective time scale consistent with Tompkins and Craig (1998).

Although quantities plotted in Fig. 4.1 indicate all experiments reach a steady equilibrium, the way this equilibrium is achieved across the model domains varies from experiment to experiment. A succinct way of presenting the structure of these quantities as the model evolves to equilibrium is in the form of time longitude variations of the type shown in Fig. 4.2. This figure is a Hovmuller-like presentation of the Precipitable Water (hereafter, PW) from the IR-300, PR-lin, PR-mean and IR-nocld experiments and offers a broad view of the wider-scale characteristics of the RCE reached by each experiment and how the water cycle of the model is grossly organized. The results show a marked difference in the temporal evolution of the spatially distributed water vapor between the experiments with fixed radiation (Figs. 4.2a and c) and the experiments with interactive radiation (Figs 4.2b and d). After an initial spin-up of around 10 days,

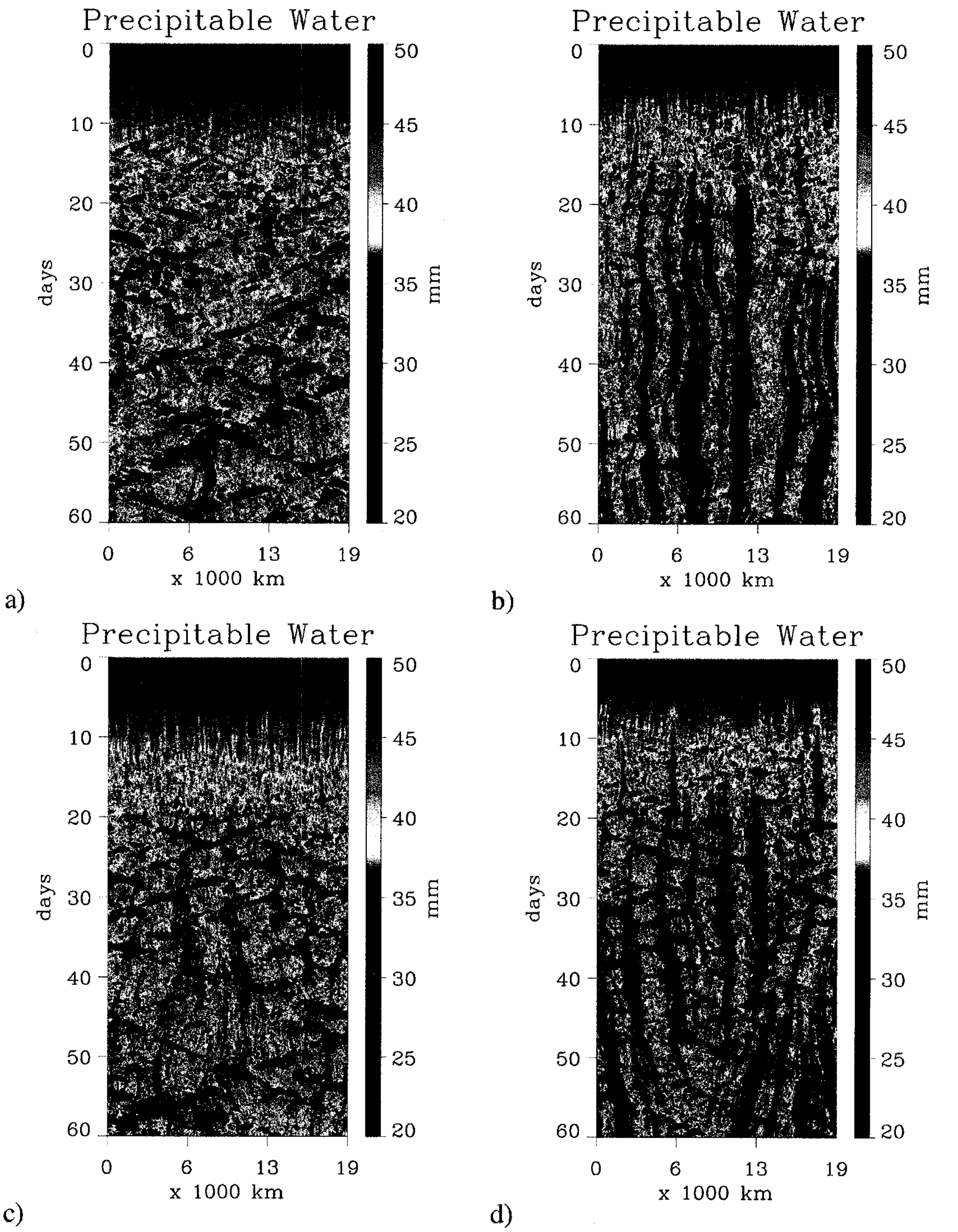

Figure 4.2: Precipitable water plots for the (a) Prescribed Radiation experiment (linear), (b) Interactive Radiation experiment, (c) Prescribed radiation experiment (mean) and (d) Interactive radiation experiment with only clear-sky forcing

water vapor organizes into dry and moist regions that remain more or less coherent over time. In the two fixed radiation experiments, these moist and dry regions propagate in both directions across the model domain whereas the moist/dry regions remain quasi-stationary in the interactive radiation experiments, although hybrid behavior is observed in all experiments. Originally noted in Held et al. (1993), why such stationary features arise with interactive radiation and the factors that define their horizontal scale and organization are issues not addressed in this paper but are topics being pursued in another related study. The stationary moist-dry structures evident in these experiments hints at the notion of self-aggregation of convection which locks into the wettest areas of the domain. When coupled to the dry areas through a broad solenoidal circulation between them (e.g. Fig 4.2), these moist regions appear to be self-sustaining. The pattern of moist-dry is a robust feature of such equilibria being noted in similar experiments conducted with very different CRMs (e.g. Held et al. 1993; Tompkins 2001b; Bretherton et al. 2005, and others).

The general circulation established in the interactive radiation experiments is significantly different from the general circulation of the fixed radiation experiments, due in some way to spatial variations of radiative forcing in the former. These findings suggest that the spatial gradients of the clear-sky cooling rate must be important to whatever mechanism affects the general circulation given the similarity of the IR-300 and IR-nocld experiments. As we shall show in following sections, the vertical structure of the radiative heating also grossly influences the cloud distributions.

4.2b. Profile properties at Equilibrium

Figure 4.3a compares the domain-averaged net radiative heating rate profiles for the four 300K SST experiments (IR-300, PR-lin, PR-mean and IR-nocld) averaged over days 50-60 of the experiments. Figure 4.3b is the latent heating rate profiles and Figs. 4.3c and d respectively present radiative and latent heating profiles for the three SST

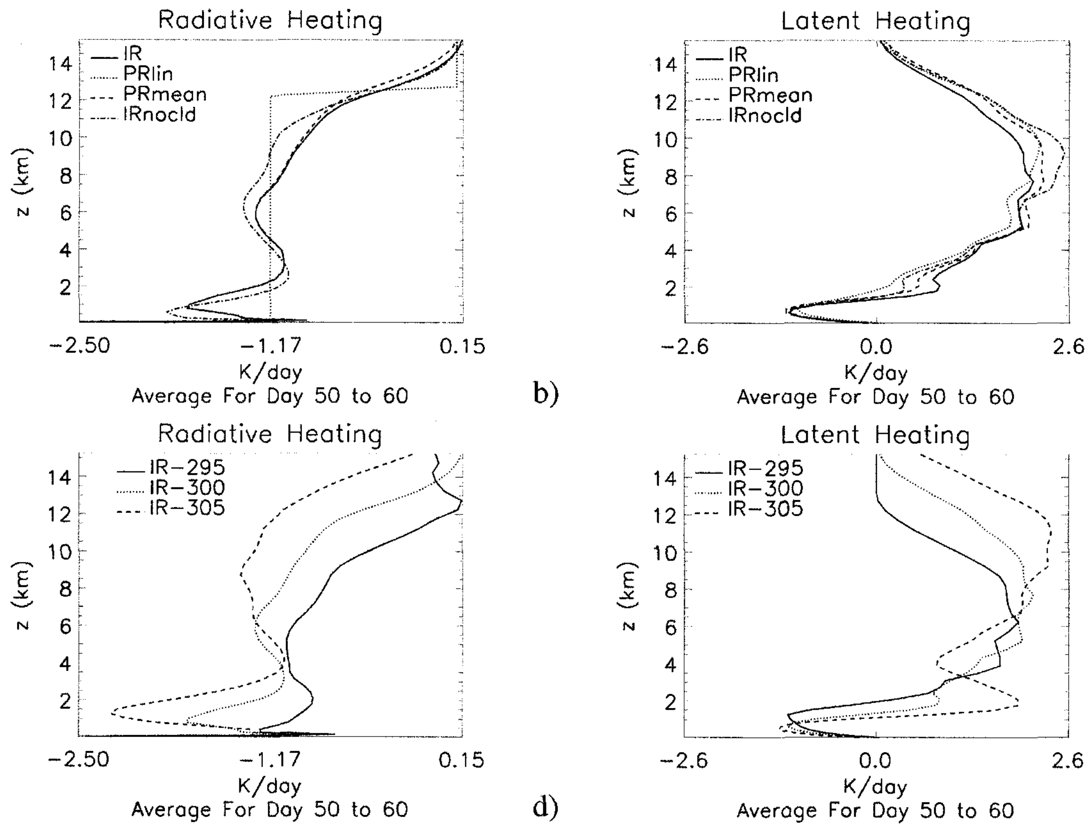

a) b) c) d)

Figure 4.3: Final 10 day mean net (a) radiative heating rates and (b) latent heating rates for the four radiation sensitivity experiments. Note that PR-mean radiative heating profile overlies the IR profile nearly completely but the same is not true for the latent heating term. Figure (c) and (d) are the same but for the three SST sensitivity experiments.

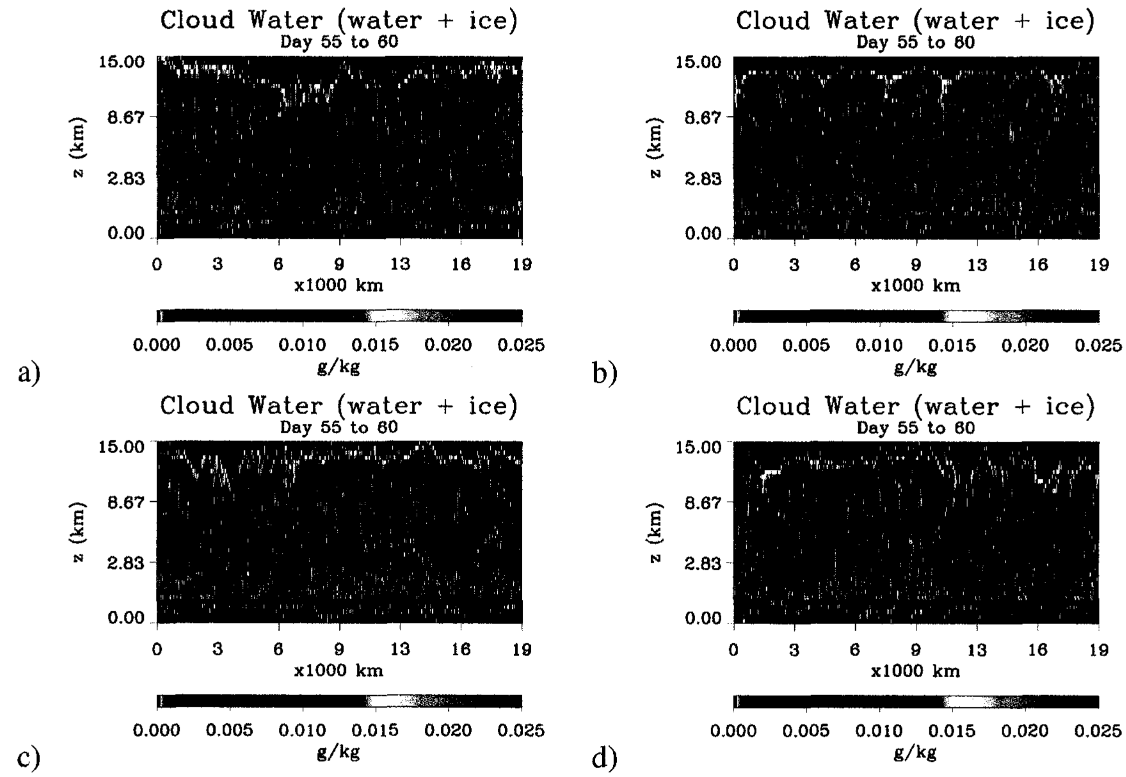

Figure 4.4: Final 5 day mean cloud water fields for the (a) PR-lin, (b) IR, (c) PR-mean and (d) IR-nocld experiments

sensitivity experiments (IR-295, IR-300 and IR-305). A remarkable feature of the radiative cooling profiles (Figs. 4.3a and c) is the low-level cooling maximum that appears in all experiments except for the PR-lin experiment which, by design, has a profile that has no maximum in these lower levels. The low-level cooling maximum also increases in magnitude and raises in height as the SST increases. The cooling maximum and its variation with SST is a consequence of the enhanced absorption that occurs in the atmospheric window region of the IR absorption spectrum through a mechanism known to be proportional to water vapor partial pressure (Burroughs, 1968; Cox, 1973; and Stephens, 1976). As shown later, these low-level cooling maxima are central to the enhanced development of shallow cumulus convection. Further discussion of the effects of sea surface temperature on the convective equilibrium is given later in section 7 and future papers.

Figure 4.4 contrasts the two dimensional vertical cross sections of the cloud water

a) b) c)

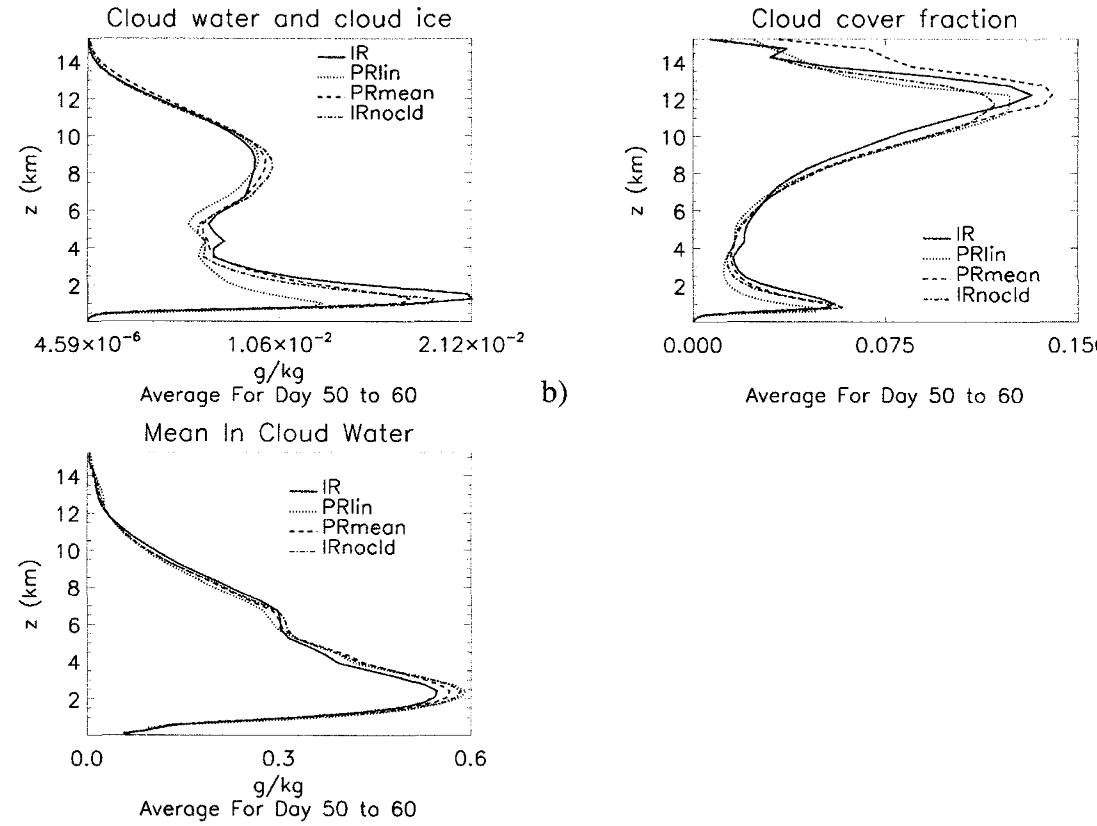

Figure 4.5: Comparison of the final 10 day (a) domain mean cloud water and ice, (b) domain fractional cloud cover, (c) total cloud mass and (d) mean liquid in cloud

for all four 300K SST experiments derived from averages over the final 5 days of the experiments (days 55-60). The cloud fields that evolve in all experiments broadly consist of cumulus and cumulus congestus clouds approaching the 6km level, with intermittent deep convection. The characteristics of the clouds produced in the experiments agree generally with the trimodal distributions reported by Johnson et al. (1999). Notable, however, is the lack of low level cloud water in the PR-lin experiment (Fig. 4.4a) compared to the other experiments. The two prescribed radiation experiments (PR-lin and PR-mean, Figs. 4.4a, c) also exhibit a more homogenous occurrence of low–level cloud across the domain whereas the two interactive radiation experiments display relatively more synoptic scale variability of low–level cloud water contents on a scale O(1000km). These localized regions of low cloud water content coincide with the regions of high PW (Fig. 4.2) and deep convection.

Figure 4.5a compares the domain averaged profiles of cloud liquid water and ice contents for the four 300K SST experiments under discussion. As expected from the comparisons of Fig. 4.4, the cloud water contents below 6km of the PR-lin experiment are a factor of two smaller than the cloud water contents of the other experiments and we will show later that this is related to the differences in the low level radiative cooling between the experiments. Figure 4.5b compares the corresponding vertical distributions of the domain averaged cloud cover showing similar amounts of upper level ice content and cloudiness in all experiments but much reduced low cloud amounts in the PR-lin experiment between 1-4 km suggesting that the reduction in low level water is a consequence of reduced cloud amount. Fig 4.5c compares the in-cloud water contents, which are generally similar in the 4 experiments although the water contents of the cumulus clouds of the interactive radiation experiments are slightly reduced, perhaps a consequence of the greater precipitation that falls from the cumulus clouds of these experiments (discussed further in the next section).

4.2c. Stability

Figure 4.6 presents vertical cross-sections of the stability ($\frac{\partial\theta}{\partial z}$) for all four experiments averaged over the final 5 days of each experiment. Humidity contours between 50% to 80% are also superimposed for reference. In the IR-300 and IR-nocld experiments, the synoptic scale organization of enhanced low–level cloud water coincides with low static stability (1-3km) and increased humidity, the latter exceeding 50% above 5km in some regions. The PR-mean (4.4-c and 4.6-c) behaves slightly differently with most of the low level cloud water (4.4-c) appearing in the left half of the domain where the highest stability exists and unconnected to elevated regions of low-level humidity. The cause of this behavior is the development of a domain wavenumber–1 circulation at the beginning of this temporal averaging period in the PR-mean experiment (Fig. 4.2c). Note that deep moisture regions appear in the right half of the domain and that these regions are

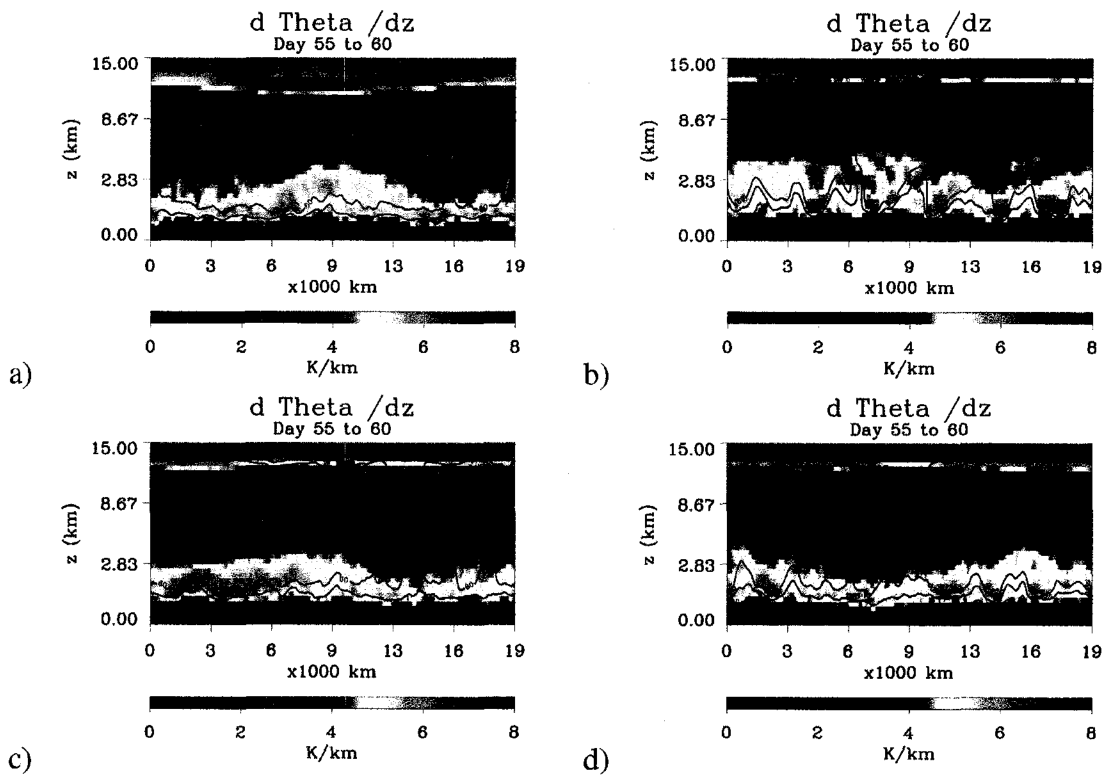

Figure 4.6: Final 5 day mean stability profile ($\frac{\partial\theta}{\partial z}$) for the (a) PR-lin, (b) IR, (c) PR-mean and (d) IR-nocld experiments. Note that the relative humidity is contoured for values between 50% and 80%.

associated with reduced static stability, congestus and deeper cumulus convection, as in the IR experiments. In this manner, for the PR-mean and PR-lin experiments, the 'moist domes' and their associated reduced mean static stability propagate.

Stable layers form around the freezing level within and near regions of deep convection in all experiments (shown more clearly in Figs. 4.7 and 4.12 below) in a manner that resembles the observations reported in J95 and probably due to one of the processes proposed in J95. Stronger stable layers develop in the interactive radiation experiments suggesting that the radiative cooling associated with these stable layers further sustains them much as speculated by Mapes and Zuidema (1996). J95 also observe low–level stable layers in deep convecting regions similar to those observed in the trade cumulus regions but not associated with any obvious vertical moisture gradients. We will show that such stable layers also occur in these simulations. Although the precise origin of these low-level layers is not conclusively determined, they most likely arise from the effects of convectively induced wave dynamics on the environment.

In summary, shallow cumulus clouds tend to occur in regions of enhanced water vapor that are surrounded by drier regions making these moist region appear as synoptic scale 'moisture domes' whose propagation characteristics are influenced by spatial variations of radiation not investigated here. Held et al. (1993) refer to these regions as 'wet-spots' as they also correspond to regions of highest surface precipitation. These moist domes also possess lower static stability than surrounding subsidence regions in the temporal mean but, as discussed in section 6, life cycle analysis shows the static stability varies and evolves with episodes of increased vertical cumulus cloud development coinciding with decreased stability prior to the formation of deep convection.

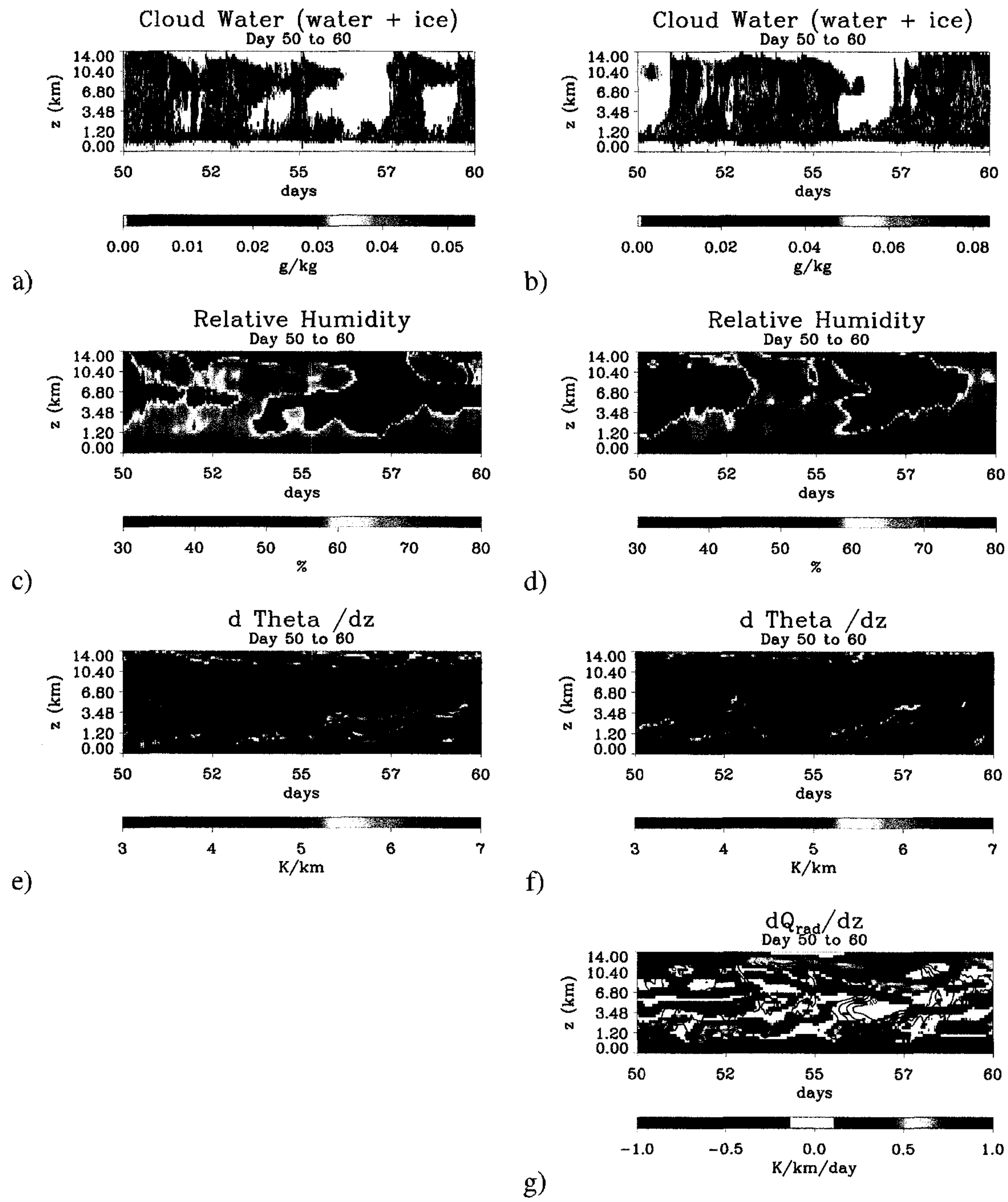

Figure 4.7: 10 day time series of 400km horizontally averaged total cloud liquid (water and ice), relative humidity and stability parameter ($\frac{\partial \theta}{\partial z}$) for the PR-lin (column 1) and IR (column 2) experiments. The position of the averaging window is largely irrelevant for the PR-lin experiment since the convection is spatially homogenous while for the IR experiment it is chosen to lie in the center of a 'moist dome'. Note that the relative humidity is contoured for values between 50% and 80% in the stability plots.

4.3. The water cycle at Equilibrium

More detailed analysis of the water cycle properties at equilibria given below shows how the shallow cumulus clouds and the clear sky regions of the model supply the moisture to the wet areas and how the deep convection that forms in these moist dome regions remove it, establishing the overall water balance at equilibrium. The nature of this balance is demonstrated with a simple procedure that employs the simulated OLR as a way of organizing the water budget into clear-sky, shallow convection and deep convection regimes. Three OLR thresholds were found to best categorize such regions; (i) a low OLR regime that characterizes deep convection as typified by heavy precipitation and the presence of thick ice clouds, (ii) an intermediate OLR regime that characterizes cumulus convection that primarily consists of (precipitating) water clouds free of ice and (iii) a high OLR regime that identifies clear skies devoid of most cloud and precipitation. Regions defined in this way do not perfectly isolate the effects of deep convection from shallow convection and clear sky regions. Regions of deep convection and thick anvil cloud in the moist domes, for instance, also contain shallow convection below and the regions of shallow convection are furthermore juxtaposed with clear regions such that the evaporation from these neighboring clear regions is strongly influenced by the local scale turbulence associated with the shallow convection.

The OLR thresholds used to define these regimes were chosen according to the analysis contained in Figs. 4.8 and 4.9. These figures are histograms of selected hydrologic variables (cloud water path (CWP), ice water path (IWP), PW, latent heat flux (LHF) and surface precipitation) taken from the final 10 days of the four 300K SST experiments and grouped into 2Wm^{-2} OLR bins. The left set of panels are the mean values of the given quantity in each OLR bin presented as a function of OLR and right-hand panels present the integrated contribution of that bin to the total variable in such a manner that the integral under each curve is normalized to unity. The domain mean value of a particular parameter is given in the legend for reference. Practically all ice and

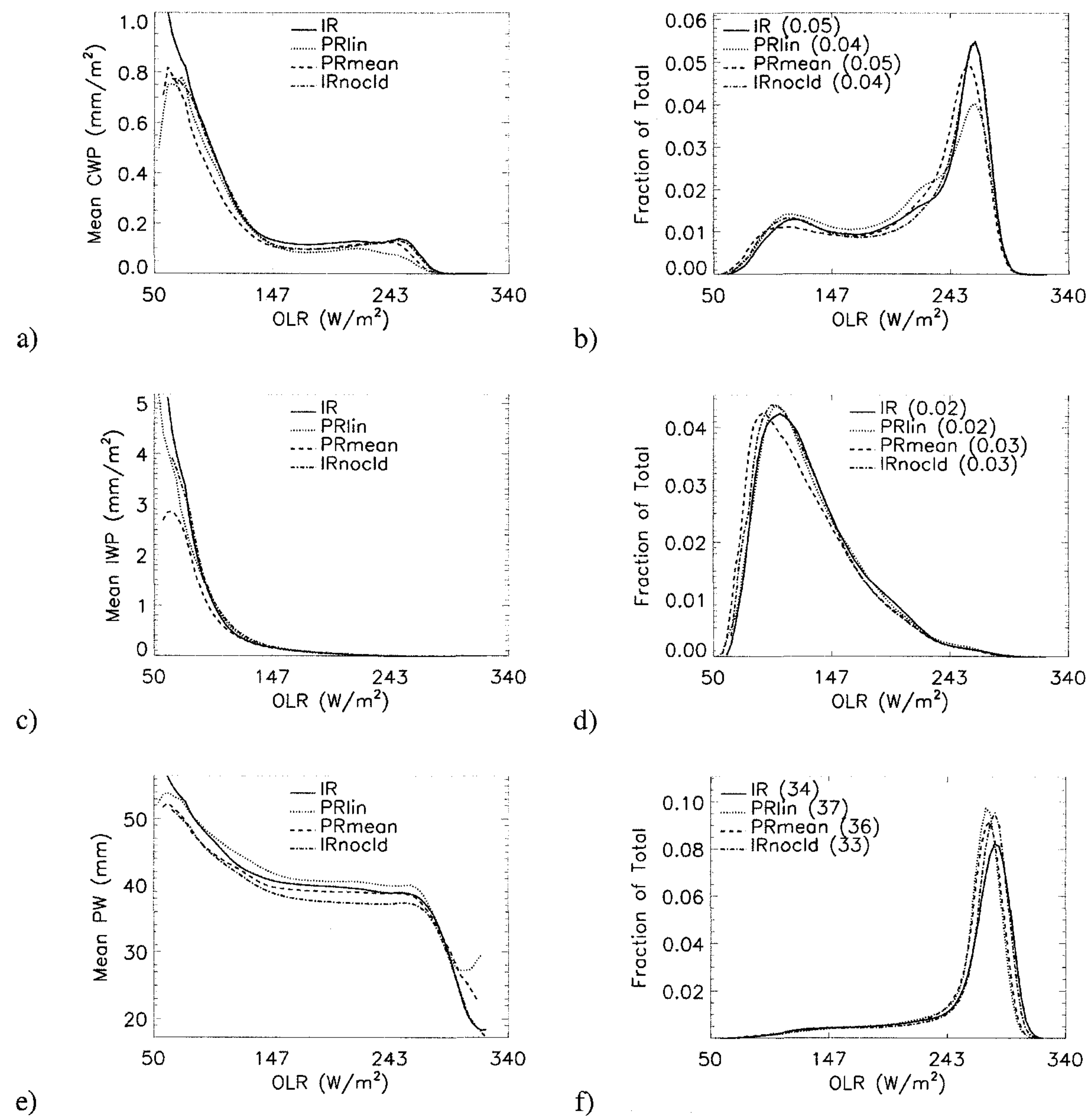

Figure 4.8: Day 50 to 60 histograms (2 W/m^2 bins) of hydrologic variables used to identify the OLR windows for designating the three cloud regimes of interest, Deep convection, cumulus convection and clear-sky subsidence regions. The left column depicts the mean variable value for a particular OLR bin while the right column depicts the integrated contribution of that bin to the 10 day mean. Note that the legend for the right column contains the domain mean value for reference. Row 1 (a and b) - cloud water path, with mean values in mm/m^2. Row 2 (c and d) - ice water path, with mean values in mm/m^2. Row 3 (e and f) - precipitable water, with mean values in mm.

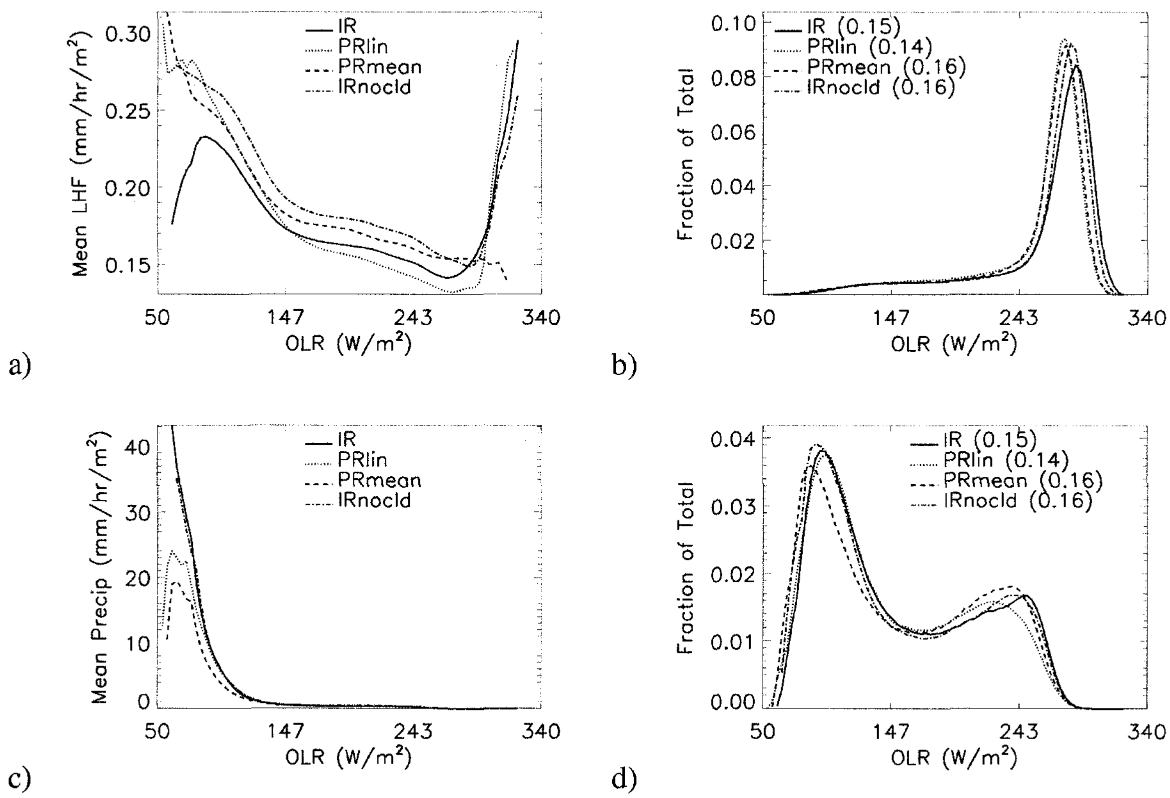

Figure 4.9: Same as figure 4.8 except for moisture budget variables. Row 1 (a and b) - latent heat flux in $mm/hr/m^2$. Row 2 (c and d) - surface precipitation in $mm/hr/m^2$.

much of the precipitation occurs in those model columns for which the OLR is below $235 \mathrm{Wm}^{-2}$. Consequently, this value was used to define the deep convective threshold. The cumulus cloud regime occurs for OLR values between 235 Wm^{-2} and 273 Wm^{-2} and the clear sky regime corresponds to OLR values above $273 \mathrm{Wm}^{-2}$.

The percentage contributions of the three cloud regimes to the total cloud water path (CWP), ice water path (IWP), latent heat flux (LHF) and precipitation are summarized in Table 4.2 for all four experiments. This summary indicates that the clear sky and cumulus cloud regimes contribute about 80% of all the moisture in the four experiments by evaporation and only loose 10-14% of this moisture by precipitation. Conversely, evaporation in designated regions of deep convection contributes only about 20% to the total water content while these regions account for 86-90 % of the moisture lost by precipitation. This behavior is also reflected in Fig. 4.9 to some extent showing a monomodal distribution for latent heat flux strongly peaked above OLR values of 235 Wm^{-2}. The precipitation exhibits a bimodal distribution with respect to OLR.

Further insight into the nature of the hydrologic cycle at equilibrium follows from consideration of the domain wide precipitable water (PW) budget written in the form

$$\frac{d}{dt}PW = \text{Latent Heat Flux} - \text{Surface Precipitation Flux} \tag{4.1}$$

where advection is zero in the domain integral. The latent heat fluxes and surface precipitation fluxes are differenced and grouped by the OLR regimes and then binned with respect to precipitable water. This analysis is shown in Fig. 4.10 and illustrates how the domain moisture flux for the three regimes varies according to precipitable water and its important to note that PW is a proxy for location indicating collocated cloud regimes. Figure 4.10a emphasizes the dominant contribution of the clear sky regions to the moisture budget, especially for PW $>$ 30mm. These regions coexist with cumulus clouds (Fig. 4.10b) that enhance the evaporation in these neighboring clear skies regions

Cloud Regime	Sampling Frequency	CWP	IWP	LHF	Precipitation
Deep Convection ($< 235\ W/m^2$)					
IR	15	51	98	18	86
PR-lin	17	59	98	21	90
PR-mean	17	52	98	20	88
IR-nocld	15	50	98	18	87
Cumulus Convection (235 - 273 W/m^2)					
IR	20	42	2	20	14
PR-lin	29	34	2	32	10
PR-mean	28	42	2	31	12
IR-nocld	25	43	2	21	13
Clear-Sky ($> 273\ W/m^2$)					
IR	65	7	0	62	0
PR-lin	54	7	0	48	0
PR-mean	55	6	0	49	0
IR-nocld	65	7	0	60	0

Table 4.2: Table of cloud regime type and their contribution to the domain total Cloud water Path (CWP), Ice Water Path (IWP), Latent Heat Flux (LHF) and surface precipitation. This analysis is performed for the two most distinct model runs, the IR and PR-lin runs. The bracketed number next to each experiment indicates the frequency of that cloud regime in that experiment.

by the deeper mixing by cumulus clouds. It is noteworthy that PW $\approx$ 40mm appears to be the cross over point above which both clear skies and cumulus clouds no longer act as a net source of moisture and the precipitation from shallow cumulus clouds now exceeds any moistening effects by evaporation. As such the cumulus clouds become more precipitation efficient preventing any further moisture build up and act as a regulator of the system. In the wet regions (PW $>$ 40 mm), deep convection coexists with cumulus clouds with the intense precipitation from deep convection rapidly drying the region.

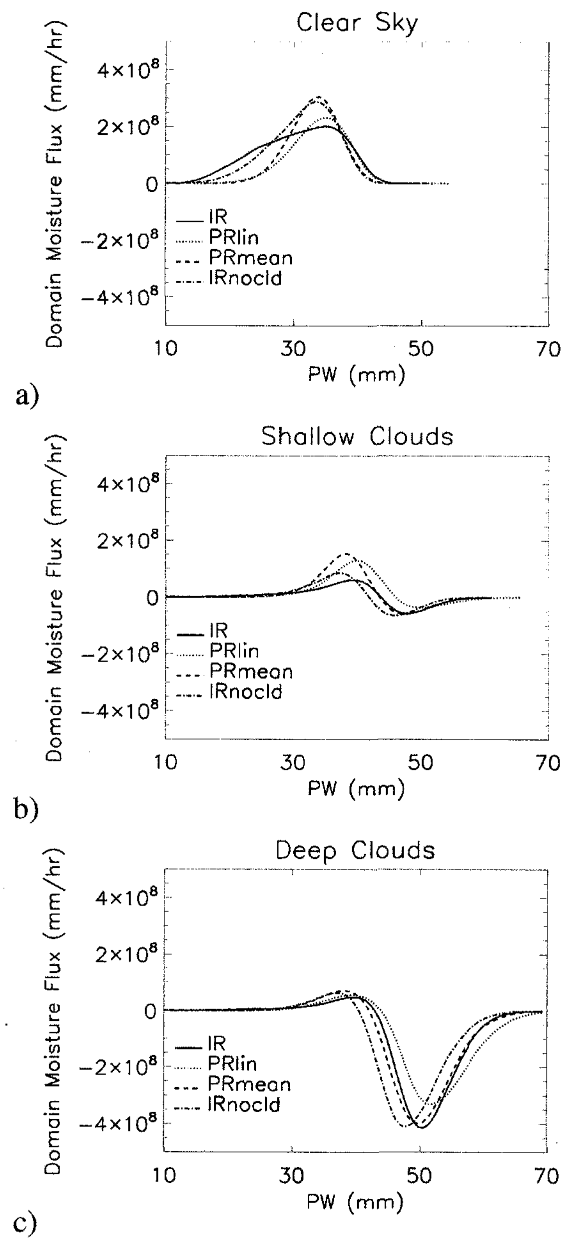

Figure 4.10: Domain net moisture flux as a function of precipitable water and cloud regime. (a) Clear-Sky, (b) cumulus convection and (c) deep convection.

4.4. Radiative Heating and Cumulus Clouds

The previous section highlighted the important role of shallow convection and its surrounding environment as the principle moisture source of the model, through surface evaporation, while also acting to regulate this moisture build-up in very moist zones. The moisture is then available for use by deep convection which can rapidly dry a region. In this way it was shown how the relation between shallow and deep convection is central to understanding the way the water budget of the RCE experiments is established. In this section and the section to follow, we examine this connection further focusing in on the moist-dome regions of the model. Here a mechanism that explains the differing amounts of cumulus clouds that develop in the different experiments is introduced.

4.4a. Divergence of a moist plume

The experiments discussed so far highlight the differences in the amounts of cumulus clouds in those experiments and suggest these differences occur as a result of differences in low-level radiative cooling (e.g. Fig. 4.3a and c). A mechanism is now forwarded to explain this connection through the stabilizing effects of radiative cooling in the lower moist layer. The mechanism proposed is simple. The mean water vapor path causes a radiative cooling profile that promotes a stable layer across the domain that restrict the penetration of convective moist plumes from below. On reaching these stable layers, moist plumes detrain, moistening the stable layer, and eventually shifting the cooling slightly higher and reducing the stabilizing affect of radiation in that layer. The plume itself adjusts the local region to a moist-adiabat that effectively destabilizes that layer and provides a neutral pathway for further convection to penetrate into the now elevated stable layer, the process repeating until a moist dome is created, the size, moisture and longevity of which being controlled by other factors.

The effects of a cloud on it environmental stability is described in Bretherton and

Smolarkiewicz (1989) as a gravity wave adjustment of the surrounding cloud free environment (CFE) towards the in–cloud buoyancy. They show that a moist plume will preferentially detrain in an environment that is more stable than some reference moist adiabat;

$$\frac{\partial \theta_p}{\partial z} < \frac{\partial \theta}{\partial z} \tag{4.2}$$

where θ_p is the parcel potential temperature and θ is the potential temperature of the environment.

This simple idea provides a useful framework in studying Fig. 4.11. The domain mean vertical profile of stability for all four radiation experiments is contrasted in Fig. 4.11a against a pseudo-moist adiabat (heavy solid line) corresponding to a saturated surface parcel, $\theta_{es} = 345$K. Also shown for reference is the $\theta_{es} = 340$K pseudo-moist adiabat which corresponds to a surface parcel at 50% saturation (heavy dashed line). The temperature profile derived from all experiments exhibits the general structure that is discussed in Mapes (2001). The lapse rates of the middle troposphere between 6 and 8km closely follow a moist-adiabat with departures from the moist adiabat above and below this region. In the context of (4.2), the results of Fig. 4.11a imply that a convective plume detrains above 8km and either entrains or detrains below about 6 km depending on the reference moist adiabat. Unsaturated entraining parcels would rise along a moist adiabat notionally like the $\theta_{es} = 340$K pseudo-moist adiabat shown and thus would be expected to detrain at all levels. Those experiments with more prolific cumulus cloudiness also possess slightly higher mean stability in the 1-6km layer (Figs 4.11a and b), thereby enhancing the potential for such detrainment effects in this layer.

4.4b. *Stability Analysis*

The simple stability arguments above rely on a comparison between the local stability ($\frac{\partial \theta}{\partial z}$) and a moist adiabat. Such comparisons as shown in Fig. 4.11 suggest that any en-

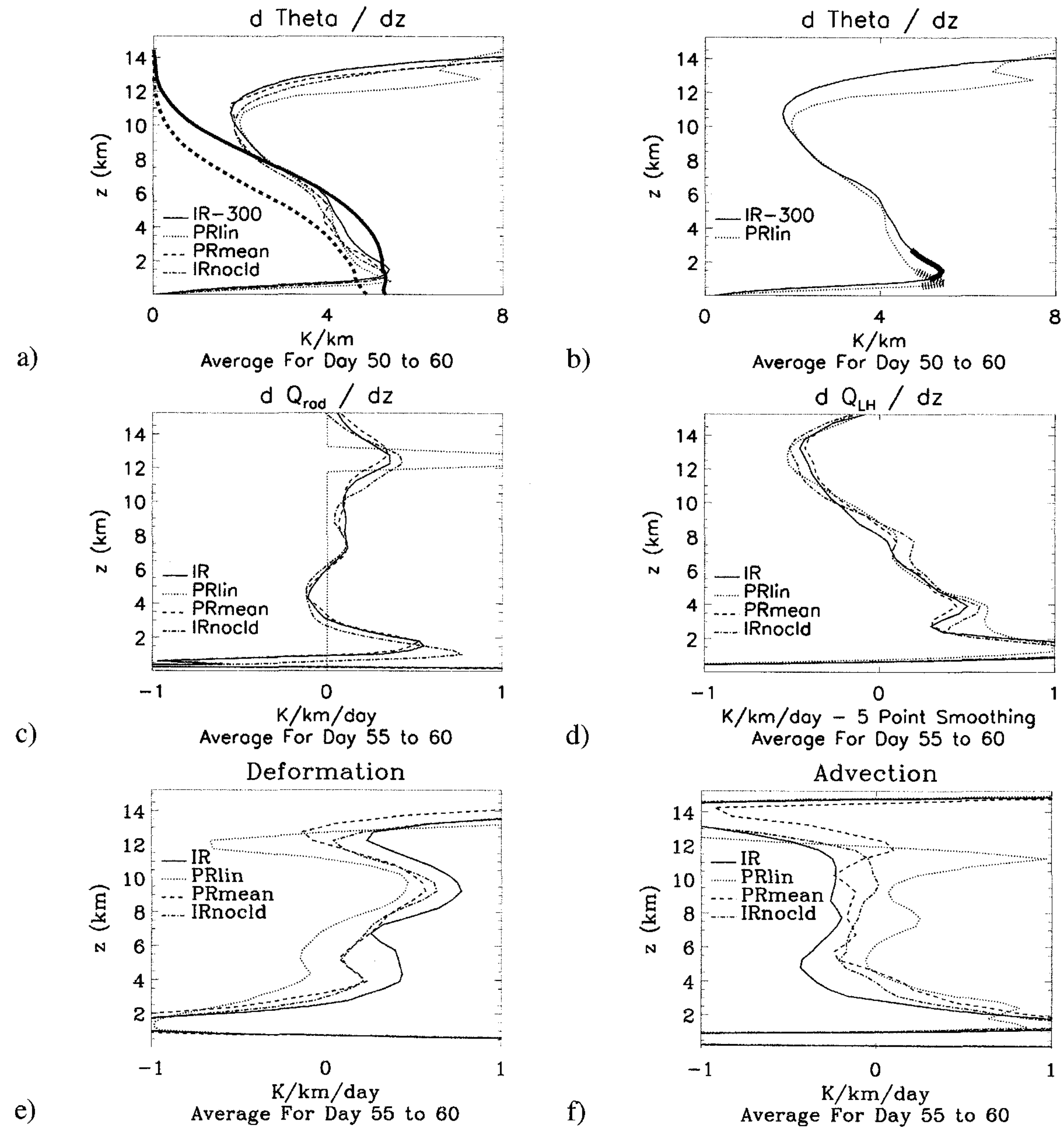

Figure 4.11: Comparison of the final 10 day, domain mean stability profile for, (a) $\frac{\partial}{\partial z}\theta$, (b) PR-lin and IR-300 stability comparison and the terms (see equation 4.3) involved in altering the stability. (c) $\frac{\partial}{\partial z}Q_{\mathrm{rad}}$, (d) $\frac{\partial}{\partial z}Q_{\mathrm{LH}}$, (e) deformation and (f) advection. Note that the heavy line in figure (a) is the 19.5C moist-adiabat while the heavy-dashed is the 14.5C moist-adiabat

training shallow cumulus that forms in the 1-6km layer will mostly likely preferentially detrain in that layer since $\frac{\partial \theta}{\partial z} > \frac{\partial \theta_{es}}{\partial z}$(340K). To examine those factors that contribute more specifically to local atmospheric stability variations observed in the experiments, consider the vertical derivative of the thermodynamic equation;

$$\underbrace{\frac{\partial}{\partial t}\frac{\partial \theta}{\partial z}}_{\text{local change}} = \underbrace{-\mathbf{u}\cdot\nabla\frac{\partial \theta}{\partial z}}_{\text{advection}} - \underbrace{\frac{\partial \mathbf{u}}{\partial z}\cdot\nabla\theta}_{\text{deformation}} + \underbrace{\frac{\partial}{\partial z}Q_{LH} + \frac{\partial}{\partial z}Q_{rad}}_{\text{diabatic source terms}} \tag{4.3}$$

where the right hand side contains four source terms, one due to advection, one due to deformation and the remaining two associated with the vertical derivatives of latent and radiative heating.

Figures 4.11c, d, e and f present domain averaged profiles of each source term calculated from the average of the last 10 days of the four 300K experiments. Notable are the differences of the radiative heating source terms (Fig. 4.11c) in the lower levels for the different experiments. This result could simply have been anticipated from the cooling rate profiles of Figs. 4.3a where the increase in cooling rate with height induces stabilizing effects below 3.5 km and the decrease cooling with height induces destabilizing effects between 3.5 km and 6 km in each of the three experiments that exhibit increased cumulus clouds. In a relative sense, the radiative cooling profile acts to enhance detrainment between 1-3 km and then promote growth up to 6 km where detrainment then occurs again. Such behavior is consistent with the observed low–level cloud detrainment levels documented in J95 and also consistent with the cloud top distributions.

Figure 4.11b highlights the mean stability states of the IR-300 and PR-lin experiments more clearly and one immediately notes that, although the lapse rates above 6km are similar, the IR-300 is characteristically more stable in the lower layers than is the PR-lin experiment. In particular, the mean stability profile appears to possess a more enhanced stable layer in the 1-3km layer, emphasized in the figure by the heavy portions of the plots. Careful study of Fig. 4.11a reveals that all experiments with a realistic vertical variations of radiation show this enhanced stability which can be attributed to the direct influence of radiative cooling in these experiments in altering the temperature field directly in a subtle manner when allowed to operate over long enough time periods. In these experiments, the spatial distribution of low-level radiative cooling is a relatively homogeneous feature which means it does not project readily onto wave structures and thus does not readily propagate away by wave action as suggested in Mapes and Zuidema (1996).

It is important to keep in mind that the actual stability profile in the 1-6km layer while influenced by radiative heating is shaped predominantly by the other source terms (4.3). The latent heating contribution shown in Fig. 4.11d is similar for all four experiments except where the profile is affected by the latent heating of cumulus clouds especially in the layer between 1-4 km. An interpretation of the LH source profiles is as follows. The general mean latent heating profile of the experiments is largely defined by the deep convective mode and the latent heating profile of this mode is typically approximated as a half sinusoid (e.g. Houze 1977). The differential of this profile is a sinusoid in quadrature, yielding a stabilization affect below the point of maximum heating and destabilization above this point. Superimposed on this effect is the heating by cumulus clouds. In this case, the heating profile can also be thought of as broadly defined as a half sinusoidal profile but now confined over a shallower layer (approximately between the surface and about 4-6 km with a maximum heating somewhere near the middle of this layer). This heating structure induces the tendency to stabilize the lower portion of this cumulus convective boundary layer and destabilize the upper half of the layer. The superposition of this effect on the deeper mode of heating is evident in Fig. 4.11d where the differences in the sources of stability between the PR-lin and other experiments shown is most marked in the region between about 2-5 km.

Both the deformation and advective terms are strongly dependent on the general circulation of the model making it difficult to draw general conclusions about the differences between the four experiments. To a first approximation, we can assume a deep solenoidal circulation exists between convecting and non-convective regions (e.g. Betts and Ridgway 1989; Mapes 2001). According to Fig. 4.11e, the advective term stabilizes the low layers below about 3 km and broadly destabilizes the upper layers, implying convection transports the more stable subsiding air into the convective region at the low-levels. The vertical component of the deformation term, $-\frac{\partial w}{\partial z}\frac{\partial \theta}{\partial z}$, is generally an order of magnitude larger than the horizontal component. As $\frac{\partial \theta}{\partial z} > 0$, a negative deformation term implies $\frac{\partial w}{\partial z} > 0$, such as that found in the accelerating portion of a convective core or the rising branch of a gravity wave. The opposite of this would be true for accelerating downdraughts and the subsidence portion of a gravity wave. Based on Fig. 4.11d, it would appear that the deformation term is dominated by subsidence processes. These results are consistent with the notions forwarded by Bjerknes (1938) in that the cloud mass flux acts to stabilize the cloud free environment, primarily through vertical motions.

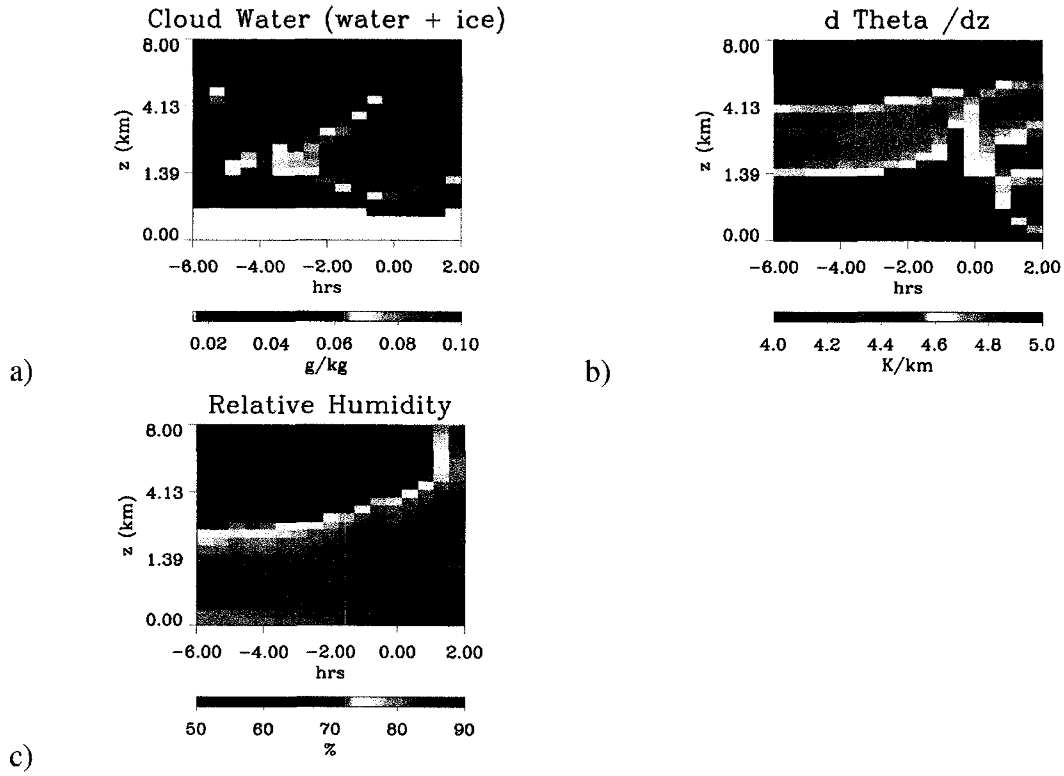

Figure 4.12: Composite analysis of the initial stages of deep convection for the Interactive Run over the final 5 days. The method used identifies 37 convective events, represented here. All plots are smoothed with a $z = 5$ vertical smoother. Cloud water (a) shows the build up to deep convection at time zero and $\frac{\partial}{\partial z}\theta$ (b) shows the erosion of the stable layer concurrent at this time while (c) shows the concurrent increase in value and vertical extent of relative humidity.

4.5. Life cycle of cumulus clouds

The results shown in Figs. 4.7 and 4.12 suggest that the development of moist domes are primarily a consequence of shallow convection mixing moisture in the vertical. Figure 4.7 compares a 10 day time series of cloud water, relative humidity and stability between the PR-lin and IR-300 experiments, averaged over a 1000km region of the model. The averaging region for the IR-300 experiment is centered on a moist dome whereas the location of this averaging region is less relevant for the PR-lin experiment since these quantities are more homogeneously distributed than in the IR-300 experiment. The contribution of radiative heating to stability (i.e. the dQ_{rad}/dz source term in eqn 4.3) is also provided in Fig. 4.7g for the IR-300 experiment only (since this contribution is zero in the PR-lin experiment). Contoured over both the radiative heating rate source and the stability (Fig. 4.7e, f and g) are the relative humidity values between 50-80% shown. The variability of relative humidity is greatest below 6km in the IR-300 experiment with values varying from less than 30% and greater than 80%. Such low-level variations are also observed in the real atmosphere (J95). The humidity of the PR-lin experiment is less variable rarely exceeding 70% in the 1.5-6 km layer.

Figures 4.7e and f also illustrates how the low–level stability below about 5km is also more variable than the more homogenous unstable air above. Although the atmospheric stability of the PR-lin and IR-300 experiments are broadly similar during periods of enhanced convection, there are subtle but important differences in the stability of both experiments. Both experiments show stable layers around the freezing level (also hinted at in Fig. 4.12b), although these levels are more stable in the IR-300 experiment suggesting that radiation further sustains these layers (e.g. Mapes and Zuidema 1996). Both experiments also reveal thin low–level stable layers around 1km that appear to be modulated on the timescale of the deep convection. J95 similarly observe that congestus clouds typically co-exist with trade cumulus clouds and that thin, low–level stable layers with little vertical moisture perturbation reside in the deep tropics. The origin of these trade like stable layers in these experiments has not been determined and they appear in all experiments, including the SST experiments discussed in the next section. More notable, however, are the enhanced stable regions that coincide with strong vertical gradients of moisture and the build up of water vapor in the IR-300 experiment (Fig. 4.7f, notably between days 55-57) and also evident in the PR-lin experiment around days 56-57 but with much less associated build up of moisture. It is also in this same region of the IR-300 experiment that the radiation contributions are largest as these too are affected most by sharp moisture gradients. Although these stable layers are a product of wave-scale dynamics in both experiments, radiation reinforces them in the IR-300 experiment. The connection between radiation stabilization effects and the vertical moisture gradient suggested by these experiments also supports the ideas described by Mapes and Zuidema (1996). More generally, radiation modulates the background environmental stability given that radiative cooling acts persistently and over wide spatial and relatively long time scales, clearly evident in Fig. 4.7g. Furthermore, the cumulus cloud activity in the periods of enhanced convection is greater for the IR-300 experiments than the PR-lin experiment and the moisture below 6km remains much higher during these periods of higher low-level stability.

Near day 57 of both experiments, the strong low-level inversion is removed with the rapid growth of congestus-like clouds which then develop into deep convection. In both experiments, deep convection is led by shallow convection but the existence of shallow convection does not necessarily always lead to deep convection. To illustrate the general behavior of the evolution from shallow to deep convection, a compositing method was developed based on a deep convection identification procedure. The procedure uses the surface precipitation fields smoothed with a $x = 12.5$km and $t = 45$min box smoother. Initiation of the core is identified as the earliest point in time and central point in space for a single closed 10 mm/hr (x, t) contour in the smoothed field. Only precipitation swaths that persist longer than three hours were then composited, thereby selecting only the larger and more persistent deep convective systems. The two dimensional fields from the model, captured at half hour intervals, are then averaged in a 'compositing box', defined as $x = [-30, 30]$km, $t = [-6, 2]$hrs, $z = [0, 8]$km from the core. This method identifies 69 convective events in the final 10 days of the IR-300 experiment. The results shown in Fig. 4.12 are smoothed with a vertical $z = 5$ point smoother and depict the mean of the x axis compositing box. In this way, the analysis provides the composite mean time evolution of cloud water, relative humidity and stability leading up to the time of a deep convective event. The abscissae in these figures are in hours prior and post the identified time of the convective core. Since the evolution depicted in this figure is similar for all experiments, only the cumulus clouds life cycle for the

IR-300 experiment is shown.

Figure 4.12a illustrates how cloud water builds in three apparent stages. The first is a semi homogenous shallow 'trade' cumulus layer with limited vertical growth up to -3 hours, probably due to a slight increase in surface winds and subsequent response of the CBL (Betts and Ridgway 1989). This is followed by a rapid deepening congestus phase associated with wave induced surface convergence up to time zero (not shown), at which point deep convection occurs as indicated by water values filling the troposphere. The stability profile (Fig. 4.12b) indicates a stability maximum between 1.4-4km during this first stage coinciding exactly with the location of the radiative forcing term of the stability equation (Fig. 4.11c). During the congestus phase, the stability reduces and it has a similar vertical extent to the cloud water field although it lags the latter by about half an hour. At time zero, the stability suddenly increases through a deep layer after which time two even stronger signals appear, one in the vicinity of the melting layer much as conjectured by J95 and one in the lower-levels, presumably due to the cold pools associated with deep convection (Tompkins 2001a). The sudden increase in stability through a deep layer, but still less than the stability at time -6hr, is indicative of a moist plume ascending a warmer adiabat. In general, the stability profiles do not resemble any single moist adiabat as a consequence of the combined effects of different processes acting in this composite box and the vertical dispersion of this adjustment process (Mapes 1993). Thus, we interpret the coherent signal between cloud water and stability as the direct effect of cumulus convection.

It appears that the cumulus in stage one ascend one adiabat, the congestus ascend an adiabat that is slightly warmer and then deep convection ascends the warmest moist adiabat. This implies that these various stages reflect different origins for the moist plume and/or different levels of entrainment into the plume, also implied by the lowering lifted condensation level (LCL) apparent in 4.12-a. This result is consistent with fig 4.12-c, which shows that the relative humidity also possesses similar vertical structure and time variations, supporting the idea of vertical mixing by detrainment into the stable layer. We note that the PW increases in the congestus stage (implied by Fig. 4.12-c). In this manner, successive cycles of shallow convection can penetrate deeper because they ascend ever warmer adiabats and have reduced effects from entrainment due to the near moist-neutral stability and increased humidity in the previously adjusted layers. The plume then encounters the higher stability above the previous clouds location and detrains and destabilizes there. The processes continuing until the cumulus clouds reach around 6km where the buoyancy increases markedly, as also shown in Mapes (2001). At this stage, the pressure perturbations and sheer size of the deep convection keep the gross entrainment to a minimum and, thus, allow moist plumes from the surface to ascend their warmest adiabats. In this light, we attribute the mean reduction of low-level stability, as compared to a deep moist adiabat, in the domain-time mean plots (Fig. 4.11a) and in regions of shallow convection in the time-mean plots (Fig. 4.6) as being due to cumulus clouds ascending cooler adiabats while the low–level 'notch' as being primarily due to radiation. In the next section, the effects of SST show that cumulus clouds become less prevalent at cooler SST's and the low-levels begin to better approximate the surface moist adiabat.

In summary, deep, high moisture and moisture distributions, along with convection and wave dynamics, alters the environmental stability which then effects the detrainment of moist plumes. Radiation acts persistently over large regions and over relatively long time scales of these experiments to produce a significant influence on the background stability profile such that detrainment in the 1-3km layer and entrainment in the 3-6km layer is enhanced. In regions of sufficient moisture, cumulus clouds form and detrain into the low–level stable layers, increasing and deepening the moisture while also destabilizing the layer in a local region, thereby providing a preferred pathway for deeper convection. This cycle of radiative and wave stabilization, cloud destabilization, entrainment and detrainment by ever deepening convection ascending ever warmer adiabats alters the mean state in this mixing layer so that its gross stability does not match the upper levels, which only ever feel the deepest convection. In this proposed mechanism, the affect of radiation on this cycle is sensitive to the absolute moisture profile and through feedbacks on stability and clouds act to promote these ‘moist domes’.

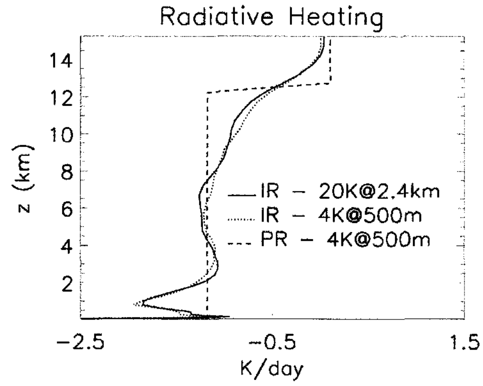

a)

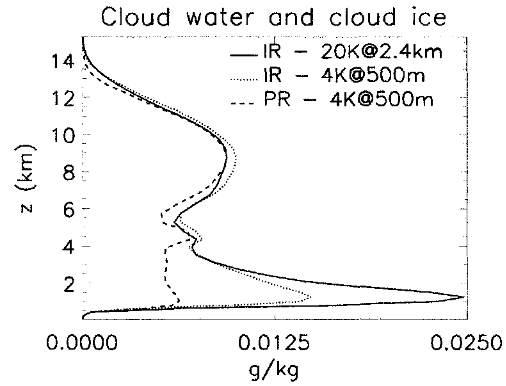

a)

Figure 4.13: Comparison of day 20-30 (a) Radiative heating profile and (b) domain mean cloud water for the increased grid resolution sensitivity experiments. Note that the large domain, coarse grid IR experiment line is included for comparison but that the experiments produce general circulations that preclude this from being conclusive to just grid resolution.

4.6. Sensitivity Experiments

4.6a. Grid Resolution Sensitivity

It was emphasized from the outset that the model resolution only marginally resolves deep convection let alone the shallower 'cumulus' convection. The IR-300 and PR-lin experiments were repeated on the same domain of 8192 grid points but at 500m resolution thus shrinking the overall domain size from approximately 20,000 km to slightly over 4,000 km. Unfortunately, computational limitations preclude the option of running these finer resolution experiments on the same domain and the smaller domain alters the general circulation of the model to an extent that a direct one-to-one comparison between these fine grid results to the coarse grid experiments is inconclusive. The radiative cooling properties are however largely independent of model resolution and, as a result, it is to be expected that the bulk equilibrium state of the fine-scale experiments should resemble those of the coarser scale experiments described in greater detail above despite the differences in circulation.

Figure 4.13a compares the day 20-30 radiative heating profile for the fine grid ex-

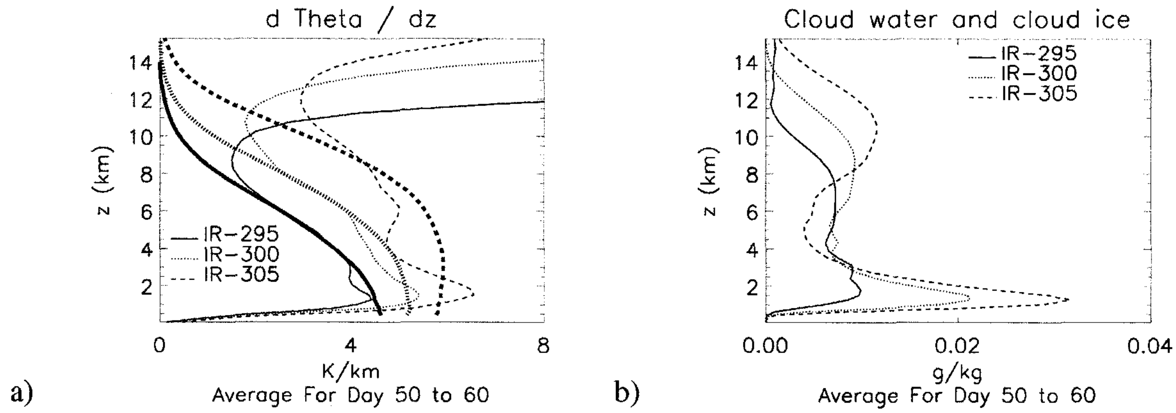

Figure 4.14: Final 10 day comparisons for the three sea surface temperature sensitivity experiments. (a) mean static stability with heavy lines denoting characteristic pseudo–moist adiabats and (b) mean cloud water and ice.

periment with the 50-60 day averaged profile of the IR-300 coarse grid experiment. The smaller domain experiments reach equilibrium much faster than the larger domain models. Clearly, the radiative profiles for the IR-300 coarse and fine grid experiments are very similar to each other as expected with only slight differences in the 2-4km layer of interest. Figure 4.13b compares the equilibrium period domain mean cloud water and shows the same behavior as before, with the IR-300 run producing enhanced cumulus cloud amounts over the matching resolution PR-lin run. The cloud water of the fine grid experiment though is significantly less than the coarse grid counterpart and we can not conclude whether this is because of the increased resolution of the cumulus clouds or because the general circulation is changed so significantly. Nevertheless, the general effect of the low-level radiative cooling enhancing cumulus clouds is repeated in these experiments suggesting the result discussed are not entirely a consequence of model configuration.

4.6b. Sea Surface Temperature Sensitivity

The mechanism discussed in section 5 suggests that increased cumulus clouds will occur when low-level radiative cooling is increased. The sensitivity results described above further suggest that the cooling has little dependence on model resolution as it arises from elementary absorption and emission processes that are proportionally dependent on the local column water vapor partial pressure of the lower model atmosphere. As shown in Fig. 4.3c, this cooling is sensitive to SST due to the intimate relationship between the two (e.g. Stephens 1990).

The bulk effects of SST on the equilibrium are explored further in Fig. 4.14 which compares the final 10 day domain mean vertical profile of (a) static stability and (b) cloud water and ice. Recall that Fig. 4.3c and d depicts the 10 day mean radiative and latent heating profiles of these experiments. Characteristic pseudo-moist adiabats are computed for each experiment and are shown as the heavy lines in Fig. 4.14a. The IR-305 experiment shows increased low-level radiative cooling with the cooling maximum rising in height causing a deeper layer of higher static stability leading to more cumulus clouds. We note that the characteristic low-level maximum of stability (the 'notch' emphasized as the bold portions of the plots) is sensitive to SST and further that the low-level departure of potential temperature from a moist adiabat amplifies with SST. This result is consistent with the notion that the 'notch' is related to the radiative stabilization perturbation while the lapse rate deviation is related to increased cumulus cloud entrainment activity.

The analysis of the hydrologic cycle discussed in section 4 is repeated for the other two SST experiments with new OLR thresholds defined for these experiments. Table 4.3 summarizes the OLR thresholds and the water budget parameters grouped by the three regimes in the same manner as Table 4.2. The quantities listed show how the bulk properties of the hydrological cycle systematically vary with SST. For the IR-295 experiment, cumulus clouds contribute relatively little to the hydrologicial cycle, and presumably then the thermodynamic and dynamic budgets, with most of the model moisture coming from evaporation in the clear sky regimes being offset by rain-out by deep convection. In contrast, cumulus play an increasingly important role in the IR-305

Cloud Regime	Sampling Frequency	CWP	IWP	LHF	Precipitation
Deep Convection					
IR-295 (< 235)	19	91	95	24	99
IR-300 (< 235)	16	51	98	18	86
IR-305 (< 235)	14	35	97	16	75
Cumulus Convection					
IR-295 (235-250)	9	8	1	11	1
IR-300 (235-273)	20	42	2	20	14
IR-305 (235-300)	66	61	3	63	25
Clear-Sky					
IR-295 (> 250)	72	1	4	65	0
IR-300 (> 273)	64	7	0	62	0
IR-305 (> 300)	20	4	0	21	0

Table 4.3: Same as table 4.2 except for the three SST sensitivity experiments. Note that the OLR filter now differs for each experiment.

experiment (compared to the IR-300 experiment) contributing 25% of the precipitation and 63% of the latent heat flux. Cumulus cloud amount is also much greater as the subsidence areas become moist enough to support cumulus clouds. Thus, a lower SST limit appears to exist for moist domes.

Figure 4.15 is the same as Fig. 4.10 except computed using new OLR thresholds specifically selected for each SST experiment. The figure shows a clear trend in increased contributions from cumulus clouds with warmer SSTs (middle panel). The variance and mean values of precipitable water also increase with SST, the former indicating a strengthening in the up-moist/down-dry circulations as SST increases, possibly due to the enhanced upper-level cooling (Mapes 2001, and Fig. 4.3c) and/or the strengthening of convective systems (not shown).

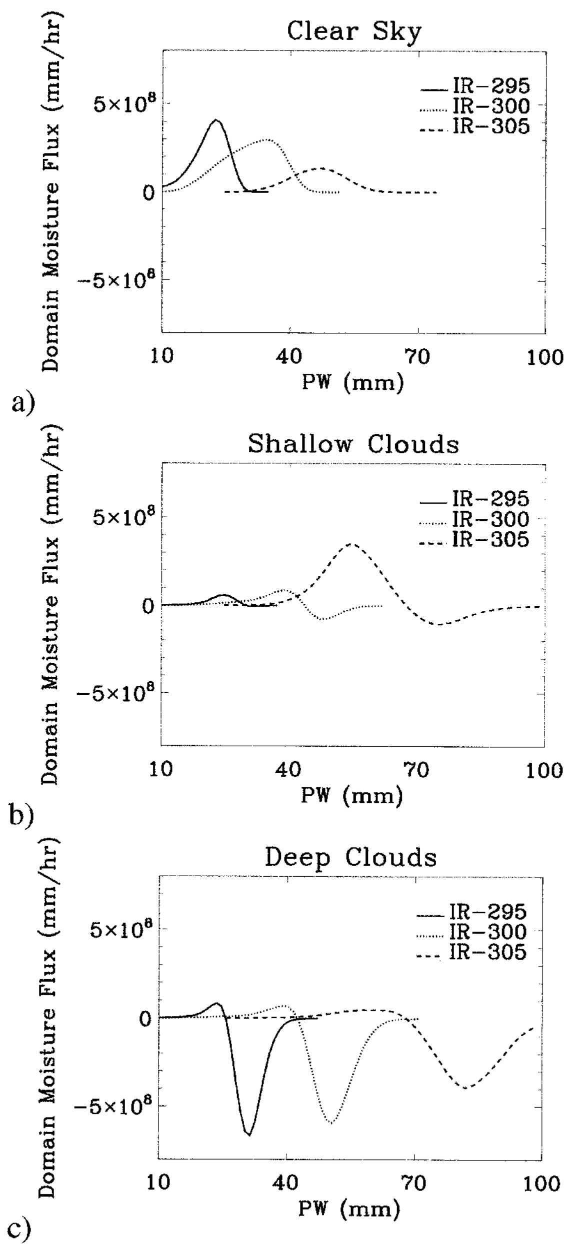

Figure 4.15: Same as Figure 4.10 except for the three SST sensitivity experiments.

4.7. Summary

This chapter demonstrated that 2D RCE-CRM reproduced many of the observed tropical phenomena, such as: (i) trimodal cloud distributions with bimodal precipitation loss; (ii) low-level (1km) stable layers with no moisture perturbation and ones with moisture perturbations; (iii) freezing level stable layers in and away from the deep convecting zones; (iv) realistic humidity profiles (especially of interest 1-5km); (v) reduced lapse rates in the 1-5km zone when compared to a deep moist adiabat; (vi) a stable bulge in the 1-3km layer; (vii) convectively-coupled gravity waves with counter propagating squall lines (i.e. reminiscent of the superclusters defined by Nakazawa 1988, and of the theory introduced in chapters 2 and 3).

The inhomogeneous distribution of precipitable water (PW) and surface precipitation has previously been recognized in these types of experiments but features such as its spatial and time scale, propagation, intensity and relation to radiative forcing remain poorly understood. In this investigation, we explored the affect of vertical variations of radiation in promoting vertical distributions of clouds. These shallow clouds, nominally representative of shallow cumulus and cumulus congestus, were integral in creating the vertically increased moisture regions with lower static stability, which we termed as 'moist domes'. The increased moisture in the moist dome was shown to be directly attributable to shallow clouds enhancing surface evaporation, subsequently being transported in the vertical by deepening shallow convection, creating a deeper moist layer (1-5km) than would otherwise just exist in the tropical boundary layer.

In general, the atmosphere adjusts towards the in–cloud moist adiabat (Bretherton and Smolarkiewicz 1989), thus explaining why the observed (and modeled) troposphere grossly resembles that of a saturated surface parcel, except in regions below 5km and near the tropopause. The resulting lapse rate for a warmer moist adiabat is always greater than that of a cooler moist adiabat. Hence, for shallow entraining cumulus that ascend cooler adiabats, the gross troposphere appears stable and the plume detrains, noting that this does not imply zero buoyancy, just that buoyancy decreases with height. In this manner, deepening shallow clouds penetrating the overlying 'stable layer' were attributable to a reduction in the time-mean static stability in this layer as compared to non convecting regions. Thus, the process of deepening shallow cumulus is congruent with increasing moisture in the vertical and decreasing lapse rates, allowing the next cycle to ascend a warmer adiabat and penetrate vertically further, this process going on until, possibly, deep convection. In this context, the moist dome system creates a neutral lapse-rate pathway for deep convection while also reducing entrainment for deep convection when it forms.

The moist dome is enhanced by radiation due to the enhanced absorption that occurs in the atmospheric window region of the IR absorption spectrum through a mechanism known to be proportional to water vapor partial pressure. This enhanced low-level cooling induces a mean stabilizing affect in the 1-3km layer that promotes plume detrainment and, thus, shallow convection. Although, we take note that radiation is not the only process important to low-level stability. The increased stability prevents deep convection from immediately forming and allows larger values of moisture to build by the evaporation processes associated with the shallow convection. Since this radiation feedback is sensitive to mean moisture path, it is dependant on SST. In this manner, it was shown that moist domes appeared to be active only for when the SST $>$ 295K and that only in those cases did the low-level static stability deviate from that of a deep moist adiabat, thus confirming our hypothesis.

We believe that moist domes are active in those regions of the deep tropics where high PW exist, for example the tropical west Pacific (TWP). While it is widely recognized that column moisture has a substantial effect on convection and subsequently surface precipitation, the moist dome system provides additional mechanisms to promote this observed relation. The benefits of the moist dome system rely on the prevention of the immediate formation of deep convection such the the region must undergo a shallow cumulus transition that increases the PW while decreasing the static stability, this having two major benefits;

(i) since the deep convection that *may* ensue is a large sink of moisture, building up moisture for the event may allow further events to take place in a similar location. Also, the increased mid-level moisture reduces the effects of downdraughts into the sub-cloud layer.

(ii) As $N^2 = \frac{g}{\theta}\frac{\partial \theta}{\partial z}$ and $w^2 \propto \frac{\partial p}{\partial z}/N^2$ (Holton 1992), a reduction in the static stability implies that for a given vertical pressure gradient, the vertical motion is enhanced. For the tropical atmosphere and this model, large scale waves dominate (Wheeler and Kiladis 1999) and a reduced static stability also implies a slower wave propagation speed (Fulton and Schubert 1985; Emanuel et al. 1994, and others). Both effects enhance the triggering potential for such systems which then may positively feedback to the energy of that system.

It is convenient to cast these processes into four conceptual phases as described in this chapter, noting that they are broadly consistent with the observations of Stephens et al. (2004a).

Phase 1 Initially, the region is under the influence of a stable layer with little surface convergence and the cloud mode is trade cumulus like as described by Betts and Ridgway (1989). Radiation strongly acts to enhance this stable layer by the large gradient of moisture at the top of the shallow moist layer much in the manner suggested by Mapes and Zuidema (1996).

Phase 2 Some disturbance forces convection which then builds the moist dome in the vertical, as described previously. The moisture increases in the vertical while the static stability decreases.

Phase 3 Deep convection may trigger or be ongoing and in balance with the shallow convection moisture sources. The large scale forcing may leave the region but if the moisture remains adequate, the region will remain suitable for deep convection. Furthermore, the radiation mechanism is weekend by the reduced gradient of moisture in the vertical as compared to surrounding regions in phase 1 or 4 but will still promote shallow cumulus modes.

Phase 4 The region is depleted of its deep moisture by convective processes and/or the influence of a strong stabilizing process. The decrease of moisture in the vertical and increase in the low-level stability returns the system back to Phase 1.

In this manner, the TWP may be semi-permanently in phase 2 and 3 exhibiting trimodal cloud structures, deep moisture profiles and decreased low-level static stability (Johnson et al. 1999). Convectively-coupled waves appear to exhibit all phases as they pass through a region but the processes that define the scale of a moist dome in this mode are unresolved and is a topic of future research.

Chapter 5

Conclusions

5.1. A New Theory

This investigation outlines a new theory for convectively-coupled waves based on a method for obtaining the particular solution of the forced β-plane system with constant damping. Forced waves were shown to be governed by two equations, one for amplitude and the other for frequency (phase speed). The amplitude equation was shown to related to the real energy of the wave and the forcing term in this equation was referred to as the 'real power' of the forcing. The frequency equation was shown not to relate to the real energy but was conjectured to relate to the propagation of energy out of the forced region. The forcing term in this equation was termed the 'radiant' power. This derivation was then applied to the convectively coupled wave problem under the following three concepts:

- a convectively coupled wave is a *forced* wave with the forcing defined by convective processes.
- a convectively coupled wave is a coupled feedback system, wherein the forcing and wave mutually reinforce one another.

- a convectively coupled wave exhibits phase-locked structures as it approaches steady state.

The particular solution of the forced problem showed that the phase speed difference between the forcing and that of the wave, denoted as δc, is an essential parameter of the forced problem. Consideration of a general forcing revealed that the frequency of forced waves approached the frequency (phase speed) of the forcing in the steady state limit and this was termed 'phase-lock'. Furthermore, observed properties of convectively coupled waves, in particular coherent structures outside the region of forcing and the observed energy spectra, could only be explained if $\delta c \neq 0$, nullifying the apparent paradox that attempts to match the speed of the forcing to that of the wave.

The notion of phase locking of the steady convectively coupled wave, which in this study refers to a wave response that couples to the forcing, was used to develop a number of properties of the coupled system. The properties that govern phase-locking of the wave to the forcing were introduced drawing from the concepts developed from radio engineering. It was shown that the condition for phase locking is:

$$|k\delta c|/\gamma < 1$$

and, depending on the sign of δc, a stably phase-locked response either leads or lags the forcing in its respective propagation direction. The implications of this to the convectively coupled wave are;

(i) convective forcing and waves of similar speeds (i.e. $\delta c \to 0$) will phase lock more readily but for such circumstances the response of such a system is trapped in or near the region of forcing. Furthermore, if $\delta c = 0$, the waves will always be in phase but not phase-locked since phase-locking requires the response wave to change speed to acquire the other. We illustrate in the next chapter that $\delta c \to 0$ cannot maintain the coupled system.

(ii) larger scale waves (i.e. $k \to 0$) phase-lock more readily than smaller scale waves, suggesting that the observed coherent structures of convectively coupled waves are preferentially large;

(iii) the ability of the wave to phase-lock to convection will be highly dependent on the energy of the wave and that of the forcing. For example, weakly forced systems with $B \to 0$ and thus $\gamma \to 0$ or highly energetic waves ($A \to \infty$ and thus $\gamma \to 0$) will tend not to phase lock. Thus the parameter γ provides some measure of the ability of the wave to couple to and feedback back on its forcing.

5.2. The Forced Kelvin Wave

The problem of the forced Kelvin wave was studied to illustrate some fundamental concepts of the theory developed. The main findings of this part of the research are:

(i) The solutions predict that a single wave produces two wave fronts that propagate at different phase speeds, one with a speed equal to the forced response and the other with a speed equal to the free response, explaining the observed energy spectra apparent in Two-Dimensional Fourier Transform (2DFT) analysis of OLR and other meteorologic variables (Wheeler and Kiladis 1999; Wheeler et al. 2000). We also note that a simple comparison of the apparent β-plane frequency to that of a 2DFT of the physical solution is ambiguous.

(ii) Assuming a deep mode vertical structure, then conditions of low level convergence is required to sustain the (convective) forcing, and conversely divergence acts to destroy this forcing, then we show that the condition that $\delta c < 0$ provides a system of positive feedback between the wave and the forcing. We also show that $\delta c = 0$ results in a wave that is trapped to the forcing whereby half the domain comes under the influence of divergence which we suggests acts to shrink the forcing eventually eliminating it and the wave completely. The behavior of the damped solutions is similar to the undamped solutions except that the the divergence field, confined to the wave fronts of the undamped solution, extend out over the entire region of influence. The physical scale of this influence in the zonal direction was shown to be

$$R_{ix} \propto \delta c/\epsilon$$

which reduces to the scale expected for a stationary forcing ($\delta c \to c$) (Gill 1980). Furthermore, these arguments are general to any vertical structure.

(iii) Consideration of the critical assumptions demonstrated that a mutually supporting convectively coupled system can only exist for the conditions;

$$-\infty < \delta c < 0$$

and that a convectively coupled system cannot exist at the bounds $\delta c \to -\infty$ and $\delta c \to 0$. It was conjectured that an optimal value of δc exists between these bounds and we deduce the relationship for this optimal value as

$$\delta c \propto -\epsilon \sigma_x$$

defined in terms of the scale of the forcing (σ_x) and rate of damping (ϵ). This relation was derived assuming that an optimal configuration of the convectively coupled wave is one for which the rate that wave energy propagates out of the forcing region (the derived radiant power) matches the rate that energy is created by the forcing (derived true power). A more mechanistic explanation of the propagation of a convectively coupled wave that leads to the same relationship is also presented based on the first two internal baroclinic modes in the context of Bjerknes (1938) "uniform adjustment" and Mapes (1993) gregarious convection hypotheses applied to the large scale flow. We show how this relationship correctly estimates the phase speeds of convectively-coupled Kelvin waves and, possibly, the MJO as depicted by Wheeler et al. (2000) using observed scales of convective forcing for typical values of σ_x. As a diagnostic equation, the relation also predicts damping rates consistent with the study of Wu et al. (2000a). Furthermore, the relation adheres to the multi-scale view of convectively-coupled systems with increasing propagation speeds at smaller scales (Nakazawa 1988; Straub and Kiladis 2002).

5.3. A Conceptual View

Figure 5.1 is a schematic of the monochromatic solution of convectively coupled waves. The figure schematically portrays the typical equatorial region with increased Sea Surface Temperatures (SST) in the tropical western Pacific (TWP) with associated increased moist static energy in the boundary layer there. The tropical eastern Pacific (TEP) is a region of cooler SST and lower moist static energy. We envisage the TWP as a region of strong convection that forces waves, emanating 'dry' or 'free' waves, for example the 45 ms^{-1} deep wave. The only waves that reach the TEP are the intrinsically fast waves by the nature of their large region of influence, as observed (Milliff and Madden 1996; Wheeler et al. 2000). Furthermore, these fast waves will tend to be highly energetic since one might assume they may have been coupled and amplified as they crossed the TWP, resulting in large (A). As these waves reach the TEP, the wave induced subsidence will adjust the atmosphere towards a moist adiabat reminiscent of the TWP. While this would imply increased shallow convection, unlike the RCE-CRM models experiments discussed in chapter 4, the shallow convection will be unable to ever achieve a moist adiabat of that of the upper troposphere as the SST is less in the TEP than the TWP and the effect of shallow cumulus would only excite a weak moist dome. The result is thus weaker or non-existent convection, implying that $B_{\text{TWP}} > B_{\text{TEP}}$ and thus:

$$\gamma_{\text{TWP}} >> \gamma_{\text{TEP}}$$

Hence, the condition for phase-locking is more readily achieved in the TWP than the TEP and that convectively-coupled systems will decouple or not form at all in the TEP.

5.4. The Effects of Shallow Clouds on Wave Forcing

The theory assumes that the forcing is given and predicts a continuous spectrum of wave speeds and, while this behavior is broadly observed for the Kelvin wave and MJO (Masunaga et al. 2006), there is notable structure in observed OLR occurring as spectral peaks in k (Wheeler and Kiladis 1999) suggesting that notable structure also exists in σ_x. We suggest that such structure is governed by other processes that influence the diabatic heating, for example the Humidistat feedback (Stephens et al. 2004a), meso/multi-scale convection (Nakazawa 1988; Mapes and Houze 1995), convective aggregation (Tompkins 2001b; Bretherton et al. 2005) and the influences of shallow convection.

Using large domain radiative convective equilibrium cloud resolving model (RCE-CRM) experiments, we concentrated on the role of shallow clouds in shaping the heating structures so integral to the findings just mentioned. It was found that deep convection always occurred in regions of high column precipitable water, a finding well noted in many such experiments. We termed these regions 'moist domes' because of their appearance as vertically stretched domes of increased relative humidity. These regions were shown to coincide not only with the deep convection but also copious amounts of shallow clouds. The low level static stability in the moist domes was shown to be episodic in nature with periods of increased stability and decreased cumulus cloud development and, conversely, with decreasing stability and increasing cumulus cloud development. It was revealed by a compositing technique that identified deep convective events that deep convective events are always preceded by deepening shallow cumulus convection associated with decreasing low-level static stability and that the decreasing static stability was directly attributable to the shallow cumulus convection.

The moist dome system is enhanced by radiation due to the enhanced absorption that occurs in the atmospheric window region of the IR absorption spectrum through a mechanism known to be proportional to water vapor partial pressure. This enhanced low-level cooling induces a mean stabilizing affect in the 1-3km layer that promotes plume detrainment and, thus, shallow convection. We take note, however, that radiation is not the only process important to low-level stability. The increased stability prevents deep convection from immediately forming and allows larger values of moisture to build by the evaporation processes associated with the shallow convection. Since this radiation feedback is sensitive to mean moisture path, it is dependant on SST. In this manner, it was shown that moist domes appeared to be active only for when the SST $>$ 295K and that only in those cases did the low-level static stability deviate from that of a deep moist adiabat, thus confirming our hypothesis that shallow cumulus clouds are the cause for low-level static stability deviations in observed soundings.

We believe that moist domes are active in those regions of the deep tropics where high PW exist, for example the tropical west Pacific (TWP). While it is widely recognized that column moisture has a substantial effect on convection and subsequently surface precipitation, the moist dome system provides additional mechanisms to promote this observed relation. The benefits of the moist dome system rely on the prevention of the immediate formation of deep convection such the region must undergo a shallow cumulus transition that increases the PW while decreasing the static stability, this having two major benefits;

(i) since the deep convection that *may* ensue is a large sink of moisture, building up moisture for the event may allow further events to take place in a similar location. Also, the increased mid-level moisture reduces the effects of downdraughts into the sub-cloud layer.

(ii) As $N^2 = \frac{g}{\theta}\frac{\partial \theta}{\partial z}$ and $w^2 \propto \frac{\partial p}{\partial z}/N^2$ (Holton 1992), a reduction in the static stability implies that for a given vertical pressure gradient, the vertical motion is enhanced.

For the tropical atmosphere and this model, large scale waves dominate (Wheeler and Kiladis 1999) and a reduced static stability also implies a slower wave propagation speed (Fulton and Schubert 1985; Emanuel et al. 1994, and others). Both effects enhance the triggering potential for such systems which then may positively feedback to the energy of that system.

5.5. Future Work

The current work only considers the forced Kelvin wave in detail while we have stated that only about half the power exists in Kelvin waves for the first two internal modes. Hence, calculations of the full power spectrum for all waves is the immediate next step. Following this, specific consideration of the MJO and explanation for the lack of the MJO in GCM simulations needs to be addressed. The concepts introduced to explain the observed features of the convectively-coupled waves can be considered a new adaptation of wave-CISK and further exploration of wave CISK within the context of the theory developed deserves further attention.

The RCE-CRM models are also an ideal environment for understanding some of the more elementary features of the meso- and cumulus scale interactions that presumably govern the forcin. We plan on continuing to use these models to better understand the factors that shape the forcing function and, in particular, the mechanics behind water vapor self-aggregation. Since these models contain convectively-coupled waves, a more critical assessment of the theory derived here is planned to hopefully elucidate some of the processes that couple the large range of scales that appear to be relevant to convectively coupled waves.

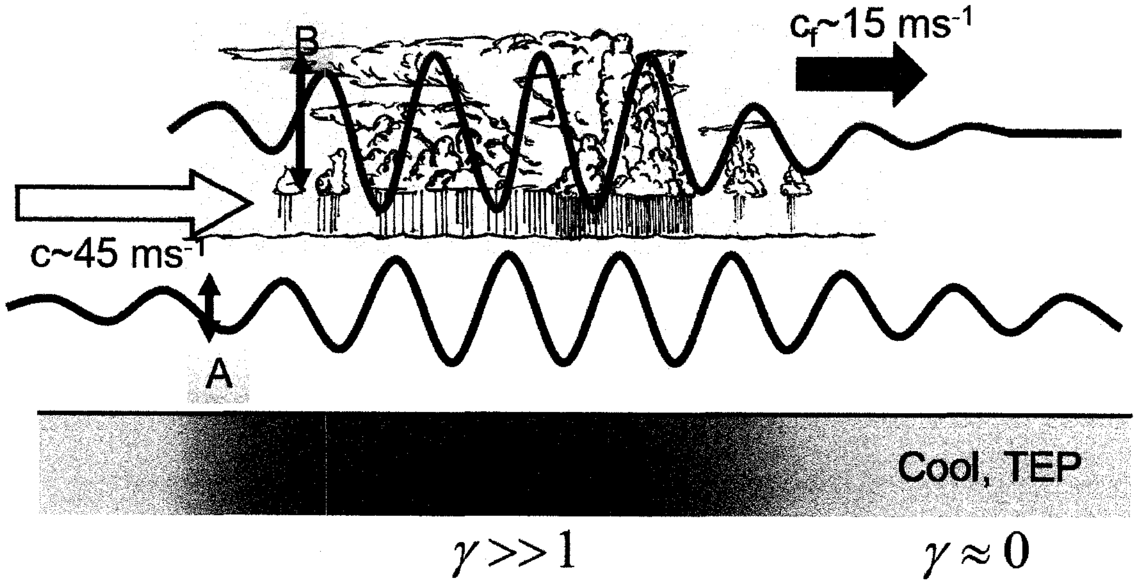

a)

Figure 5.1: Conceptual view of the forced wave (B) and wave response (A) as it varies from the tropical west Pacific (TWP) to the tropical east Pacific (TWP). The amplitude of A and B notionally indicate the strength of the wave and forcing, the ratio of which is γ whose value determines the ability to phase lock.

Appendix A

Generalized Vertical Co-Ordinate On a Cartesian Plane

The derivation for a general vertical co-ordinate is now presented. We wish to convert some variable ψ from one set of dependant variables to another but where only the vertical co-ordinate is changed, such that;

$$\psi\,(x, y, z, t) \rightarrow \psi\,(x, y, \eta(x, y, z, t), t)$$

Where the new vertical co-ordinate $\eta(x, y, z, t)$ is arbitrary. One condition on η is that it must be monotonic so that every vertical level has a definite position. It would first help to restate the quasi-static primitive equations in cartesian coordinates, explicitly stating where the vertical co-ordinate is held constant with respect to a differential. Note that the f-plane approximation has been made.

$$\frac{Du}{Dt} = -\frac{1}{\rho}\left(\frac{\partial p}{\partial x}\right)_z + fv + F_x \tag{A.1a}$$
$$\frac{Dv}{Dt} = -\frac{1}{\rho}\left(\frac{\partial p}{\partial y}\right)_z - fu + F_y \tag{A.1b}$$
$$\frac{\partial p}{\partial z} = -\rho g \tag{A.1c}$$
$$\frac{D\rho}{Dt} + \rho\left[\left(\frac{\partial u}{\partial x}\right)_z + \left(\frac{\partial v}{\partial y}\right)_z + \frac{\partial w}{\partial z}\right] = 0 \tag{A.1d}$$
$$C_p\frac{DT}{Dt} - \frac{1}{\rho}\frac{Dp}{Dt} = Q \tag{A.1e}$$
$$p = \rho RT \tag{A.1f}$$

Where

$$\frac{D}{Dt} = \left(\frac{\partial}{\partial t}\right)_z + u\left(\frac{\partial}{\partial x}\right)_z + v\left(\frac{\partial}{\partial y}\right)_z + w\frac{\partial}{\partial z} f = 2\Omega\sin\theta$$

All terms with respect to z surfaces must be transformed to be with respect to η surfaces. Using the chain rule on some variable ψ;

$$\left(\frac{\partial \psi}{\partial t}\right)_z = \left(\frac{\partial \psi}{\partial t}\right)_\eta\left(\frac{\partial t}{\partial t}\right)_z + \left(\frac{\partial \psi}{\partial x}\right)_\eta\left(\frac{\partial x}{\partial t}\right)_z + \left(\frac{\partial \psi}{\partial y}\right)_\eta\left(\frac{\partial y}{\partial t}\right)_z + \frac{\partial \psi}{\partial \eta}\left(\frac{\partial \eta}{\partial t}\right)_z$$

Knowing that in the natural cartesian co-ordinate system, (x, y, z, t) are all independent and orthogonal, they have no derivatives amongst them, thus the first and last terms on the right hand side are zero. Then, following the same procedure for x and y;

$$\left(\frac{\partial \psi}{\partial t}\right)_z = \left(\frac{\partial \psi}{\partial t}\right)_\eta + \frac{\partial \psi}{\partial \eta}\left(\frac{\partial \eta}{\partial t}\right)_z \tag{A.2a}$$
$$\left(\frac{\partial \psi}{\partial x}\right)_z = \left(\frac{\partial \psi}{\partial x}\right)_\eta + \frac{\partial \psi}{\partial \eta}\left(\frac{\partial \eta}{\partial x}\right)_z \tag{A.2b}$$
$$\left(\frac{\partial \psi}{\partial y}\right)_z = \left(\frac{\partial \psi}{\partial y}\right)_\eta + \frac{\partial \psi}{\partial \eta}\left(\frac{\partial \eta}{\partial y}\right)_z \tag{A.2c}$$

Special care must be taken with the z-ordinate;

$$\begin{aligned}
\frac{\partial \psi}{\partial z} &= \left(\frac{\partial \psi}{\partial t}\right)_\eta \frac{\partial t}{\partial z} + \left(\frac{\partial \psi}{\partial x}\right)_\eta \frac{\partial x}{\partial z} + \left(\frac{\partial \psi}{\partial y}\right)_\eta \frac{\partial y}{\partial z} + \frac{\partial \psi}{\partial \eta}\frac{\partial \eta}{\partial z} \\
&= \frac{\partial \psi}{\partial \eta}\frac{\partial \eta}{\partial z}
\end{aligned} \tag{A.3}$$

Substituting (A.2a)-(A.3) into the material derivative (A) for an unknown ψ;

$$\begin{aligned}
\left(\frac{D}{Dt}\right)_z &= \left(\frac{\partial}{\partial t}\right)_\eta + u\left(\frac{\partial}{\partial x}\right)_\eta + v\left(\frac{\partial}{\partial y}\right)_\eta \\
&\quad + \left[\left(\frac{\partial \eta}{\partial t}\right)_z + u\left(\frac{\partial \eta}{\partial x}\right)_z + v\left(\frac{\partial \eta}{\partial y}\right)_z + w\frac{\partial \eta}{\partial z}\right]\frac{\partial}{\partial \eta} \\
&= \left(\frac{\partial}{\partial t}\right)_\eta + u\left(\frac{\partial}{\partial x}\right)_\eta + v\left(\frac{\partial}{\partial y}\right)_\eta + \dot{\eta}\frac{\partial}{\partial \eta} \\
&= \left(\frac{D}{Dt}\right)_\eta
\end{aligned}$$

Note that the new form of the material derivative is designated specifically as the $\left(\frac{D}{Dt}\right)_\eta$. Hence, $\dot{\eta} = \left(\frac{D\eta}{Dt}\right)_z = \left(\frac{D\eta}{Dt}\right)_\eta$ but that this second form actually yields no information. From here on, subscripting on the $\frac{D}{Dt}$ operator is dropped due to their equivalency (except when calculating $\dot{\eta}$). Physically, $\dot{\eta}$ is the particle velocity perpendicular to η surfaces. Similarly, (u, v, w) are all velocities along the natural orthogonal variables (x, y, z), respectively. For example, $w = \frac{Dz}{Dt}$ and so forth. Hence, special care must be taken when w appears explicitly in the equations as we wish the equations to be with reference to a new, arbitrary vertical co-ordinate. As this arbitrary co-ordinate is not necessarily orthogonal to (x, y, t), an expression relating w to the new velocity $\dot{\eta}$ is desired. As w only appears in the continuity equation (A.1d) as $\frac{\partial w}{\partial z}$, we can guess this to be our desired form;

$$
\begin{aligned}
\frac{\partial \dot{\eta}}{\partial \eta} &= \frac{\partial}{\partial \eta}\left(\frac{D\eta}{Dt}\right)_z = \frac{\partial}{\partial \eta}\left[\left(\frac{\partial \eta}{\partial t}\right)_z + u\left(\frac{\partial \eta}{\partial x}\right)_z + v\left(\frac{\partial \eta}{\partial y}\right)_z + w\frac{\partial \eta}{\partial z}\right] \times \frac{\partial z}{\partial z} \\
&= \frac{\partial z}{\partial \eta}\left[\frac{\partial}{\partial t}\frac{\partial \eta}{\partial z} + u\frac{\partial}{\partial x}\frac{\partial \eta}{\partial z} + v\frac{\partial}{\partial y}\frac{\partial \eta}{\partial z} + w\frac{\partial}{\partial z}\frac{\partial \eta}{\partial z}\right] \\
&\qquad + \frac{\partial z}{\partial \eta}\left[\left(\frac{\partial \eta}{\partial x}\right)_z \frac{\partial u}{\partial z} + \left(\frac{\partial \eta}{\partial y}\right)_z \frac{\partial v}{\partial z} + \frac{\partial \eta}{\partial z}\frac{\partial w}{\partial z}\right] \\
&= \frac{\partial z}{\partial \eta}\frac{D}{Dt}\frac{\partial \eta}{\partial z} + \left(\frac{\partial \eta}{\partial x}\right)_z \frac{\partial u}{\partial \eta} + \left(\frac{\partial \eta}{\partial y}\right)_z \frac{\partial v}{\partial \eta} + \frac{\partial w}{\partial z}
\end{aligned}
$$

Rearranging

$$
\frac{\partial w}{\partial z} = \frac{\partial \dot{\eta}}{\partial \eta} - \frac{\partial z}{\partial \eta}\frac{D}{Dt}\frac{\partial \eta}{\partial z} - \left(\frac{\partial \eta}{\partial x}\right)_z \frac{\partial u}{\partial \eta} - \left(\frac{\partial \eta}{\partial y}\right)_z \frac{\partial v}{\partial \eta} \tag{A.4}
$$

Substituting (A.2a)-(A.3) and (A.4) into the continuity equation (A.1d);

$$
\begin{aligned}
\frac{D\ln\rho}{Dt} + \left(\frac{\partial u}{\partial x}\right)_\eta + \frac{\partial u}{\partial \eta}\left(\frac{\partial \eta}{\partial x}\right)_z + \left(\frac{\partial v}{\partial y}\right)_\eta + \frac{\partial v}{\partial \eta}\left(\frac{\partial \eta}{\partial y}\right)_z + \\
\frac{\partial \dot{\eta}}{\partial \eta} - \frac{\partial z}{\partial \eta}\frac{D}{Dt}\frac{\partial \eta}{\partial z} - \left(\frac{\partial \eta}{\partial x}\right)_z \frac{\partial u}{\partial \eta} - \left(\frac{\partial \eta}{\partial y}\right)_z \frac{\partial v}{\partial \eta} = 0
\end{aligned}
$$

$$
\frac{D\ln\rho}{Dt} + \left(\frac{\partial u}{\partial x}\right)_\eta + \left(\frac{\partial v}{\partial y}\right)_\eta + \frac{\partial \dot{\eta}}{\partial \eta} - \frac{\partial z}{\partial \eta}\frac{D}{Dt}\frac{\partial \eta}{\partial z} = 0 \tag{A.5}
$$

The last term can be simplified using the hydrostatic equation and solving for ρ. By definition, ρ is always positive so we can cast the equation as such;

$$
\begin{aligned}
\rho &= \frac{1}{g}\left|\frac{\partial p}{\partial z}\right| = \frac{1}{g}\left|\frac{\partial \eta}{\partial z}\right|\left|\frac{\partial p}{\partial \eta}\right| \\
&= m\left|\frac{\partial \eta}{\partial z}\right|
\end{aligned} \tag{A.6}
$$

Where

$$
m \equiv \frac{1}{g}\left|\frac{\partial p}{\partial \eta}\right| \tag{A.7}
$$

is known as the pseudo-density because hydrostatically $dp = gd(\text{mass})/dxdy \Rightarrow d(\text{mass}) = \rho dzdxdy = md\eta dxdy$. $d\eta$ may contain information about mass and length, in which case m is a modifier to convert this number to an actual mass, just like ρ does to a volume element, $dzdxdy$. Note that the absolute sign could be dropped because η and p are monotonic.

Now taking the $\frac{D\ln()}{Dt}$ of A.6;

$$\frac{D\ln\rho}{Dt} = \frac{D}{Dt}\left[\ln m + \ln\left|\frac{\partial\eta}{\partial z}\right|\right] = \frac{D\ln m}{Dt} + \frac{\partial z}{\partial\eta}\frac{D}{Dt}\frac{\partial\eta}{\partial z}$$

Now substituting this into the last term of (A.5) to get the new form of the continuity equation;

$$\frac{Dm}{Dt} + m\left[\left(\frac{\partial u}{\partial x}\right)_\eta + \left(\frac{\partial v}{\partial y}\right)_\eta + \frac{\partial\dot{\eta}}{\partial\eta}\right] = 0 \tag{A.8}$$

We now transform the hydrostatic equation (vertical momentum equation) with A.3;

$$\begin{aligned}\frac{\partial p}{\partial z} = \frac{\partial p}{\partial\eta}\frac{\partial\eta}{\partial z} &= -\rho g \\ \frac{\partial\phi}{\partial\eta} &= -\frac{1}{\rho}\frac{\partial p}{\partial\eta}\end{aligned} \tag{A.9}$$

where $\phi = gz$.

The last terms to transform are the horizontal pressure gradient terms. For this, substitute $\psi = p$ into A.2b and $\psi = \phi$ into A.3, noting that $\left(\frac{\partial\phi}{\partial x}\right)_z = 0$, eliminating $\left(\frac{\partial\eta}{\partial x}\right)_z$ between them and using the hydrostatic equation to relate $\frac{\partial p}{\partial z}$ to m, we find;

$$\frac{1}{\rho}\left(\frac{\partial p}{\partial x}\right)_z = \left(\frac{\partial\phi}{\partial x}\right)_\eta + \frac{1}{m}\frac{\partial\phi}{\partial\eta}\left(\frac{\partial p}{\partial x}\right)_\eta = \left(\frac{\partial\phi}{\partial x}\right)_\eta$$

Where the last term is for the special case $p = f(\eta)$ only. This applies similarly for the y component too.

Restating the complete, generalized vertical co-ordinate system on the cartesian plane, with the First Law back in explicit form;

$$\frac{Du}{Dt} = -\left(\frac{\partial \phi}{\partial x}\right)_\eta + \frac{1}{m}\frac{\partial \phi}{\partial \eta}\left(\frac{\partial p}{\partial x}\right)_\eta + fv + F_x \tag{A.10a}$$

$$\frac{Dv}{Dt} = -\left(\frac{\partial \phi}{\partial y}\right)_\eta + \frac{1}{m}\frac{\partial \phi}{\partial \eta}\left(\frac{\partial p}{\partial y}\right)_\eta - fu + F_y \tag{A.10b}$$

$$\frac{\partial \phi}{\partial \eta} = -\frac{1}{\rho}\frac{\partial p}{\partial \eta} \tag{A.10c}$$

$$\frac{Dm}{Dt} + m\left[\left(\frac{\partial u}{\partial x}\right)_\eta + \left(\frac{\partial v}{\partial y}\right)_\eta + \frac{\partial \dot{\eta}}{\partial \eta}\right] = 0 \tag{A.10d}$$

$$C_p\frac{DT}{Dt} - \frac{1}{\rho}\frac{Dp}{Dt} = Q \tag{A.10e}$$

$$p = \rho RT \tag{A.10f}$$

where

$$\frac{D}{Dt} = \left(\frac{\partial}{\partial t}\right)_\eta + u\left(\frac{\partial}{\partial x}\right)_\eta + v\left(\frac{\partial}{\partial y}\right)_\eta + \dot{\eta}\frac{\partial}{\partial \eta}$$

$$f = 2\Omega \sin\theta \qquad \dot{\eta} = \left(\frac{D\eta}{Dt}\right)_z \qquad \phi = gz \qquad m = \frac{1}{g}\left|\frac{\partial p}{\partial \eta}\right|$$

Log-Pressure Co-Ordinate

Now for the special case of $\eta = \ln(p_0/p) \equiv z^*$.

$$p = p_0 e^{-\eta} = p_0 e^{-z^*}$$

$$\frac{\partial p}{\partial \eta} = -p \qquad m = |-p|/g = (p_0/g)e^{-z^*} \qquad \dot{\eta} = \frac{Dz^*}{Dt} \equiv w^*$$

Where w^* defines the $\ln -p$ velocity. As p is a function of η, the second term in the horizontal pressure gradient force is zero. Similarly, as $m = f(p) = f(\eta)$, all but the last term in the material derivative are zero, and by direct substitution, $\frac{1}{m}\frac{Dm}{Dt} = -w^*$.

The right hand side of the hydrostatic equation becomes $p/\rho = RT$ by the ideal gas law. Furthermore, as the First law contains the term $\frac{Dp}{Dt}$ and $p = f(\eta)$, this becomes $\frac{Dp}{Dt} = -w^*p$ which allows the first law to be written as $\frac{DT}{Dt} + \kappa T w^* = \frac{Q}{C_p}$ and the entire system can be written as;

$$
\begin{aligned}
\frac{Du}{Dt} &= -\frac{\partial\phi}{\partial x} + fv + F_x \\
\frac{Dv}{Dt} &= -\frac{\partial\phi}{\partial y} - fu + F_y \\
\frac{\partial\phi}{\partial z} &= RT \\
\frac{\partial u}{\partial x} + \frac{\partial v}{\partial y} + \frac{\partial w}{\partial z} - w &= 0 \\
\frac{DT}{Dt} + \kappa T w &= \frac{Q}{C_p} \\
p &= \rho RT
\end{aligned}
$$

Where

$$\frac{D}{Dt} = \frac{\partial}{\partial t} + u\frac{\partial}{\partial x} + v\frac{\partial}{\partial y} + w\frac{\partial}{\partial z}$$

With subscripts dropped and $w = w^*$.

Appendix B

The Hermite Polynomials

Various methods for defining the Hermite polynomials are available. The discussion here permits the derivation of the form of the Hermite polynomials, their reoccurrence relations and the differential equation that they inherently satisfy.

Beginning with the function definition;

$$\begin{aligned}
F^0(z) &= e^{-z^2} \\
F^1(z) &= \frac{dF}{dz} = -2ze^{-z^2} \\
F^2(z) &= \frac{d^2F}{dz^2} = (4z^2 - 2)e^{-z^2} \\
F^n(z) &= \frac{d^nF}{dz^n} = (-1)^n H_n(z)e^{-z^2}
\end{aligned}$$

Where H_n are the Hermite polynomials, such that;

$$\begin{aligned}
H_0(z) &= 1 \\
H_1(z) &= 2z \\
H_2(z) &= 4z^2 - 2 \\
H_n(z) &= (-1)^n e^{z^2} \frac{d^n}{dz^n} e^{-z^2}
\end{aligned}$$

Where the definition of H_n arises from rearranging the general expression of $F^n(z)$. Now taking the Taylor series expansion of $F(z-t)$;

$$F(z-t) = \sum_{n=0}^{\infty} \frac{(-t)^n}{n!} \frac{d^n}{dz^n} F(z) = \sum_{n=0}^{\infty} \frac{(-t)^n}{n!} F^n(z)$$
$$= \sum_{n=0}^{\infty} \frac{(-t)^n}{n!} (-1)^n H_n(z) e^{-z^2}$$
$$= \sum_{n=0}^{\infty} \frac{t^n}{n!} H_n(z) e^{-z^2}$$

Writing $F(z-t) = e^{-(z-t)^2} = e^{-z^2+2zt-t^2}$, then;

$$e^{2zt-t^2} = \sum_{n=0}^{\infty} \frac{t^n}{n!} H_n(z)$$

This is known as the generating function. One might quickly see that describing the Hermite polynomials from this series would be painstaking compared to the initial definition. However, by taking the derivative with respect to t of this expression, we can form a recurrence relation that provides the simplest method for generating the Hermite Polynomials;

$$(2z-2t)e^{2zt-t^2} = \sum_{n=1}^{\infty} \frac{nt^{n-1}}{n!} H_n(z)$$
$$2z \sum_{n=0}^{\infty} \frac{t^n}{n!} H_n(z) - 2t \sum_{n=0}^{\infty} \frac{t^n}{n!} H_n(z) = \sum_{n=1}^{\infty} \frac{t^{n-1}}{(n-1)!} H_n(z)$$
$$2z \sum_{n=0}^{\infty} \frac{t^n}{n!} H_n(z) - 2 \sum_{n=0}^{\infty} \frac{t^{n+1}}{n!} H_n(z) = \sum_{n=1}^{\infty} \frac{t^{n-1}}{(n-1)!} H_n(z)$$

We now wish to have all t to the same power, so, re-indexing appropriately;

$$2z \sum_{n=0}^{\infty} \frac{t^n}{n!} H_n(z) - 2 \sum_{n=1}^{\infty} \frac{t^n}{(n-1)!} H_{n-1}(z) = \sum_{n=0}^{\infty} \frac{t^n}{n!} H_{n+1}(z)$$

Note that the summations are not of the same order. Furthermore, the indexing on the Hermite polynomials involves +1 and -1. As we know the first two Hermite polynomials (H_0 and H_1), we can assume the summation starts from H_2, or $n = 2$, thus

$$2z\sum_{n=2}^{\infty}\frac{t^n}{n(n-1)!}H_n(z) - 2\sum_{n=2}^{\infty}\frac{t^n}{(n-1)!}H_{n-1}(z) = \sum_{n=2}^{\infty}\frac{t^n}{n(n-1)!}H_{n+1}(z)$$

Hence,

$$H_{n+1}(z) = 2zH_n(z) - 2nH_{n-1}(z)$$

In a similar fashion, differentiating the generating function with respect to z;

$$\begin{aligned}
2te^{2zt-t^2} &= \sum_{n=0}^{\infty}\frac{t^n}{n!}\frac{d}{dz}H_n(z) \\
2t\sum_{n=0}^{\infty}\frac{t^n}{n!}H_n(z) &= \sum_{n=0}^{\infty}\frac{t^n}{n!}\frac{d}{dz}H_n(z) \\
2\sum_{n=0}^{\infty}\frac{t^{n+1}}{n!}H_n(z) &= \sum_{n=0}^{\infty}\frac{t^n}{n!}\frac{d}{dz}H_n(z) \\
2\sum_{n=1}^{\infty}\frac{t^n}{(n-1)!}H_{n-1}(z) &= \sum_{n=0}^{\infty}\frac{t^n}{n!}\frac{d}{dz}H_n(z) \\
2\sum_{n=2}^{\infty}\frac{t^n}{(n-1)!}H_{n-1}(z) &= \sum_{n=2}^{\infty}\frac{t^n}{n(n-1)!}\frac{d}{dz}H_n(z)
\end{aligned}$$

Hence,

$$\frac{d}{dz}H_n(z) = 2nH_{n-1}(z)$$

The Hermite Polynomials also satisfy a general class of differential equations. By Taking the $\frac{d}{dz}$ of the Hermite recurrence relation;

$$\frac{d}{dz}H_{n+1}(z) = 2H_n(z) + 2z\frac{d}{dz}H_n(z) - \frac{d}{dz}2nH_{n-1}(z)$$

and substituting the differential recurrence relation;

$$2(n+1)H_n(z) = 2H_n(z) + 2z\frac{d}{dz}H_n(z) - \frac{d^2}{dz^2}H_n(z)$$

$$\left(\frac{d^2}{dz^2} - 2z\frac{d}{dz} + 2n\right) H_n(z) = 0$$

In Summary;

The Hermite Polynomials are given by

$$H_0(z) = 1$$

$$H_1(z) = 2z$$

$$H_{n+1}(z) = 2zH_n(z) - 2nH_{n-1}(z)$$

and have derivatives by;

$$\frac{d}{dz}H_n(z) = 2nH_{n-1}(z)$$

They have the symmetry property that;

$$H_n(-z) = (-1)^n H_n(z)$$

They are orthogonal to the weighting function e^{-z^2} such that;

$$\int_{-\infty}^{\infty} H_m(z)H_n(z)e^{-z^2} = \delta_{mn}2^n n!\sqrt{\pi}$$

and thus form linearly independent solutions to the general differential equation

$$\left(\frac{d^2}{dz^2} - 2z\frac{d}{dz} + 2n\right) H_n(z) = 0$$

Appendix C

Orthogonal Eigenfunctions for the Degenerate $k = 0$ Rossby Mode

For the $r = 0$ root of the cubic dispersion diagram, as $k \to 0$, $\nu \to 0$ for $n > 1$ such that degeneracy occurs and orthogonality is not guaranteed by the uniqueness of eigenvalues. To find the orthogonal eigenfunctions, we wish to take the limit of the known eigenfunctions as $k \to 0$, which by the dispersion equation, implies that $k << 1$ and $\nu << 1$. Ignoring higher powers of these parameters, the dispersion equation becomes:

$$\nu = \frac{ck}{2n+1} \tag{C.1}$$

Substituting this into (2.38) and taking the limit as $k \to 0$, noting that we have evaluated the normalization constant, we find:

$$\mathbf{K}_{n,0}(0,\hat{y}) = \frac{c}{\sqrt{2}\pi^{\frac{1}{4}}\sqrt{2n+1}} \begin{pmatrix} \left[(n+1)^{\frac{1}{2}}\mathcal{H}_{n-1}(\hat{y}) - n^{\frac{1}{2}}\mathcal{H}_{n+1}(\hat{y})\right] \\ 0 \\ -c\left[(n+1)^{\frac{1}{2}}\mathcal{H}_{n-1}(\hat{y}) + n^{\frac{1}{2}}\mathcal{H}_{n+1}(\hat{y})\right] \end{pmatrix} \quad n > 1 \tag{C.2}$$

which can be verified to satisfy (2.32) by direct substitution.

Appendix D

Power Series Solution of Hermite's Differential Equation

Although the solution to Hermites' differential equation are known, this derivation highlights some useful properties and points relating to the solution. Defining the power series and their first two differentials ;

$$\hat{V}(k,\hat{y}) = \sum_{m=0}^{\infty} a_m \hat{y}^m \tag{D.1}$$

Then

$$\frac{d\hat{V}}{d\hat{y}} = \sum_{m=1}^{\infty} m a_m \hat{y}^{m-1} = \sum_{m=0}^{\infty} m a_m \hat{y}^{m-1}$$

where we can index m from 0 instead of 1 because $\left(\frac{d\hat{V}}{d\hat{y}}\right)_{m=0} = 0$. Taking the derivative of this and re-indexing with $m = m + 2$;

$$\frac{d^2\hat{V}}{d\hat{y}^2} = \sum_{m=2}^{\infty} (m-1) m a_m \hat{y}^{m-2} = \sum_{m=0}^{\infty} (m+1)(m+2) a_{m+2} \hat{y}^m$$

Substituting these into (2.24);

$$\sum_{m=0}^{\infty}\left[(m+1)(m+2)a_{m+2}+(R-2m)\,a_m\right]\hat{y}^m=0$$

where $R=\frac{\nu^2}{c\beta}-\frac{c}{\beta}k^2+c\frac{k}{\nu}-1$. As $y^m=0$ only for $y=0$, we require the bracketed term to be zero for all m to guarantee that the power series (D.1) is a solution to the differential equation (2.24). This yields the recurrence relation for the power series coefficients as;

$$a_{m+2}=\frac{2m-R}{(m+1)(m+2)}a_m \tag{D.2}$$

Thus (D.1) and (D.2) form a complete solution for (2.24).

Harmonics of The Power Series

The form of (D.1) as an infinite series is not very practical nor insightful. We first note that the recurrence relation has two unknowns, a_0 and a_1. From these, the even m completely depend on a_0 and the odd m on a_1. As a_0 and a_1 are constants of integration, they are completely arbitrary and we simply choose $a_0=1$ and $a_1=2$. It is evident that, as $m\to\infty$, $a_{m+2}\to 0$ such that the power series is truncated at some point if R is finite. Thus the complete infinite series is not required to represent the solution for $R<\infty$. Clearly, if $R=2n$ and $(n=0,1,2,...,\infty)$ then the series is truncated exactly at $m=n$ for either the odd or even m's following but not both. Using this property, we divide the complete solution into a set of even and odd solutions, such that:

$$\hat{V}(k,\hat{y})=\sum_{\frac{m}{2}=0}^{\infty}a_m\hat{y}^m+\sum_{\frac{m-1}{2}=0}^{\infty}a_m\hat{y}^m$$

The even series solution will be truncated if n is even and the odd series solution if n is odd, which defines the harmonics:

$$H_n = \begin{cases} \sum_{\frac{m}{2}=0}^{n} h_m \hat{y}^m & \text{if } n \text{ even} \\ \sum_{\frac{m-1}{2}=0}^{n} h_m \hat{y}^m & \text{if } n \text{ odd} \end{cases}$$

$$R = 2n \quad \text{and} \quad n = 0, 1, ..., \infty$$

where the harmonic coefficients are defined as h_m to distinguish these from the full solution a_m and that;

$$h_{m+2} = \frac{2(m-n)}{(m+1)(m+2)} h_m \tag{D.3}$$

We now evaluate the first few n and chose h_0 and h_1 to make all coefficients integers;

$H_0 = 1$	$h_0 = 1$
$H_1 = 2y$	$h_1 = 1$
$H_2 = 4y^2 - 2$	$h_0 = 2$
$H_3 = 8y^3 - 12y$	$h_1 = 12$
$H_4 = 16y^4 - 48y^2 + 12$	$h_0 = 12$

Which are formally equivalent to the Hermite Polynomials. This is expected since we have already shown that the solutions to the Hermite Differential equation are the Hermite polynomials and that they consist of odd and even functions. The utility of this is that it can now be shown that the sum of these Harmonic solutions, with the appropriate weight W_n, are equivalent to the general solution. Redefining the harmonic (Hermite) polynomials as;

$$H_n = \sum_{m=0}^{\infty} h_m \hat{y}^m$$

Noting that h_m are the Hermite Coefficients, which depend on n, then;

$$\begin{aligned}
\hat{V}(k,\hat{y}) = \sum_{m=0}^{\infty} a_m \hat{y}^m &= \sum_{n=0}^{\infty} W_n H_n \\
&= \sum_{n=0}^{\infty} W_n \sum_{m=0}^{\infty} h_m \hat{y}^m \\
&= \sum_{n=0}^{\infty} \sum_{m=0}^{\infty} W_n h_m \hat{y}^m \\
&= \sum_{m=0}^{\infty} \sum_{n=0}^{\infty} W_n h_m \hat{y}^m
\end{aligned}$$

This is true if, and only if;

$$a_m = \sum_{n=0}^{\infty} W_n h_m \qquad m = 0, 1, ..., \infty \tag{D.4}$$

This explicitly states that the true solution is the sum of weighted basis functions (Hermite Polynomials). From Appendix B, we also know that the basis functions are orthogonal. This is a classic result of linear differential equation theory in that the true solution of a system with boundary conditions will be some combination of constants (an eigenvector) multiplied by basis functions (eigenfunctions) whose linearly independence is guaranteed if their eigenvalues (R in this case) are unique. Note that if the eigenvalues were not unique, care must be taken to make sure the eigenfunctions are. If this were note the case, there would be multiple harmonic basis functions with the same form - that is they would be identical Hermite Polynomials but with a different index n. In this case, (D.4) could not be true because W_n would be identical for both n yielding a value of a_m twice as large as required.

The utility of the power series derivation is to highlight that $R = (\frac{\nu^2}{c\beta} - \frac{c}{\beta}k^2 + c\frac{k}{\nu} - 1)$ is **not** discrete but is continuous and that harmonics exists only because the solution can truncate, based on the boundary conditions. One must be careful not to interpret the harmonic functions as the actual solution since, as this derivation proves, the true solution is the sum of all harmonics. In the case that $R \approx n$ for the true solution, then it is easily verified that the basis functions whose index is n will dominate the solution. These arguments are analogous to the mechanics of a Fourier transform and in that manner, one must consider all basis functions when refereing to the true, physical solution.

In summary, the re-dimensionalized solution of

$$\frac{d^2V}{dy^2} + \left[\frac{\nu^2}{c^2} - k^2 + \beta\frac{k}{\nu} - \frac{\beta^2}{c^2}y^2\right]V = 0$$

is

$$V(k,y) = CH_n\left(\sqrt{\tfrac{\beta}{c}}y\right)e^{-\frac{1}{2}\frac{\beta}{c}y^2}$$

if

$$\frac{\nu^2}{c\beta} - \frac{c}{\beta}k^2 + c\frac{k}{\nu} - 1 = 2n \quad (n = 0, 1, ..., \infty)$$

and C is some constant.

Appendix E

Analytical Solution for Gaussian Forcing in the Meridional Projection

We now assume that the structure for any of the forcing terms are gaussian in y, that is that the forcing is separable such that;

$$\hat{\hat{\mathbf{W}}}(k,y,t) = \hat{\hat{\mathbf{W}}}(k,t)\, e^{-(y\,-\,y_0)^2/a^2}$$

Where y_0 is the latitudinal offset of the forcing and a is the forcing radius, both in m's. Then the inner product for the meridional transform becomes;

$$\tilde{W}_{n,r}(k,t) = \left(\hat{\hat{\mathbf{W}}}(k,t)e^{-(y\,-\,y_0)^2/a^2}, \mathbf{K}_{n,r}(k,y)\right)$$

Noting that the backward transform remains the same. When the inner product is computed, the following term appears commonly among the different components;

$$\int_{-\infty}^{\infty} \mathcal{H}_n(\hat{y})e^{-(y\,-\,y_0)^2/a^2}dy$$

This integral has mixed units, so we non-dimensionalize y, y_0 and a by the usual substitution $\hat{()} = ()\sqrt{\beta/c}$ while also substituting the full form for $\mathcal{H}_n$;

$$= (2^n n!)^{\frac{1}{2}} (c/\beta)^{\frac{1}{2}} \int_{-\infty}^{\infty} H_n(\hat{y}) e^{-\frac{1}{2}\hat{y}^2} e^{-(\hat{y} - \hat{y_0})^2/\hat{a}^2} d\hat{y}$$

Combining the exponentials exponents into one term

$$-\frac{1}{2}\hat{y}^2 - (\hat{y} - \hat{y_0})^2/\hat{a}^2 = -\frac{2+\hat{a}^2}{2\hat{a}^2}\left[\hat{y}^2 - \frac{4\hat{y_0}}{2+\hat{a}^2}\hat{y}\right] - \hat{y_0}^2/\hat{a}^2$$

Complete the square of the term in brackets using the formula $\hat{y}^2 + b\hat{y} = (\hat{y} + b/2)^2 - b^2/4$

$$= -\frac{2+\hat{a}^2}{2\hat{a}^2}\left[\left(\hat{y} - \frac{2\hat{y_0}}{2+\hat{a}^2}\right)^2 - \frac{4\hat{y_0}^2}{(2+\hat{a}^2)^2}\right] - \hat{y_0}^2/\hat{a}^2$$

$$= -\left(\frac{\sqrt{2+\hat{a}^2}}{\sqrt{2}\hat{a}}\hat{y} - \frac{\hat{y_0}\sqrt{2}}{\hat{a}\sqrt{2+\hat{a}^2}}\right)^2 - \frac{\hat{y_0}^2}{(2+\hat{a}^2)}$$

The integral now becomes;

$$(2^n n!)^{-1/2}\sqrt{\frac{c}{\beta}}\, e^{-\frac{\hat{y_0}^2}{(2+\hat{a}^2)}} \int_{-\infty}^{\infty} H_n(\hat{y})\, e^{-\left(\frac{\sqrt{2+\hat{a}^2}}{\sqrt{2}\hat{a}}\hat{y} - \frac{\hat{y_0}\sqrt{2}}{\hat{a}\sqrt{2+\hat{a}^2}}\right)^2} d\hat{y}$$

From Gradshteyn and Ryzhik (2000);

$$\int_{-\infty}^{\infty} H_n(\alpha X) e^{-(X-Y)^2} dX = \pi^{\frac{1}{2}}(1-\alpha^2)^{n/2} H_n\left[\frac{\alpha Y}{(1-\alpha^2)^{\frac{1}{2}}}\right]$$

Setting

$$X = \frac{\sqrt{2+\hat{a}^2}}{\sqrt{2}\hat{a}}\hat{y} \qquad Y = \frac{\hat{y_0}\sqrt{2}}{\hat{a}\sqrt{2+\hat{a}^2}} \qquad \alpha X = \hat{y}$$

and noting that $1-\alpha^2 = 1 - \dfrac{2\hat{a}^2}{2+\hat{a}^2} = \dfrac{2-\hat{a}^2}{2+\hat{a}^2}$. Care must be taken with the resubstitution of $\mathcal{H}_n$, since it contains the term $e^{-\frac{1}{2}\hat{y}^2}$, which we combine with the leading exponential.

$$\int_{-\infty}^{\infty} \mathcal{H}_n(\hat{y}) e^{-(y-y_0)^2/a^2} dy =$$

$$(c/\beta)^{\frac{1}{2}} e^{\left(\frac{\hat{a}^2\hat{y_0}^2}{4-\hat{a}^4}\right)} \left(\frac{2\pi\hat{a}^2}{2+\hat{a}^2}\right)^{\frac{1}{2}} \left(\frac{2-\hat{a}^2}{2+\hat{a}^2}\right)^{n/2} \mathcal{H}_n\left(\frac{2\hat{y}_0}{\sqrt{4-\hat{a}^4}}\right)$$

where $0 < \hat{a} < \sqrt{2}$

Note that as $0 < a < \sqrt{2c/\beta}$, the shallow modes can not extend far in y for this to remain valid. We now use this integral to complete the inner product for all components and find that the full spectral transform of the forcing is;

$$\tilde{W}_{n,r}(k,t) =$$

$$\hat{\tilde{\mathbf{W}}}(k,t) \bullet \begin{cases} \begin{pmatrix} (c/2\beta)^{\frac{1}{2}} \left[(n+1)^{\frac{1}{2}}(\nu_{n,r}-ck)\mathcal{G}_{n+1} + n^{\frac{1}{2}}(\nu_{n,r}+ck)\mathcal{G}_{n-1}\right] \\ -i\beta^{-1}(\nu_{n,r}^2 - c^2k^2)\mathcal{G}_n \\ (2c\beta)^{-\frac{1}{2}} \left[(n+1)^{\frac{1}{2}}(\nu_{n,r}-ck)\mathcal{G}_{n+1} - n^{\frac{1}{2}}(\nu_{n,r}+ck)\mathcal{G}_{n-1}\right] \end{pmatrix} N_{n,r} & n \geq 0 \\ \begin{pmatrix} c \\ 0 \\ 1 \end{pmatrix} (2\sqrt{\pi})^{-\frac{1}{2}} \quad \mathcal{G}_0 & n = -1 \end{cases}$$

and

$$\mathcal{G}_n = c^{-2} e^{\left(\frac{\hat{a}^2\hat{y_0}^2}{4-\hat{a}^4}\right)} \left(\frac{2\pi\hat{a}^2}{2+\hat{a}^2}\right)^{\frac{1}{2}} \left(\frac{2-\hat{a}^2}{2+\hat{a}^2}\right)^{n/2} \mathcal{H}_n\left(\frac{2\hat{y}_0}{\sqrt{4-\hat{a}^4}}\right)$$

noting that $\hat{()} = ()\sqrt{\beta/c}$.

A special case of this projection is when $y_0 = 0$. This dictates that the only values of $\mathcal{G}_n$ that can contribute are ones in which $\mathcal{H}_n(0) \neq 0$, which can only be satisfied for the symmetrical class of Hermite polynomials (even n). If the forcing is in U or Φ then, by the above equation, only odd values of n in $W_{n,r}$ will have non-zero spectral power, which then correspond to the symmetrical structure functions in U and Φ. Thus, the equator must be a local maxima/minima for these fields, which then implies no first-order cross-equatorial gradients. Furthermore, as V projects onto the odd functions, it must be zero on the equator. Note that forcing in V will produce the opposite effect with cross equatorial flow (nonzero V) with zero U and Φ and, possibly, cross equatorial gradients.

Bibliography

Augstein, E., H. Riehl, R. Ostapoff, and V. Wagner, 1973: Mass and energy transports in an undisturbed Atlantic Trade wind flow. *Monthly Weather Review*, **101**, 101–111.

Betts, A., 1973: Non-precipitating cumulus convection and its parameterization. *Quart. J. Roy. Meteorol. Soc.*, **86**, 178–196.

Betts, A. and W. Ridgway, 1989: Climatic equilibrium of the atmospheric convective boundary layer over a tropical ocean. *J. Atmos. Sci*, **46**, 26212641.

Biello, J. and A. Majda, 2005: A New Multiscale Model for the Madden Julian Oscillation. *J. Atmos. Sci*, **62**, 65–87.

Bjerknes, J., 1938: Saturated adiabatic ascent of air through dry-adiabatically descending environment. *Quart. J. Roy. Meteorol. Soc.*, **108**, 325–330.

Bretherton, C., P. Blossey, and M. Khairoutdinov, 2005: An Energy-Balance Analysis of Deep Convective Self-Aggregation above Uniform SST. *J. Atmos. Sci*, **62**, 4273–4292.

Bretherton, C. and P. Smolarkiewicz, 1989: Gravity Waves, Compensating Subsidence and Detrainment around Cumulus Clouds. *J. Atmos. Sci*, **46**, 740–759.

Deardorff, J., 1980: Stratocumulus-capped mixed layers derived from a three-dimensional model. *Bound.-Layer Meteor.*, **18**, 495–527.

DeMaria, M., 1985: Linear Response of a Stratified Tropical Atmopshere to Convective Forcing. *J. Atmos. Sci*, **42**, 1944–1959.

Emanuel, K., J. Neelin, and C. Bretherton, 1994: On large-scale circulations in convecting atmopsheres. *Quart. J. Roy. Meteorol. Soc.*, **120**, 1111–1143.

Esbensen, S., 1978: Bulk thermodynamic effects and properties of small tropical cumuli. *J. Atmos. Sci*, **35**, 826–837.

Fulton, S. and W. Schubert, 1985: Vertical normal mode transforms: Theory and application. *Monthly Weather Review*, **113**, 647–658.

Gill, A., 1980: Some simple solutions for heat-induced tropical circulation. *Quart. J. Roy. Meteorol. Soc.*, **106**, 447–462.

— 1982a: *Atmopshere-Ocean Dynamics*. Academic Press, San Diego, CA.

— 1982b: Studies of moisture effects in simple atmospheric models: The Stable Case. *Geophys. Astrophys. Fluid Dyn.*, **19**, 119–152.

Grabowski, W. and M. Moncrieff, 2000: Large-scale organization of tropical convection in two-dimenisonal explicit numerical simulations. *Quart. J. Roy. Meteorol. Soc.*, **127**, 445–468.

Gradshteyn, I. and I. Ryzhik, 2000: *Table of Integrals, Series, and Products*. Academic Press.

Held, I., R. Hemler, and V. Ramaswamy, 1993: Radiative Convective Equilibrium with explicit two-dimensional moist convection. *J. Atmos. Sci*, **50**, 3909–3927.

Holton, J., 1992: *An Introduction to Dynamic Meteorology - Third Edition*. Academic Press, San Diego, CA.

Houze, R., 1977: Structure and Dynamics of a Tropical SquallLine System. *Monthly Weather Review*, **105**, 1540–1567.

— 1989: Observed Structure of meso-scale convective systems and implications for large-scale heating. *Quart. J. Roy. Meteorol. Soc.*, **115**, 425–461.

Inness, P., J. Slingo, S. Woolnough, R. Neal, and V. Pope, 2001: Organization of tropical convection in a GCM with varying vertical resolution: implications for the simulation of the Madden-Julian Oscillation. *Climate Dynamics*, **17**, 777–793.

Johnson, R. and P. Ciesielski, 2000: Rainfall and Radiative Heating Rates from TOGA COARE Atmospheric Budgets. *J. Atmos. Sci*, **57**, 1497–1514.

Johnson, R. and X. Lin, 1997: Episodic Trade Wind Regimes over the Western Pacific Warm Pool. *J. Atmos. Sci*, **54**, 2020–2034.

Johnson, R., T. Rickenbach, S. Rutledge, P. Ciesielske, and W. Schubert, 1999: Trimodeal characteristics of tropical convection. *J. Climate*, **12**, 2397–2418.

Johnson, R. H., 1978: Cumulus Transports in a Tropical Wave Composite for Phase III of GATE. *J. Atmos. Sci*, **35**, 484–494.

Kessler, E., 1969: On the distribution and continuity of water substance in atmospheric circulations. *Meteorl. Monogr.*, **10**, 8.

Khairoutdinov, M. and D. Randall, 2003: Cloud Resolving Modeling of the ARM Summer 1997 IOP: Model Formulation, Results, Uncertainties, and Sensitivities. *J. Atmos. Sci*, **60**, 607–625.

Lau, K.-M., 1981: Oscillations in a Simple Equatorial Climate System. *J. Atmos. Sci*, **38**, 248–261.

Lau, K.-M. and L. Peng, 1987: Origin of low-frequency (intraseasonal) oscillations in the tropical atmosphere Part I: Basic theory. *J. Atmos. Sci*, **44**, 950–972.

Lindzen, R., 1967: Planetary waves on beta-planes. *Monthly Weather Review*, **95**, 441–451.

— 1973: Wave-cisk in the tropics. *J. Atmos. Sci*, **31**, 156–179.

— 2003: The interaction of waves and convection in the tropics. *J. Atmos. Sci*, **60**, 3009–3020.

Longuet-Higgins, M., 1968: The eigenfunctions of laplace's tidal equation over a sphere. *Phlios. Trans. Roy. Soc. London*, **262A**, 511–607.

Madden, R. and P. Julian, 1971: Detection of a 4050 day oscillation in the zonal wind in the tropical pacific. *J. Atmos. Sci*, **28**, 702–708.

Mapes, B., 1993: Gregarious tropical convection. *J. Atmos. Sci*, **50**, 2026–2037.

— 2001: Water's two height scales: The moist adiabat and the radiative troposphere. *Quart. J. Roy. Meteorol. Soc.*, **127**, 2353–2366.

Mapes, B. and R. Houze, 1995: Diabtic Divergence Profiles in Western Pacific Mesoscale Convective Systems. *J. Atmos. Sci*, **52**, 1807–1828.

Mapes, B. and P. Zuidema, 1996: Radiative-dynamical consequences of dry tongues in the tropical troposphere. *J. Atmos. Sci*, **53**, 620–638.

Masunaga, H., T. L'Ecuyer, and C. Kummerow, 2006: The Madden-Julian Oscillation Recorded in Early Observations from the Tropical Rainfall Measuring Mission (TRMM). *J. Atmos. Sci*, xxxx–xxxx.

Matsuno, T., 1966: Quasi-geostrophic motions in the equatorial area. *J. Meteor. Soc. Japan*, **44**, 25–42.

Milliff, R. and R. Madden, 1996: The Existence and Vertical Structure of Fast, Eastward-Moving Disturbances in the Equatorial Troposphere. *J. Atmos. Sci*, **53**, 586–597.

Nakazawa, T., 1988: Tropical super clusters within intraseasonal variations over the western pacific. *J. Meteor. Soc. Japan*, **66**, 823–839.

Neelin, J. and J. Yu, 1994: Modes of Tropical Variability under Convective Adjustment and the Madden-Julian Oscillation. Part I: Analytical theory. *J. Atmos. Sci*, **51**, 1876–1894.

Nicholls, S. and M. Lemone, 1980: The Fair Weather Boundary Layer in GATE: The Relationship of Subcloud Fluxes and Structure to the Distribution and Enhancement of Cumulus Clouds. *J. Atmos. Sci*, **37**, 2051–2067.

Nitta, T. and S. Esbensen, 1974: Heat and moisture budget analyses using bomex data. *Monthly Weather Review*, **102**, 1728.

Riehl, H. and J. Malkus, 1958: On the heat balance of the equatorial trough zone. *Geophys.*, **6**, 503538.

Rotunno, R., J. Klemp, and M. Weisman, 1988: A Theory for Strong, Long-Lived Squall Lines. *J. Atmos. Sci*, **45**, 463–485.

Schubert, W. and M. Masarik, 2006: Potential Vorticity aspects of the MJO. *Dynamics of Atmospheres and Oceans*, xxxx–xxxx.

Silva Dias, P., W. Schubert, and M. DeMaria, 1983: Large-scale response of the tropical atmosphere to transient convection. *J. Atmos. Sci*, **40**, 2689–2707.

Stephens, G., 1990: On the Relationship between Water Vapor over the Oceans and Sea Surface Temperature. *J. Climate*, **3**, 634–645.

— 2005: Cloud Feedbacks in the Climate System: A Critical Review. *J. Climate*, **18**, 237–273.

Stephens, G., P. Webster, R. Johnson, R. Engelen, and T. L'Ecuyer, 2004a: Observational Evidence for the Mutual Regulation of the Tropical Hydrological Cycle and Tropical Sea Surface Temperatures. *J. Climate*, **17**, 2213–2224.

Stephens, G. and N. Wood, 2005: what is it? *Monthly Weather Review*, submitted.

Stephens, G., N. Wood, and L. Pakula, 2004b: On the radiative effects of dust on tropical convection. *Geophys. Res. Letters*, **31**.

Stephens, G. L., P. M. Gabriel, and P. T. Partain, 2001: Parameterization of atmospheric radiative transfer I: Validity of simple models. *J. Atmos. Sci*, **58**, 3391–3409.

Straub, K. and G. Kiladis, 2002: Observations of a Convectively Coupled Kelvin Wave in the Eastern Pacific ITCZ. *J. Atmos. Sci*, **59**, 30–53.

Sui, C., W. T. K.M. Lau, and J. Simpson, 1994: The Tropical Water and Energy Cycles in a Cumulus Ensemble Model. Part I: Equilibrium Climate. *J. Atmos. Sci*, **51**, 711–728.

Tompkins, A., 2000: Impact of dimensionality on long-term cloud-resolving model simulations. *Monthly Weather Review*, **128**, 1521–1535.

— 2001a: Organization of tropical convection in low vertical wind shears: The role of cold pools. *J. Atmos. Sci*, **58**, 1650–1672.

— 2001b: Organization of tropical convection in low vertical wind shears: The role of water vapor. *J. Atmos. Sci*, **58**, 529–545.

Tompkins, A. and G. Craig, 1998: Time-scales of adjustment to radiative-convective equilibrium in the tropical atmosphere. *Quart. J. Roy. Meteorol. Soc.*, **124**, 2693–2713.

— 1999: Sensitivity of tropical convection to sea surface temperature in the absence of lare-scale flow. *J. Climate*, **12**, 462–476.

Tompkins, A. and K. Emanuel, 2000: The vertical resoloution sensitivity of simulated equilibrium temperature and water-vapour profiles. *Quart. J. Roy. Meteorol. Soc.*, **126**, 1219–1238.

Viterbi, A., 1966: *Principle of Coherent Communication.* McGraw Hill.

Wheeler, M. and G. Kiladis, 1999: Convectively coupled equatorial waves: Analysis of clouds and temperature in the wavenumber-frequency domain. *J. Atmos. Sci*, **56**, 374–399.

Wheeler, M., G. Kiladis, and P. Webster, 2000: Large-scale dynamical fields associated with convectively coupled equatorial waves. *J. Atmos. Sci*, **57**, 613–640.

Wu, Z., D. Battisti, and E. Sarachik, 2000a: Rayleigh Friction, Newtonian Cooling, and the Linear Response to Steady Tropical Heating. *J. Atmos. Sci*, **57**, 1937–1957.

— 2000b: Vertical Structure of Convective Heating and the Three-Dimensional Structure of the Forced Circulation of an Equatorial Beta Plane. *J. Atmos. Sci*, **57**, 2169–2187.

Wu, Z. and D. Moore, 2004: The completeness of eigenfunctions of the tidal equation on an equatorial beta plane. *J. Atmos. Sci*, **61**, 769–774.

Yanai, M., S. Esbensen, and J. Chu, 1973: Determination of bulk properties of tropical cloud clusters from large-scale heat and moisture budgets. *J. Atmos. Sci*, **30**, 611–627.

Yang, G., B. Hoskins, and J. Slingo, 2003: Convectively Coupled Equatorial Waves: A New Methodology for Identifying Wave Structures in Observational Data. *J. Atmos. Sci*, **60**, 1637–1654.

Zhang, C., 2005: Madden-Julian Oscillation. *Reviews of Geophysics*, **43**, 1–36.

Ziemianski, M., W. Grabowski, and M. W. Moncrieff, 2005: Explicit convection over the western Pacific Warm Pool in the Community Atmospheric Model. *J. Climate*, **18**, 1482–1502.